Gas-Phase Ion Chemistry in Interstellar, Circumstellar, and Planetary Environments

by

Nicholas J. Demarais

B.S., Minnesota State University, Mankato, 2009

A thesis submitted to the

Faculty of the Graduate School of the

University of Colorado in partial fulfillment

of the requirements for the degree of

Doctor of Philosophy

Department of Chemistry and Biochemistry

2014

This thesis entitled:
Gas-Phase Ion Chemistry in Interstellar, Circumstellar, and Planetary Environments
written by Nicholas J. Demarais
has been approved for the Department of Chemistry and Biochemistry

Veronica M. Bierbaum

Theodore P. Snow

Date _____

The final copy of this thesis has been examined by the signatories, and we find that both the content and the form meet acceptable presentation standards of scholarly work in the above mentioned discipline.

Demarais, Nicholas J. (Ph.D., Physical Chemistry)

Gas-Phase Ion Chemistry in Interstellar, Circumstellar, and Planetary Environments

Thesis directed by Dr. Veronica M. Bierbaum

Abstract

In the last century, astronomers, physicists, and chemists have shown that the environments of space are complex. Although we have learned a great amount about the interstellar medium, circumstellar medium, and atmospheres of other planets and moons, many mysteries still remain unsolved. The cooperation of astronomers, modelers, and chemists has lead to the detection of over 180 molecules in the interstellar and circumstellar medium, and the evolution of the new scientific field of astrochemistry. Gas-phase ion chemistry can determine the stability of ions in these complex environments, provide chemical networks, and guide searches for new interstellar molecules.

Using the flowing afterglow-selected ion flow tube (FA-SIFT), we have characterized the reactions of positive and negative ions that are important in a variety of astrochemical environments. The detection of CF^+ in photodissociation regions highlights the importance of fluorinated species in the interstellar medium. The viability of CF^+ as a possible diffuse interstellar band (DIB) carrier is discussed as related to reactions with neutral molecules in various interstellar conditions; the reactions of CF^+ with twenty-two molecules of interstellar relevance were investigated.

The chemical reactions of $HCNH^+$ with H_2, CH_4, C_2H_2, and C_2H_4 were reexamined to provide insight into the overprediction of $HCNH^+$ in Titan's ionosphere by current astrochemical models. In addition, this work suggests other chemical reactions that should be included in the current models to fully describe the destruction rates of $HCNH^+$ in Titan's ionosphere.

The reactions of polycyclic aromatic hydrocarbon (PAH) ions with H atoms and other

small molecules were carried out to determine the stability of these species. In diffuse regions, where the photon flux is high, PAH cations are the dominant ionization state. This work continues our previous research to include PAHs of differing geometries as well as nitrogen-containing PAHs. Extension to larger PAH cations was made possible by the integration of the laser induced acoustic desorption (LIAD) source with the FA-SIFT.

In addition, in dense environments, where the photon flux is low, anionic PAHs may exist. The detection of negative ions in the past 10 years has highlighted the importance of their inclusion in astrochemical models. We have investigated the chemistry of deprotonated PAHs with molecules of interstellar relevance to determine their chemical stability in dense regions of the interstellar and circumstellar medium.

In addition to PAH anions, H^- is an important species in dense interstellar environments. While the reaction of hydride anion has been recognized as a critical mechanism in the initial cooling immediately after the Big Bang, $H^- + H \longrightarrow H_2 + e^-$, chemistry with neutral molecules was largely unknown. The chemistry of H^- with various classes of organic molecules was investigated and conclusions are drawn based on reaction mechanisms.

Dedication

To my family.

"The nitrogen in our DNA, the calcium in our teeth, the iron in our blood, the carbon in our apple pies were made in the interiors of collapsing stars. We are made of star stuff."

—Carl Sagan

Acknowledgements

First and foremost, I would like to express my sincere gratitude to my adviser Veronica Bierbaum. Thank you for pushing me to become a better scientist, researcher, writer, and critic. I appreciate all of the time you have spent guiding and mentoring me. I will never forget your acute attention to detail and I will carry that with me throughout the rest of my career. Thank you for allowing me to fail and learn from my mistakes. In addition, I would like to acknowledge and thank my unofficial adviser, Theodore Snow. Thank you for exposing me to the field of astrophysics and introducing me to one of the most fascinating scientific mysteries, the diffuse interstellar bands. I appreciate your patience and guidance in my understanding of astrophysics and your ability to see the big picture impact through all of the chemistry. To both of you, I will never be able to repay to you what you have given me. Thank you.

Second, I need to thank all of the behind-the-scenes help that I have received in my tenure at the University of Colorado, Boulder. Thank you to Don David, Ken Smith, and everyone in the CIRES integrated instrument development facility. You all were integral in maintaining the FA-SIFT, helping with repairs and troubleshooting, and designing and implementing the laser induced acoustic desorption technique. I would not have been able to finish my degree without your expert knowledge and immense amount of patience. A special thank you is extended to Hilkka Kenttämaa and her research group at Purdue for allowing me to visit their laboratory and providing invaluable insight into the LIAD technique. In addition, I want to thank Marshall Wilkinson and everyone in the ChemStore and purchasing

department. Thank you for all the time and effort you put into obtaining all of the dangerous chemicals that I needed.

Lastly, I have to thank all of the great people I have met and have had the opportunity to interact with. Thank you to my lab mates over the years: Oscar Martinez Jr., John Garver, Callie Cole, Charles Nichols, Ditte Thomsen, Zhibo Yang, Nadine Wehres, Jeniffer Herbst, and Zhe-Chen Wang. Thank you all for your collaborations and discussions, guidance and wisdom, and for being great friends. I never thought I would meet a group of people who love sugar as much as I do. In addition, I would like to thank everyone involved in the ion supergroup: the Ellision lab, Lineberger lab, and Weber lab. Thank you all for you help and guidance, and for allowing me to present my research. The last group of people I have to thank are my classmates. I owe a huge thank you to all of you. We worked together, made it through, and now it's on to the next challenge. Congratulations to all of you, and good luck in your next endeavor.

Contents

Chapter

Appendix

Tables

Table

Figures

Figure

Publications

1. Martinez, O., Jr.; Yang, Z.; Demarais, N. J.; Snow, T. P.; Bierbaum, V. M., Gas-phase Reactions of Hydride Anion, H^-. *Astrophys. J.* **2010**, *720*, 173.

2. Demarais, N. J.; Yang, Z.; Martinez, O., Jr.; Wehres, N.; Snow, T. P.; Bierbaum, V. M., Gas-phase Reactions of Polycyclic Aromatic Hydrocarbon Anions with Molecules of Interstellar Relevance. *Astrophys. J.* **2012**, *746*, 32.

3. Demarais, N. J.; Yang, Z.; Snow, T. P.; Bierbaum, V. M., Chemistry of $HCNH^+$: Mechanisms, Structures, and Relevance to Titan's Atmosphere. *Struct. Chem.* **2013**, *24*, 1957.

4. Cole, C. A.; Demarais, N. J.; Yang, Z.; Snow, T. P.; Bierbaum, V. M., Heterocyclic Anions of Astrobiological Interest. *Astrophys. J.* **2013**, *779*, 181.

5. Demarais, N. J.; Yang, Z.; Snow, T. P.; Bierbaum, V. M., Gas-phase Reactions of Polycyclic Aromatic Hydrocarbon Cations and their Nitrogen-Containing Analogs with H Atoms. *Astrophys. J.* **2014**, *784*, 25.

6. Demarais, N. J.; Wang Z.-C.; Snow, T. P.; Bierbaum, V. M., Chemistry of CF^+ and its Relevance to the Interstellar Medium. *J. Phys. Chem. A, in preparation.*

Chapter 1

Gas-Phase Ion Chemistry in Interstellar, Circumstellar, and Planetary Environments

1.1 Introduction

The space between the planets and stars is not empty. In fact, it contains a vast array of atoms, molecules, and dust. This was evident to scientists such as Sir F. W. Herschel as early as the 1700's, who noted areas that were devoid of stars or where the luminosity of some stars appeared drastically diminished compared to those around it [1]. An example of this is Edward Barnard's plate number 5 of the nebulous region in the constellation Taurus (Figure 1.1) [1], which is a visible wavelength image (∼400–700 nm). The dark areas that are devoid of stars indicate the presence of cosmic dust, which blocks light from stars. This space between the stars and planets is termed the interstellar medium (ISM).

In the mid 1800's, scientists Robert Bunsen and Gustav Kirchhoff noted that every element has its own spectral signature and these spectra could be used to identify elements in the laboratory and in the ISM [1, 2]. This discovery was instrumental in developing the field of astrophysics. Extension of the spectroscopic discovery of Bunsen and Kirchhoff from elements to molecules eventually led to the detection and identification of CH, CN, and CH^+ in 1937, 1940, and 1941, respectively [3–7]. Exploration of the ISM and the circumstellar medium (CSM, the area around stars) has lead to the detection of over 180 molecules to date, ranging in size, charge, and composition (Table 1.1) [8].

Most of these molecules have been detected using their rotational signatures in emis-

Figure 1.1: A reproduction of Barnard's plate No. 5 of a nebulous region in the Taurus molecular cloud. This image shows the visible wavelength region. The dark areas that are void of stars indicate the presence of cosmic dust, which blocks light from stars. Photo retrieved from http://www.library.gatech.edu/bpdi/bpdi.php (accessed July 11, 2014).

Table 1.1: Identified interstellar molecules

Neutral				Cation	Anion
CH	C_3N	CO_2	HC_4N	CH^+	OCN^-
CN	H_2CCO	CH_2	CH_2CCHCN	HCO^+	C_6H^-
OH	C_2	CP	c-C_3H_2O	N_2H^+	C_4H^-
NH_3	HNO	H_2CCC	CH_3CONH_2	HCS^+	C_8H^-
H_2O	CH_3CH_2CN	H_2CCCC	CH_3C_6H	$HOCO^+$	C_3N^-
H_2CO	HC_7N	HC_2N	CH_2CNH	HOC^+	C_5N^-
CO	HC_9N	NH	CH_3C_5N	$HCNH^+$	CN^-
H_2	C_4H	CH_4	HCP	H_3O^+	
CH_3OH	NO	C_2O	CH_2CHCH_3	SO^+	
HC_3N	CH_3SH	HCCNC	PO	CO^+	
HCN	HNCS	SiN	CCP	HC_3NH^+	
HCOOH	C_2H_4	HNCCC	NH_2CH_2CN	H_3^+	
SiO	CH_3C_3N	NH_2	PH_3	H_2COH^+	
CS	SiH_4	H_2CN	HCNO	CF^+	
CH_3CN	CH_3C_4H	NaCN	C_2H_5OCHO	H_2O^+	
OCS	C_3O	N_2O	C_3H_7CN	OH^+	
NH_2CHO	c-SiC_2	MgCN	HSCN	H_2Cl^+	
HNC	C_3H	C_8H	AlOH	SH^+	
H_2S	HCl	C_7	C_{60}	HCl^+	
HNCO	c-C_3H_2	CH_3OOH	C_{70}	ℓ-C_3H^+	
CH_3CHO	C_6H	H_2C_6	KCN	C_{60}^+	
CH_3CCH	MgNC	$HC_{11}N$	FeCN	NH_3D^+	
CH_2NH	C_5H	HF	HOOH	H_2NCO^+	
H_2CS	C_2S	c-C_2H_4O	O_2	ArH^+	
SO	C_3S	LiH	HO_2		
CH_3OCH_3	$(CH_3)_2CO$	SiC_3	SH		
CH_2NH_2	NaCl	CH_3	$HCOOCH_3$		
C_2H	AlCl	CH_2OHCHO	HNCNH		
CH_2CHCN	KCl	SiCN	CH_3O		
CH_3CH_2OH	AlF	C_4H_2	CH_3CHNH		
$HCOOCH_3$	c-C_3H	C_6H_2	TiO		
SO_2	PN	c-C_6H_6	TiO_2		
HDO	CH_3CN	CH_2CHOH	CH_3COOCH_3		
SiS	C_3	AlNC	HMgNC		
NS	CH_2CN	FeO	$(NH_2)_2CO$		
NH_2CN	HC_2CHO	$HOCH_2CH_2OH$	CH_3CH_2SN		
HC_5N	C_5	N_2			
HCO	SiC	CH_2CHCHO			
C_2H_2	SiC_4	SiNC			

Notes. Molecules are listed by charge and in chronological order of detection.

sion, while others have been detected by observing their vibrational or electronic emission spectra [8]. There are, of course, limitations to these spectroscopic detection techniques. Only molecules whose laboratory spectra are known can be identified in the ISM or CSM, and not all regions of the electromagnetic spectrum give signatures that are unique to only one molecule. Another complication is that it is difficult to find a line-of-sight with only one molecule-containing region. Moreover, these regions can be different chemically and physically, causing lines or bands to overlay each other. These limitations are evident in the astrophysical phenomena known as the diffuse interstellar absorption bands (DIBs) [9], and the unidentified infrared emission bands (UIRs) [10].

Alternatively, for objects relatively close to earth, such as the planets in our solar system, physical probes can be launched and additional analysis techniques can be employed. The NASA Cassini-Huygens Mission, launched to study Saturn and its moons, included a mass spectrometer, which is able to detect positively charged molecules and ionize and detect neutral species. Unlike spectroscopy, which detects rotational, vibrational and electronic transitions, mass spectrometry detects the mass-to-charge ratio of the species analyzed. The combination of spectroscopy and mass spectrometry has lead to the identification of 17 molecules in the atmosphere of Titan, but many of the detected masses remain unassigned [8, 11–14].

Physical processes such as heating and cooling, photon and electron interactions, stellar winds and shocks help shape all of these environments, but chemistry plays an important role as well. In particular, ion-neutral chemistry in these low density environments becomes important. Many ion-neutral reactions do not exhibit barriers to reaction that often exist for neutral-neutral reactions, and the added ion-dipole or ion-induced dipole interactions lead to enhanced attraction between the two species. The growing field of astrochemistry has highlighted the importance of collaboration among astronomers, astrophysical modelers, and chemists. Through this cooperation, scientists can better describe these environments, make predictions on their origin and evolution, and discover new molecules not yet detected.

1.2 Interstellar and Circumstellar Medium

As is evident by the detection of atoms and molecules in space, the ISM is a diverse place. The composition of the ISM is 99:1 gas to dust by mass. The regions where the gas congregates in higher densities are termed clouds. In our own galaxy the ISM constitutes 10–15% of the mass but most of the volume [15]. In this expanse, interstellar clouds occupy ∼1–2% of the interstellar volume, but contain approximately half the mass of the ISM [15]. The average density of interstellar clouds is $\sim 10^3$ particles cm^{-3}, whereas the density of earth's atmosphere is $\sim 10^{19}$ particles cm^{-3}. In this thesis, I adopt the naming convention of Snow and McCall [16] for different interstellar cloud environments: (1) diffuse atomic, (2) diffuse molecular, (3) translucent, and (4) dense molecular. The different environments are characterized by temperature, density, and typical atomic and molecular abundances (Figure 1.2) [16]. In a simplistic view, one can consider the different interstellar cloud environments as the layers of an onion. The outermost layer is the diffuse atomic environment, followed by the diffuse molecular, then the translucent, and finally the dense molecular. In reality, interstellar clouds are inhomogeneous and irregular in shape, i.e. the Horsehead nebula (Figure 1.3). In addition to interstellar clouds, the CSM is also a complex environment with rich chemistry.

1.2.1 Diffuse Atomic Clouds

Diffuse atomic clouds are fully exposed to the surrounding interstellar radiation field. Because of this, the main constituent is neutral atomic hydrogen, with a small fraction of H_2. All atoms and molecules with ionization energies (IE) less than that of hydrogen are in their cationic state, with minor abundances of the neutral species present as well. The high radiation flux also provides an abundance of electrons. The density in this region is 10–100 particles cm^{-3} and the temperature is 30–100 K. The dominant source of heating in diffuse atomic clouds is UV photons; in an ionization event, part of the energy is utilized to remove

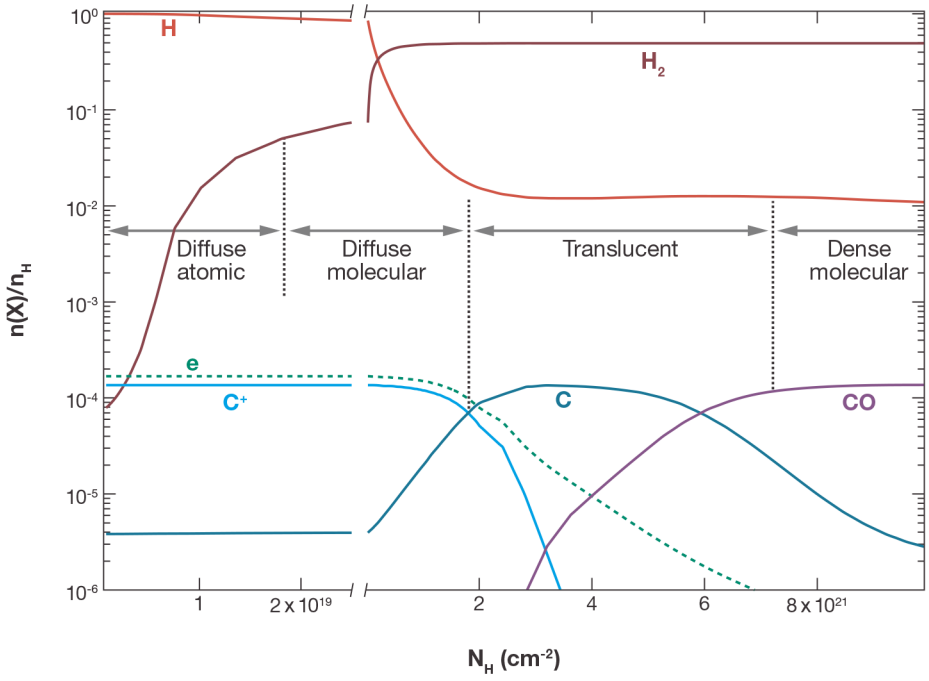

	Diffuse Atomic	Diffuse Molecular	Translucent	Dense Molecular
Defining Characteristic	$f^n_{H_2} < 0.1$	$f^n_{H_2} > 0.1$ $f^n_{C^+} > 0.5$	$f^n_{C^+} < 0.5$ $f^n_{CO} < 0.9$	$f^n_{CO} > 0.9$
A_V (min.)	0	~0.2	~1–2	~5–10
Typ. n_H (cm^{-3})	10–100	100–500	500–5000?	$>10^4$
Typ. T (K)	30–100	30–100	15–50?	10–50
Observational Techniques	UV/Vis H I 21-cm	UV/Vis IR abs mm abs	Vis (UV?) IR abs mm abs/em	IR abs mm em

Figure 1.2: Interstellar cloud environment conditions. (Upper) A graph mapping the ratio of the number density of different atoms and molecules compared to the number density of H atom versus the column density of H. The four different interstellar cloud types are shown in their approximate regions. (Lower) The physical characteristics and defining features of each cloud type are listed. The figure is adapted from Snow and McCall [16].

Figure 1.3: A false color image of the Horsehead nebula seen in the infrared. The darker red areas indicate more dense regions. This figure highlights the irregularity in densities of interstellar environments. Image retrieved from www.nasa.gov.

an electron from the gas and the other fraction is partitioned into translational energy [17].

Polycyclic aromatic hydrocarbons (PAHs) are organic molecules composed of fused five- and six-membered aromatic rings. The aromatic nature of these ringed species make them exceptionally stable, and since carbon is the fourth most abundant element after H, He, and O, they are thought to be prevalent throughout the ISM. Although diffuse atomic clouds are devoid of complex chemistry, most of the DIBs have been detected in this region (Section 1.3). To survive the harsh conditions of the diffuse atomic clouds, the DIB carriers must be very stable; for this reason, PAHs have been proposed as possible carriers. The large flux of interstellar radiation most likely results in ionized PAHs. The chemistry of PAH cations is discussed in Chapter 3.

1.2.2 Diffuse Molecular Clouds

Diffuse molecular clouds are largely shielded from radiation above 13.6 eV, and the hydrogen number density is slightly greater than in diffuse atomic clouds. This causes the fraction of hydrogen in the form of H_2 to become significant ($f^n_{H_2} > 0.1$) [16]. The temperatures are still high (30–100 K) and the density increases slightly ($\sim$100–500 particles cm^{-3}). Because UV radiation is still prevalent in diffuse molecular clouds, C^+ is the dominant form of carbon. Small molecules begin to form, including the first three detected diatomics: CH, CN, and CH^+. Most notably, CF^+ has recently been detected in the Horsehead nebula and the Orion nebula. CF^+ is the most abundant form of fluorine after HF. This molecule has been proposed as a possible DIB carrier and its chemistry is discussed in Chapter 4.

1.2.3 Translucent Clouds

Translucent clouds are the least understood of the four regimes. This region marks a drastic change in the state of carbon, as seen in Figure 1.2. The complex nature of translucent clouds leads to variations in the fractional abundance of carbon. Fractional C^+ abundances are less than 0.5 ($f^n_{C^+} < 0.5$) and the abundance of CO may be as high as 0.9

($f_{CO}^{n} < 0.9$) [16]. This region differs from the diffuse molecular in that C^+ is no longer the dominant form of carbon; however, the abundance of CO is not yet unity. As the density increases (500–5000 particles cm^{-3}) the temperature in these inner clouds decreases (15–50 K). The transition from diffuse molecular to translucent to dense molecular clouds does not have distinct boundaries. This allows mixing between clouds and abundant atoms and molecules in each region to interact. An example of this phenomenon is the hydride anion (H^-). Although H^- has eluded detection in the ISM [18], its existence is generally accepted among the astrochemical community. It is likely that H^- is generated at the interface of translucent and dense molecular clouds. Here, the electron density is still appreciable, but the high density of the molecular cloud shields atoms and molecules from incoming radiation and destruction. Additionally, H^- may be initially formed on the surfaces of grains in translucent clouds and then released into the gas phase [19]. The chemistry of H^- with molecules of interstellar relevance is discussed in Chapter 5.

1.2.4 Dense Molecular Clouds

Dense molecular clouds constitute the most chemically rich environment of the four cloud regions. The densities are $> 10^4$ particles cm^{-3} and because the majority of UV radiation does not penetrate into this region, the temperatures are 10–50 K. Here, the main source of heating is interaction with cosmic rays. Due to the low temperatures in these regions, ion-neutral reactions are important for the evolution of complex chemical species. In 2006, the first interstellar anion was discovered, C_6H^-, in the dark cloud Taurus molecular cloud-1 (TMC-1) [20]. Astronomers had long thought that anions would not survive the harsh conditions of the ISM; however, the subsequent detection of C_8H^- in TMC-1 solidified their existence. A class of important anions that have yet to be detected but hold great promise is deprotonated PAHs ($[PAH–H]^-$) [21–23]. It has been suggested that neutral PAHs associate with free electrons in dense clouds to produce a distribution of neutral and anionic PAHs [24]. However, the electron affinity (EA) of the parent molecules is low (EA 0.5–1 eV) compared

to the EA of their dehydrogenated counterparts (EA 1–2 eV). The chemical reactions of deprotonated PAHs with H atom and molecules of interstellar relevance are discussed in Chapter 6.

Most of the identified interstellar species have been discovered in dense molecular clouds [8]. The high densities allow closer proximity and shield the molecules from incident radiation, allowing complex molecules to form. It is within dense molecular clouds that the next step in the life cycle of interstellar material begins. When the density of gas is high enough, a new star is formed. Star formation and stellar processes are complex and extensive, and the details are not discussed here (cf. Wooden et al. [15], and Snow [25]).

1.2.5 Circumstellar Medium

Intermediate mass stars, similar to the size of our sun, begin to lose matter at a high rate late in their lifetime [24]. This loss can result in a thick layer around the central star, a circumstellar envelope (CSE), that gives rise to complex chemistry, much like dense molecular clouds. Molecules can be formed in the atmosphere of these stars and be expelled into the CSE or be formed in the CSE itself. The star IRC +10216 is one example that has been highly studied by astronomers due to: (1) its close proximity to earth [27], (2) the detection of over 80 molecules, including unusual species such as HMgNC [27, 28], and (3) the identification of 6 anionic species (C_4H^-, C_6H^-, C_8H^-, CN^-, C_3N^-, and C_5N^-) [8]. These discoveries forecast the likely detection of more anions in space, including H^- (Chapter 5) and $[PAH–H]^-$ (Chapter 6).

The star IRC +10216 is believed to be nearing the end of its mass-loss phase and beginning the transition into the preplanetary nebula (PPN) phase. One physical distinction of this transition is the heating of the central star. This heating causes high velocity winds to transform the nearly spherical CSE to an axially symmetric environment as the star continues to expel a large amount of its mass back into the ISM [27, 29, 30]. In addition, as the star heats up, more UV photons are emitted, resulting in evolution of the molecules

located in the CSE. Even though the PPN phase is short-lived, a few hydrocarbons have been detected in the PPN CRL 618, including the first interstellar detection of benzene [30]. This detection of the primary building block for PAHs demonstrates that aromatic species can form and thrive in the CSM and most likely in the ISM.

1.3 Diffuse Interstellar Absorption Bands

The diffuse interstellar bands (DIBs) are characteristic absorption features, observed from the far infrared into the ultraviolet wavelengths of the electromagnetic spectrum, that are much broader and less defined than interstellar atomic transitions. They have been described as the longest standing spectroscopic mystery in astronomy. The first discovery of DIBs by Mary L. Heger in 1922 [31] has sparked over 9 decades of research in discovering new DIBs and finding potential carriers. To date, over 500 DIBs have been identified; however, the origin of these absorption features remains elusive [9]. The tentative assignment of ℓ-C_3H_2 by Maier et al. [32] as a possible DIB carrier is the best candidate to date (Figure 1.4); however, even this species has been challenged [33].

DIBs are seen throughout our own galaxy. The abundance of the strongest DIBs is closely related to the atomic hydrogen abundance and less related to dense molecular clouds or even diffuse clouds [16, 34]. It is largely accepted that the DIB carriers are:

(1) interstellar in origin rather than in, or associated with, the stars themselves [35]. This was shown as early as 1936, when Merrill [35] observed that central wavelengths of the DIBs were stationary in the spectrum of a binary star throughout the motions of the stars.

(2) broad in nature due to the short lifetimes of the electronic excited state [36, 37]. This short lifetime is likely due to rapid internal conversion in molecules [36]. Using a Lorentzian profile, Snow et al. has suggested a lifetime of $\sim 10^{-13}$ s for the DIB seen at 4428 Å. In addition, a lifetime of 10^{-13} s has been proposed for the broad features

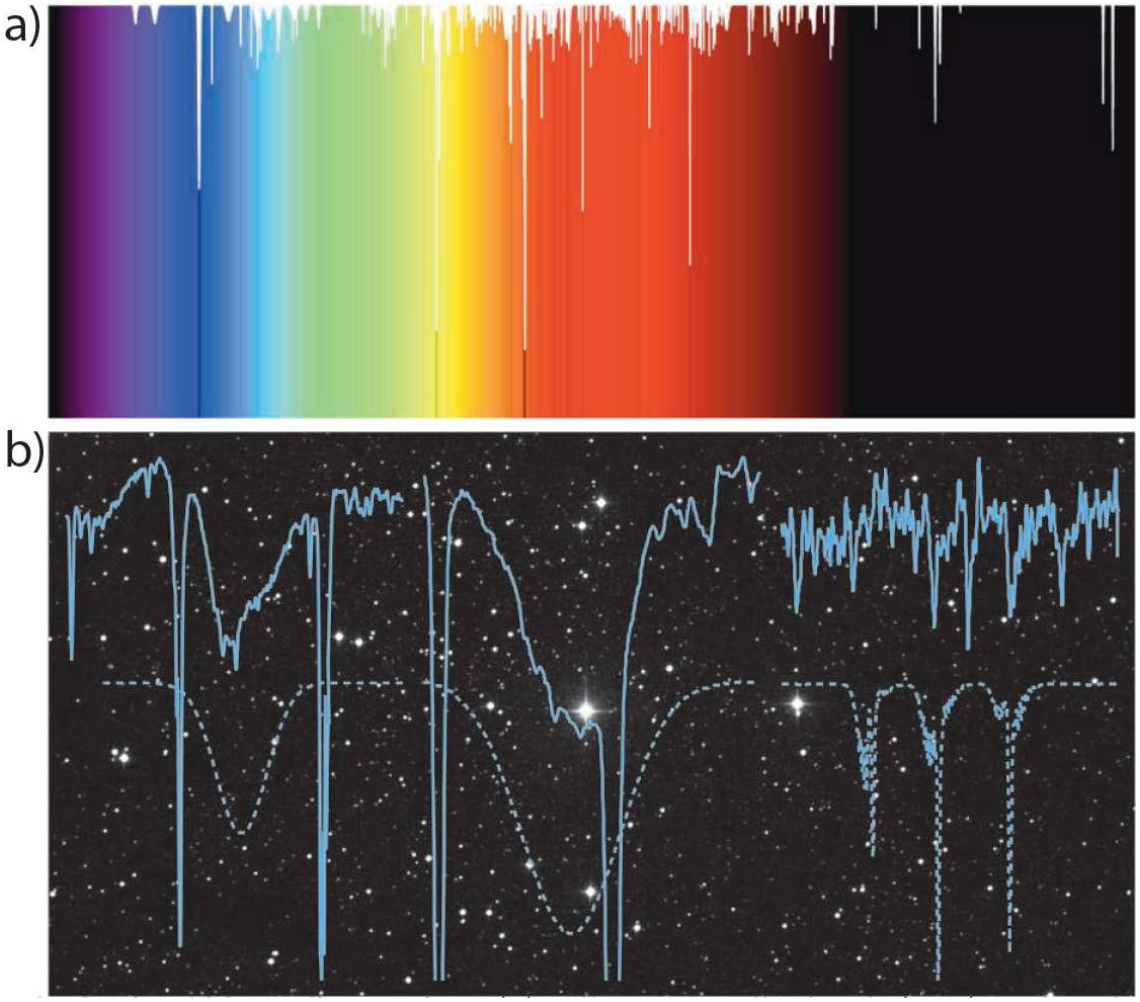

Figure 1.4: The diffuse interstellar absorption bands (DIBs). (a) A compilation of detected DIBs spanning the near-UV to the far IR. (b) The solid curves show DIBs for the wavelength ranges (left to right) 4812 to 4956 Å, 5431 to 5472 Å, and 6144 to 6176 Å, measured from the background star HD 183143 (center). The dashed lines are the simulations of Maier et al. [32] based on their laboratory data for ℓ-C_3H_2. Photo adopted from Oka and McCall [33].

of ℓ-C_3H_2 seen in Figure 1.4 [33]. Although DIBs are broad in nature, structural features, proposed to be partially resolved rotations in the electronic signature of gas-phase molecules, have been observed in some DIBs (cf. Kerr et al. [38]).

(3) likely gas-phase molecules, rather than atoms or grains [9, 16]. The transitions do not match any known atomic spectra, and the wavelength profiles are consistent from sightline to sightline [16]. In addition, some DIB profiles show fine structure, which also suggests gas-phase molecules.

(4) likely composed of the most cosmically abundant elements (H, C, O, N), because they are detected throughout the ISM [16].

Based on these characteristics, PAHs have emerged as possible DIB carriers. Large PAHs of 30 carbon atoms or more have been shown to be stable in the harsh environments where atomic hydrogen dominates [39], and carbon and hydrogen are abundant cosmic elements; PAHs are thought to be abundant throughout the ISM, although individual species have not been definitively identified. In particular, because the UV flux is high in regions where atomic hydrogen is abundant, PAHs in these environments are likely ionized. PAH cations and protonated PAHs show electronic transitions in the visible wavelengths while transitions of neutral PAHs dominate the UV [40, 41]. Due to the abundance of nitrogen in cosmic environments, polycyclic aromatic nitrogen heterocycles (PANHs) should also be considered as possible DIB carriers. Similar to their homocyclic counterparts, PANH cations also exhibit electronic transitions in the visible region [42].

The DIBs show varied intensities in different environments. Therefore, it is reasonable that more than one class of molecules is responsible for the 500 identified features. Recently, the ion CF^+ has been proposed as a carrier of the 1384 Å DIB [43]. This ion is isoelectronic with CO and closely maps the regions where C^+ is abundant [44]. Preliminary ab initio calculations show close correlation for the transition from the $^1\Sigma$ ground state to the $^1\Delta$ excited state; however, no experimental electronic spectrum has been measured [45].

The chemistry of PA(N)H cations and CF^+ are explored in Chapters 3 and 4, respectively, and their chemical stability in the environments dominated by DIBs is examined.

1.4 Unidentified Infrared Emission Bands

Another spectroscopic mystery in astrochemistry that has a widely accepted solution, but no definitive proof, is the origin of the unidentified infrared emission bands (UIRs) [46–48]. Unlike the DIBs, these spectroscopic features are the result of IR photons being released by vibrationally excited interstellar molecules. The strongest detected wavelengths, 3.3, 6.2, 7.7, 8.6, 11.2, 12.7, and 16.4 μm, are characteristic of aromatic species like PAHs [49]. Infrared transitions are characteristic of specific types of vibrations; however, they are not always distinct enough to identify individual molecules. With the aid of experimental and theoretical work, classes of PAHs have been roughly assigned to dominant features of UIRs. While previous attempts to identify specific molecules have been unsuccessful [10, 50], classes of PAHs have been identified as necessary for modeling interstellar spectra. Included in this list are large neutral PAHs, PAH cations, PAH anions, nitrogen-containing PAHs, and PAHs with aliphatic groups. In some interstellar environments, varying sizes of PAHs are needed to accurately fit the observed spectra. It is not surprising that such a wide array of PAHs may exist since the UIRs are ubiquitous throughout the ISM. The work in Chapters 3 and 6 explores the chemistry of PA(N)H cations and deprotonated PAHs, respectively, with an attempt to narrow the range of possible PAHs, as well as search for new classes not previously considered.

1.5 Atmosphere of Titan

In addition to a rich chemical environment in the ISM and CSM, astronomers have discovered other planets and moons with atmospheres where complex chemistry is taking place. One such example is Saturn's moon, Titan. The NASA Cassini-Huygens Mission was launched in 1997, the Cassin-Huygens probe entered Saturn's orbit in 2004, and made its

first flyby through the atmosphere of Titan in 2005. The Cassini probe made its 100th flyby of Titan on March 6, 2014, and has gathered invaluable information about the atmosphere of this earth-like moon [51]. However, unlike the Earth, Titan's atmosphere is dominated by molecular nitrogen and methane. The bombardment of this thick atmosphere by UV photons and other energetic particles results in complex chemistry and physics (Figure 1.5) [12, 52]. The ionosphere of Titan has received considerable attention in recent years [11, 12, 14, 52–55]. This region is of particular interest because Titan's ionosphere is at a critical density where both photochemistry and ion-neutral chemistry can influence the evolution of the environment. In addition, the Cassini probe has collected sufficient data for scientists to begin modeling this complex environment [12–14, 52, 53, 55, 56]. Although models of the physical and chemical processes occurring in Titan's ionosphere have been scrutinized by multiple groups, the overestimation of the $HCNH^+$ abundance by current models, compared to observed densities, still remains a problem. Chapter 7 reexamines the chemistry of $HCNH^+$ with H_2, CH_4, C_2H_2, and C_2H_4 in an attempt to resolve this discrepancy. In addition, new chemical reactions are suggested that were not included in previous models.

1.6 Conclusion

In the past 80 years, astronomers, physicists, and chemists have shown that the environments of space are complex. Although we have learned a great amount about the ISM, CSM, and atmospheres of other planets and moons, many mysteries still remain unsolved. The work in this thesis focuses on the gas-phase chemistry of ions with neutrals.

The flowing afterglow-selected ion flow tube (FA-SIFT; Section 2.2) instrument is ideal for studying ion-neutral gas-phase reactions. A plethora of ionization techniques combined with ion selection allows easy study of ions of interstellar relevance. Here, the study of large, non-volatile PAHs was facilitated by the incorporation of the laser induced acoustic desorption (LIAD; Section 2.3) technique into the FA-SIFT. Ion-neutral reactions are studied with stable, neutral molecules and hydrogen atoms. Pseudo first-order conditions allow for mea-

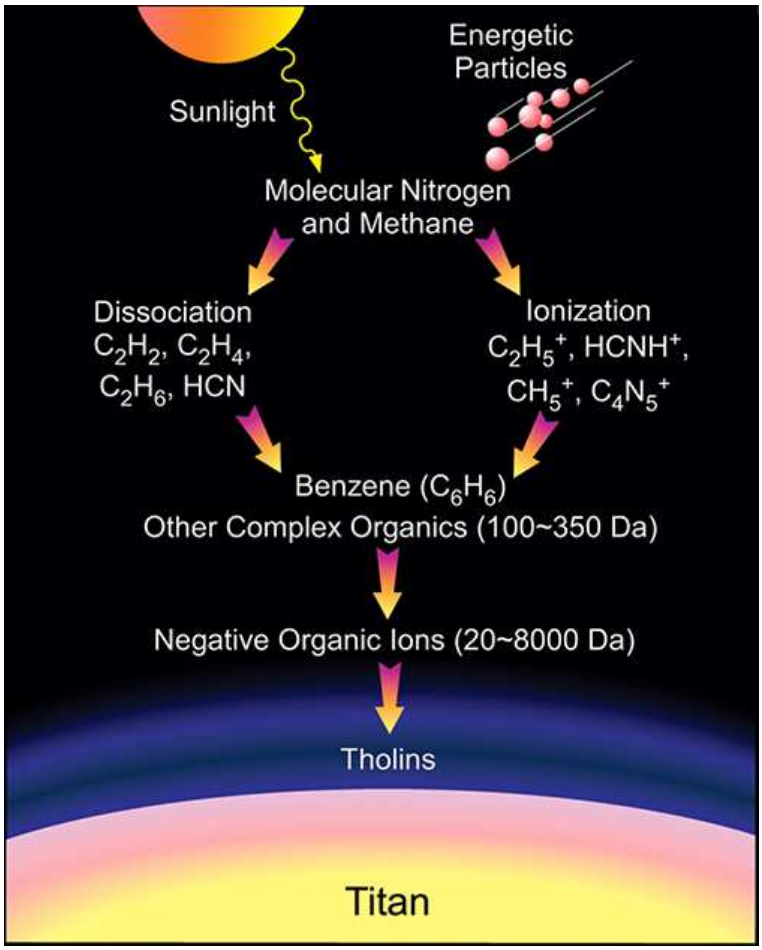

Figure 1.5: The atmosphere of Titan is a complex environment. At the outer reaches atoms and molecules are bombarded by sunlight and high energy particles. In the ionosphere, dissociation and ionization dominate. As the density of the atmosphere increases, more complex molecules emerge, including negative ions. Figure adapted from Waite et al. [52].

surement of reaction rate constants and product distributions. Different collision theories are used to determine reaction efficiencies, which are used to elucidate trends in reactivity. The experimental work is supported by computational chemistry to give insight into reaction thermodynamics as well as reaction mechanisms. The experimental and computational methods are described in Chapter 2.

The reactions of PA(N)H cations with H atoms and other small molecules was carried out to determine the stability of these species. This work continues previous research carried out by our laboratory to include PAHs with differing geometries as well as nitrogen-containing PAHs. The extension to larger PAH cations was made possible by the integration of the LIAD source with the FA-SIFT. Details of the chemistry are presented in Chapter 3.

Chapter 4 moves more deeply into the interstellar cloud "onion" to determine the stability of CF^+ in the extreme environments of photodissociation regions. The viability of CF^+ as a carrier of the DIB at 1384 Å is discussed as related to reactions with neutral molecules present in the same environments.

In dense interstellar clouds, the chemistry of anions becomes important. While the reaction of hydride anion has been recognized as a critical mechanism in the initial cooling immediately after the Big Bang, $H^- + H \longrightarrow H_2 + e^-$, its chemistry with neutral molecules was largely unknown. Chapter 5 investigates the chemistry of H^- with various classes of organic molecules and draws conclusions based on reaction mechanisms.

The detection of negative ions in the past 10 years has highlighted the importance of their inclusion in astrochemical models. PAHs have been accepted to exist in the ISM for many years, but their negative ion chemistry remained unexplored. Chapter 6 investigates the chemistry of deprotonated PAHs with molecules of interstellar relevance to determine their chemical stability in dense regions of the ISM and CSM.

Lastly in Chapter 7, the chemical reactions of $HCNH^+$ with H_2, CH_4, C_2H_2, and C_2H_4 are reexamined to provide insight into the overprediction of $HCNH^+$ in Titan's ionosphere by current astrochemical models. In addition, this work suggests other chemical reactions

that should be included in the current models to fully characterize the destruction rates of $HCNH^+$ in Titan's ionosphere.

1.7 References

1. Yamada, K. M. T.; Winnewisser, G., Eds. In *Interstellar Molecules: Their Laboratory and Interstellar Habitat*. Springer Tracts in Modern Physics; Springer: New York, NY, 2011, Vol. 241.

2. Chemical Heritage Foundation. Robert Bunsen and Gustav Kirchhoff. http://www.chemheritage.org/discover/online-resources/chemistry-in-history/themes/the-path-to-the-periodic-table/bunsen-and-kirchhoff.aspx (accessed July 11, 2014).

3. Swings, P.; Rosenfeld, L., Considerations Regarding Interstellar Molecules. *Astrophys. J.* **1937**, *86*, 483.

4. McKellar, A., Evidence for the Molecular Origin of Some Hitherto Unidentified Interstellar Lines. *Pub. Astron. Soc. Pacific*, **1940**, *52*, 187.

5. Douglas, A. E.; Herzberg, G., Note on CH^+ in Interstellar Space and in the Laboratory. *Astrophys. J.*, **1941**, *94*, 381.

6. Adams, W. S., Some Results with the COUDÉ Spectrograph of the Mount Wilson Observatory. *Astrophys. J.*, **1941**, *93*, 11.

7. Dunham, T., Jr., Interstellar Neutral Potassium and Neutral Calcium. *Pub. Astron. Soc. Pacific*, **1937**, *49*, 26.

8. Woon, D. E. The Astrochymist. http://astrochymist.com (accessed July 11, 2014).

9. McCall, B. J.; Griffin, R. E., On the Discovery of the Diffuse Interstellar Bands. *Proceed. R. Soc. A* **2013**, *469*, 20120604.

10. Cami, J., Analyzing Astronomical Observations with the NASA Ames PAH Database. *EAS Pub. Ser.* **2011**, *46*, 117.

11. Vuitton, V.; Yelle, R. V.; McEwan, M. J., Ion Chemistry and N-Containing Molecules in Titan's Upper Atmosphere. *Icarus* **2007**, *191*, 722.

12. Vuitton, V.; Yelle, R. V.; Lavvas, P., Composition and Chemistry of Titan's Thermosphere and Ionosphere. *Phil. Trans. R. Soc. A* **2009**, *367*, 729.

13. Vuitton, V.; Lavvas, P.; Yelle, R. V.; Galand, M.; Wellbrock, A.; Lewis, G. R.; Coates, A. J.; Wahlund, J. E., Negative Ion Chemistry in Titan's Upper Atmosphere. *Planet. Space Sci.* **2009**, *57*, 1558.

14. Robertson, I. P.; Cravens, T. E.; Waite, J. H., Jr.; Yelle, R. V.; Vuitton, V.; Coates, A. J.; Wahlund, J. E.; Ågren, K.; Mandt, K.; Magee, B.; Richard, M. S.; Fattig, E., Structure of Titan's Ionosphere: Model Comparisons with Cassini Data. *Planet. Space Sci.* **2009**, *57*, 1834.

15. Wooden, D. H.; Charnley, S. B.; Ehrenfreund, P., Composition and Evolution of Interstellar Clouds; University of Arizona Press: Tucson, AZ, 2004; p 33.

16. Snow, T. P.; McCall, B. J., Diffuse Atomic and Molecular Clouds. *Annu. Rev. Astron. Astrophys.* **2006**, *44*, 367.

17. Ferriére, K. M., The Interstellar Environment of our Galaxy. *Rev. Modern Phys.* **2001**, *73*, 1031.

18. Ross, T.; Baker, E. J.; Snow, T. P.; Destree, J. D.; Rachford, B. L.; Drosback, M. M.; Jensen, A. G., The Search for H^- in Astrophysical Environments. *Astrophys. J.* **2008**, *684*, 358.

19. Field, D., H_2 Formation in Space: A Negative Ion Route? *Astron. Astrophys.* **2000**, *362*, 774.

20. McCarthy, M. C.; Gottlieb, C. A.; Gupta, H.; Thaddeus, P., Laboratory and Astronomical Identification of the Negative Molecular Ion C_6H^-. *Astrophys. J. Lett.* **2006**, *652*, L141.

21. Hammonds, M.; Pathak, A.; Candian, A.; Sarre, P. J., Spectroscopy of Protonated and Deprotonated PAHs. *EAS Pub. Ser.* **2011**, *46*, 373.

22. Carelli, F.; Gianturco, F., Electron Angular Distributions and Attachment Rates in o-Benzyne and Phenyl Aromatic Molecules: The Effect of the Permanent Dipoles. *Eur. Phys. J. D* **2013**, *67*, 1.

23. Gao, J.; Berden, G.; Oomens, J., Laboratory Infrared Spectroscopy of Gaseous Negatively Charged Polyaromatic Hydrocarbons. *Astrophys. J.* **2014**, *787*, 170.

24. Wakelam, V.; Herbst, E., Polycyclic Aromatic Hydrocarbons in Dense Cloud Chemistry. *Astrophys. J.* **2008**, *680*, 371.

25. Snow, T. P., *The Dynamic Universe: An Introduction to Astronomy*, 4th ed.; West Publishing Company: St. Paul, MN, 1991.

26. Males, J. R.; Close, L. M.; Skemer, A. J.; Hinz, P. M.; Hoffmann, W. F.; Marengo, M., Four Decades of IRC +10216: Evolution of a Carbon-Rich Dust Shell Resolved at 10 μm with MMT Adaptive Optics and MIRAC4. *Astrophys. J.* **2012**, *744*, 133.

27. Agúndez, M.; Fonfría, J. P.; Cernicharo, J.; Kahane, C.; Daniel, F.; Guélin, M., Molecular Abundances in the Inner Layers of IRC +10216. *Astron. Astrophys.* **2012**, *543*, A48.

28. Cabezas, C.; Cernicharo, J.; Alonso, J. L.; Agúndez, M.; Mata, S.; Guélin, M.; Peña, I., Laboratory and Astronomical Discovery of Hydromagnesium Isocyanide. *Astrophys. J.* **2013**, *775*, 133.

29. Davis, C. J.; Smith, M. D.; Gledhill, T. M.; Varricatt, W. P., Near-Infrared Echelle Spectroscopy of Protoplanetary Nebulae: Probing the Fast Wind in H_2. *Mon. Not. R. Astron. Soc.* **2005**, *360*, 104.

30. Cernicharo, J.; Heras, A. M.; Tielens, A. G. G. M.; Pardo, J. R.; Herpin, F.; Guélin, M.; Waters, L. B. F. M., Infrared Space Observatory's Discovery of C_4H_2, C_6H_2, and Benzene in CRL 618. *Astrophys. J. Lett.* **2001**, *546*, L123.

31. Heger, M. L., Further Study of the Sodium Lines in Class B Stars. *Lick Observatory Bullet.* **1922**, *10*, 141.

32. Maier, J. P.; Walker, G. A. H.; Bohlender, D. A.; Mazzotti, F. J.; Raghunandan, R.; Fulara, J.; Garkusha, I.; Nagy, A., Identification of H_2CCC as a Diffuse Interstellar Band Carrier. *Astrophys. J.* **2011**, *726*, 41.

33. Oka, T.; McCall, B. J., Disclosing Identities in Diffuse Interstellar Bands. *Science* **2011**, *331*, 293.

34. Herbig, G. H., The Diffuse Interstellar Bands. *Annu. Rev. Astron. Astrophys.* **1995**, *33*, 19.

35. Merrill, P. W., Stationary Lines in the Spectrum of the Binary Star Boss 6142. *Astrophys. J.* **1936**, *83*, 126.

36. Snow, T. P., Search for Fine Structure within the 4430 Å Diffuse Interstellar Band. *Astrophys. J.* **2002**, *567*, 407.

37. Snow, T. P.; Zukowski, D.; Massey, P., The Intrinsic Profile of the 4428 Å Diffuse Interstellar Band. *Astrophys. J.* **2002**, *578*, 877.

38. Kerr, T. H.; Hibbins, R. E.; Fossey, S. J.; Miles, J. R.; Sarre, P. J., Ultrafine Structure in the λ5797 Diffuse Interstellar Absorption Band. *Astrophys. J.* **1997**, *495*, 941.

39. Le Page, V.; Snow, T. P.; Bierbaum, V. M., Hydrogenation and Charge States of Polycyclic Aromatic Hydrocarbons in Diffuse Clouds. II. Results *Astrophys. J.* **2003**, *584*, 316.

40. Hammonds, M.; Pathak, A.; Sarre, P. J., TD-DFT Calculations of Electronic Spectra of Hydrogenated Protonated Polycyclic Aromatic Hydrocarbon (PAH) Molecules: Implications for the Origin of the Diffuse Interstellar Bands? *Phys. Chem. Chem. Phys.* **2009**, *11*, 4458.

41. Rouillé, G.; Steglich, M.; Carpentier, Y.; Jäger, C.; Huisken, F.; Henning, T.; Czerwonka, R.; Theumer, G.; Börger, C.; Bauer, I.; Knölker, H.-J., On the Relevance of Polyynyl-substituted Polycyclic Aromatic Hydrocarbons to Astrophysics. *Astrophys. J.* **2012**, *752*, 25.

42. Dryza, V.; Sanelli, J. A.; Robertson, E. G.; Bieske, E. J., Electronic Spectra of Gas-Phase Polycyclic Aromatic Nitrogen Heterocycle Cations: Isoquinoline$^+$ and Quinoline$^+$. *J. Phys. Chem. A* **2012**, *116*, 4323.

43. Roueff, E. Observatoire de Paris-Meudon, LUTH, 5 Place Jules Janssen, F-92190 Meudon, France. Personal communication, 2014.

44. Guzmán, V.; Pety, J.; Gratier, P.; Goicoechea, J. R.; Gerin, M.; Roueff, E.; Teyssier, D., The IRAM-30m Line Survey of the Horsehead PDR. *Astron. Astrophys.* **2012**, *543*, L1.

45. Petsalakis, I. D.; Theodorakopoulos, G., Electronic states of CF^+. *Chem. Phys.* **2000**, *254*, 181.

46. Léger, A.; Puget, J. L., Identification of the Unidentified IR Emission Features of Interstellar Dust? *Astron. Astrophys.* **1984**, *137*, L5.

47. Allamandola, L. J.; Tielens, A. G. G. M.; Barker, J. R., Polycyclic Aromatic Hydrocarbons and the Unidentified Infrared Emission Bands: Auto Exhaust Along the Milky Way! *Astrophys. J.* **1985**, *290*, L25.

48. Allamandola, L. J.; Hudgins, D. M.; Sandford, S. A., Modeling the Unidentified Infrared Emission with Combinations of Polycyclic Aromatic Hydrocarbons. *Astrophys. J. Lett.* **1999**, *511*, L115.

49. Tielens, A. G. G. M., Interstellar Polycyclic Aromatic Hydrocarbon Molecules. *Annu. Rev. Astron. Astrophys.* **2008**, *46*, 289.

50. Bauschlicher, C. W., Jr.; Boersma, C.; Ricca, A.; Mattioda, A. L.; Cami, J.; Peeters, E.; Sánchez de Armas, F.; Puerta Saborido, G.; Hudgins, D. M.; Allamandola, L. J., The NASA Ames Polycyclic Aromatic Hydrocarbon Infrared Spectroscopic Database: The Computed Spectra. *Astrophys. J. Supp. Ser.* **2010**, *189*, 341.

51. Piazza, E. Flybys. Munsell, K., Ed. http://saturn.jpl.nasa.gov/mission/flybys/ (accessed July 11, 2014).

52. Waite, J. H., Jr.; Young, D. T.; Cravens, T. E.; Coates, A. J.; Crary, F. J.; Magee, B.; Westlake, J., The Process of Tholin Formation in Titan's Upper Atmosphere. *Science* **2007**, *316*, 870.

53. Vuitton, V.; Yelle, R. V.; Anicich, V. G., The Nitrogen Chemistry of Titan's Upper Atmosphere Revealed. *Astrophys. J. Lett.* **2006**, *647*, L175.

54. Thissen, R.; Vuitton, V.; Lavvas, P.; Lemaire, J.; Dehon, C.; Dutuit, O.; Smith, M. A.; Turchini, S.; Catone, D.; Yelle, R. V.; Pernot, P.; Somogyi, A.; Coreno, M., Laboratory Studies of Molecular Growth in the Titan Ionosphere. *J. Phys. Chem. A* **2009**, *113*, 11211.

55. Westlake, J. H.; Waite, J. H., Jr.; Mandt, K. E.; Carrasco, N.; Bell, J. M.; Magee, B. A.; Wahlund, J. E., Titan's Ionospheric Composition and Structure: Photochemical Modeling of Cassini INMS Data. *J. Geophys. Res.* **2012**, *117*, E01003.

56. Magee, B. A.; Waite, J. H., Jr.; Mandt, K. E.; Westlake, J.; Bell, J.; Gell, D. A., INMS-Derived Composition of Titan's Upper Atmosphere: Analysis Methods and Model Comparison. *Planet. Space Sci.* **2009**, *57*, 1895.

Chapter 2

Methods

2.1 Introduction

Ion-neutral chemistry in the gas-phase is an important process in environments where densities are sparse, like the interstellar medium (ISM), circumstellar medium (CSM), and atmospheres of planets and moons. The flowing afterglow-selected ion flow tube (FA-SIFT) is advantageous for studying gas-phase ion processes. An assortment of ion generation techniques combined with ion selection enables the study of a variety of ions ranging from small species, like H^- and CF^+, to large molecules, like $C_{14}H_9^-$ and $C_{18}H_{12}^+$. The laser induced acoustic desorption (LIAD) technique was incorporated into the FA-SIFT to facilitate the study of large, non-volatile species, like PAH ions (Section 2.3). The ions are entrained in a flow of helium allowing gas-phase reactions with stable molecules and hydrogen atoms at a known temperature. The experiments are conducted under pseudo first-order conditions, and reaction rate constants and product ion distributions are determined. Different ion-neutral collision theories are used to determine reaction efficiencies, which are used to elucidate trends in reactivity. The experimental work is supported by computational analyses to give insight into reaction thermodynamics, reactivity trends, and reaction mechanisms.

2.2 Flowing Afterglow-Selected Ion Flow Tube Technique

The FA-SIFT instrument is utilized to study ion-neutral reactions. The flowing afterglow (FA) technique was initially developed by Ferguson, Fehsenfeld, and Schmeltekopf to

study reactions relevant to Earth's atmosphere [1]. This technique has several useful features for studying ion-neutral reactions; however, it has limitations. Complex molecules are difficult to study due to the large number of ions that can be produced by electron ionization. The incorporation of the selected ion flow tube (SIFT), by Adams and Smith [2], allowed for the study of individual ionic species. A variety of ions can be generated simultaneously and selected for individual measurement. The arrangement of the FA-SIFT instrument utilized in this work consists of four distinct regions: (1) ion production flow tube, (2) ion selection region, (3) reaction flow tube, and (4) detection region (Figure 2.1). Detailed descriptions of the instrument and its many components have been published and this thesis will provide only an overview of the apparatus [3–6].

2.2.1 Ion Production Flow Tube

The ion production flow tube is made of stainless steel and has an inner diameter of 7.3 cm. Helium gas is introduced at the farthest upstream position, ∼75 cm from the ion-skimming nose cone. Two movable, ringed gas inlets allow for the introduction of neutral gases or liquid vapors at variable distances inside the flow tube. In addition, several inlets exist along the flow tube for the introduction of solid species. The LIAD technique has been incorporated into the ion production flow tube for the introduction of large, non-volatile species (Section 2.3). To produce the array of ions studied in this work, various ionization techniques have been employed including electron, chemical, and Penning ionization (Section 2.4). After the formation event, the ions are carried downstream by the flowing He gas. A skimming nose cone with a 2 mm diameter is held at a potential that is attractive to the charged species of interest. The central portion of the ion beam enters the ion selection region and the neutral gas is removed by a high capacity roots blower.

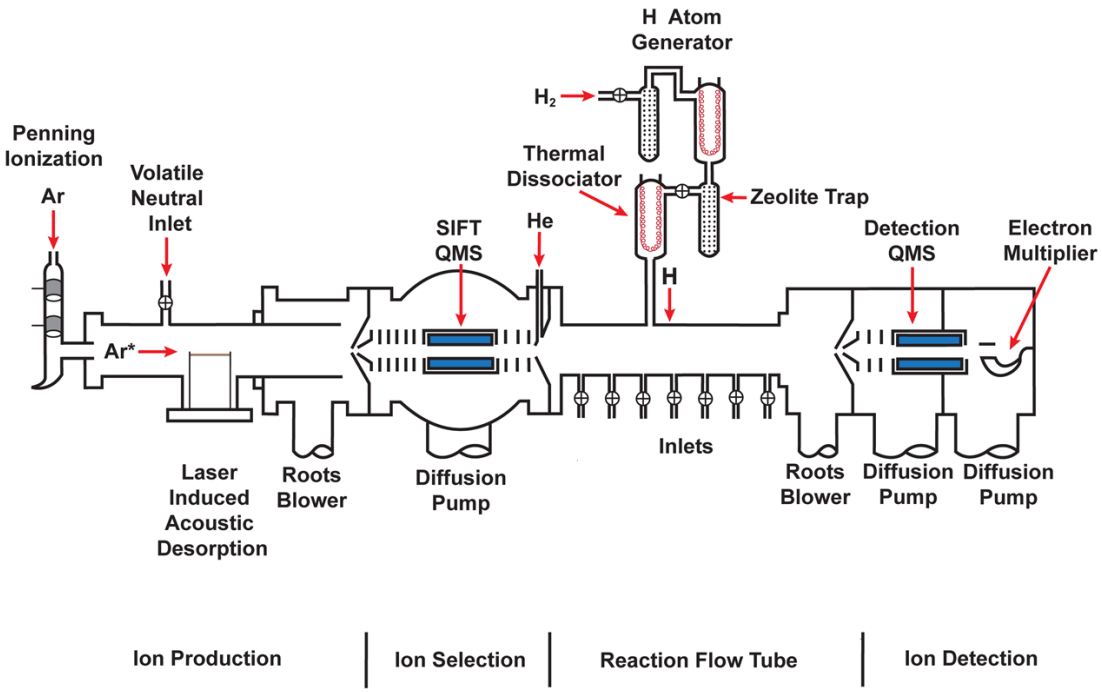

Figure 2.1: FA-SIFT apparatus. Ions are generated in the ion production region using various ionization techniques. Large non-volatile organics are introduced into the flow tube using the LIAD technique. Generated ions are then mass-selected by a quadrupole mass filter, and injected into the reaction flow tube, where stable neutrals are introduced through a manifold of inlets. Ion intensities are measured as a function of reaction distance using a quadrupole mass filter coupled to an electron multiplier. Alternatively, H atoms are introduced at a fixed inlet. The subsequent decrease in reactant-ion signal is monitored as a function of H atom concentrations.

2.2.2 Ion Selection Region

The ion selection region is a low pressure chamber ($\sim 1 \times 10^{-5}$ Torr) that is used to select and focus ions of one mass-to-charge ratio (m/z). Ions are extracted from the ion production flow tube into the ion selection region by electric fields generated by a cone shaped electrode immediately after the skimming nose cone. This region is pumped by a 10-inch diffusion pump. Two ring electrodes transport the ions away from the inlet and allow efficient pumping of the neutral gas that has passed through the small orifice. Next, an Einzel lens is used to focus the ion beam into the entrance of a quadrupole analyzer, which is differentially pumped by a 6-inch diffusion pump (not shown in Figure 2.1), and ions of a single m/z are selected. These ions then enter a second Einzel lens, where they are refocused into the entrance of a Venturi inlet. The low pressure region created by the design of the Venturi inlet facilitates efficient transport of the ions from the low pressure ion selection region into the high pressure reaction flow tube.

Figure 2.2 shows the mass spectrum of (a) unSIFTed C^+ (m/z 12), produced by electron ionization of CO, (b) unSIFTed CF^+ (m/z 31), generated by the reaction of C^+ with F_2, and (c) SIFTed CF^+, which demonstrates the advantage of the SIFT technique.

2.2.3 Reaction Flow Tube

Similar to the ion production flow tube, ionic species that enter the reaction flow tube are entrained in a flow of helium gas (7–15 std atm L min^{-1}, P_{He} = 0.3–0.5 Torr) and the ions are collisionally cooled before the addition of neutral reactants. The neutral molecule concentration is chosen by increasing the flow of the neutral until the reactant ion intensity decreases to $\sim$10% of the initial intensity for the longest reaction distance (77 cm). Stable, neutral molecules are introduced through a manifold of inlets and allowed to react. The central portion of the ion beam enters the ion detection region through a second skimming nose cone, and the neutral gas is removed by a high capacity roots blower. Alternatively,

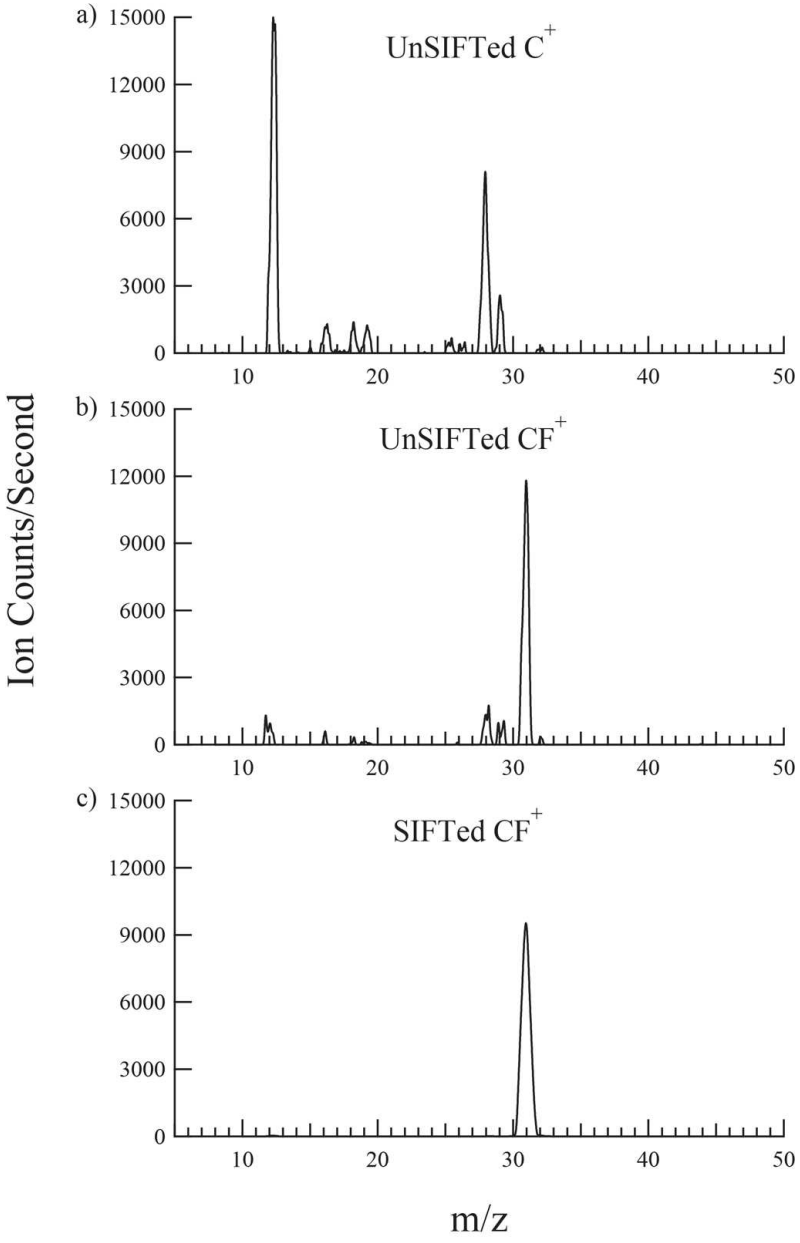

Figure 2.2: Mass spectrum of a) UnSIFTed C^+, b) UnSIFTed CF^+, and c) SIFTed CF^+. (a) C^+ (m/z 12) is generated by electron ionization of CO. A number of other cations are produced as well. (b) F_2 is subsequently added to the ion production flow tube and CF^+ (m/z 31) is generated by the reaction $C^+ + F_2 \longrightarrow CF^+ + F$. (c) The CF^+ ion is isolated and injected into the reaction flow tube.

hydrogen atoms may be introduced at a fixed distance and allowed to react with the ion of interest (Section 2.5).

2.2.4 Ion Detection Region

Upon entering the ion detection region, an Einzel lens is used to focus the ion beam into the entrance of a differentially pumped quadrupole mass analyzer. Electrostatic lenses, positioned at the exit of the quadrupole, guide the ions into a channeltron electron multiplier and the ions are detected. Figure 2.3 shows the reaction of $CF^+ + CD_3OD$ with introduction of the neutral at intlets 1, 4, and 7. As the reaction distance (reaction time) increase, the CF^+ ion intensity decreases and the product ion intensities increase. Determination of reaction rate constants as a function of reaction distance or hydrogen atom concentration is detailed in Sections 2.6.1 and 2.6.2, respectively.

2.3 Laser Induced Acoustic Desorption

Large carbonaceous species such as PA(N)Hs are difficult to study in the gas phase due to their extremely low vapor pressure and high melting point. We utilize the LIAD technique to attain sufficient densities of large, nonvolatile, neutral species in the gas phase. The neutral molecules are subsequently ionized upon desorption (Figure 2.4). This method has been well characterized previously for many different mass spectrometric applications [7–10]. Although coronene cation has been studied in our FA-SIFT instrument previously, this required extreme temperatures and large quantities of solid coronene. The LIAD technique requires no heating and much less solid sample to attain similar ion intensities. Consequently, we have adapted this setup to our FA-SIFT to generate sufficient concentrations of tetracene cation in the gas-phase (Figure 2.5).

First, a known amount of analyte is dissolved in a volatile solvent and deposited on a thin titanium foil (12.7 μm, Alfa Aesar). Multiple application techniques were explored including dipping the foil, adding the solution to the foil drop wise and allowing it to dry

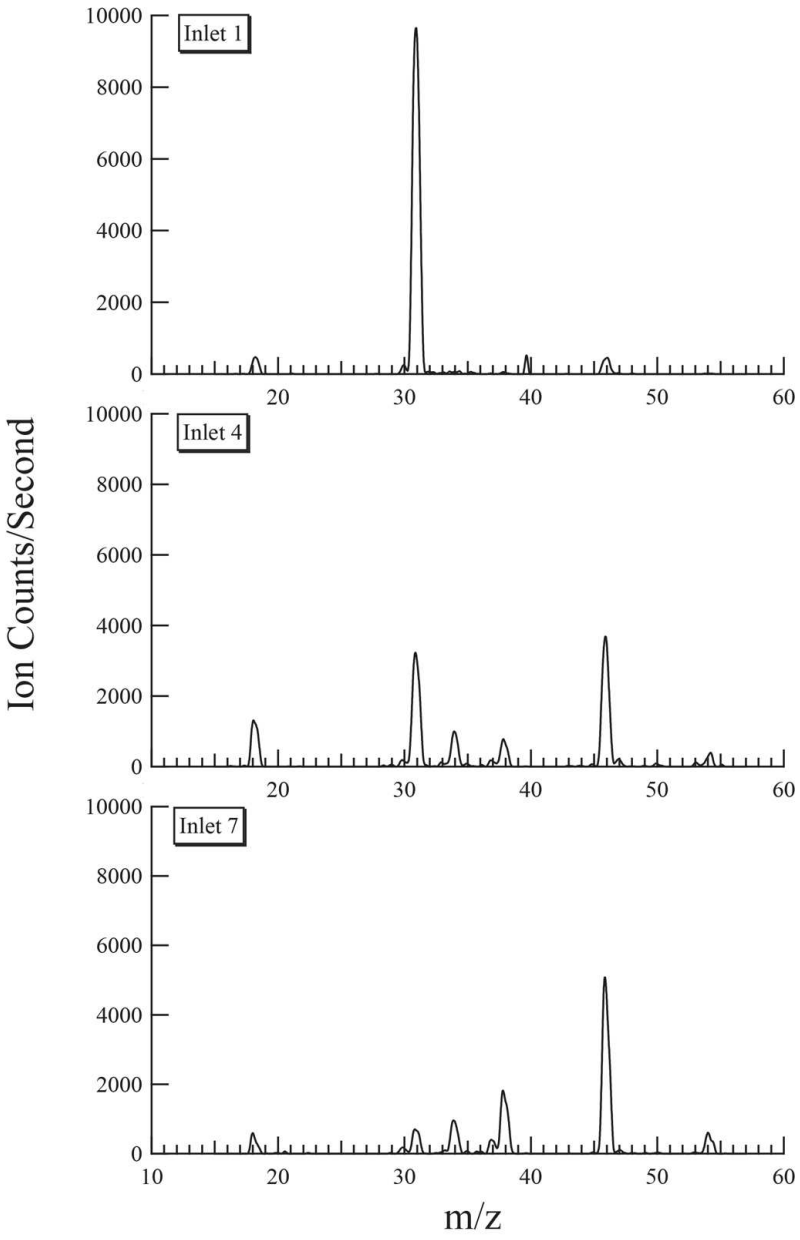

Figure 2.3: Mass spectrum for the reaction of CF^+ + CD_3OD with introduction of the neutral molecules at inlets 1, 4, and 7. The intensity of CF^+ decreases and the intensity of the product ions increase as the reaction distance increases.

with and without heat, spin-coating, and airbrushing. Using a fixed-flow airbrush (Badger 200nh), we were able to apply a uniform coating of the analyte to a 3.1 cm diameter foil. While benzene is an efficient solvent for large PAH molecules, aerosolic benzene is extremely toxic. The airbrush technique has the advantages of efficient solvent evaporation, which eliminates the aggregation effects seen in the other three techniques, and control of the analyte concentration. This allows the use of less toxic solvents, like ethanol. For sufficiently volatile solvents, no drying time is needed. After the analyte is applied to the foil, it is mounted on a probe where it is held in place between two stainless steel rings. The probe is inserted into the ion production flow tube so that the foil is held in the center and desorption is perpendicular to the He flow (Figure 2.1, 2.4, 2.5). An unfocused, pulsed laser beam (Continuum Minilite II, Nd:YAG, 532 nm, 3 mm beam diameter, 15 Hz, 25 mJ pulse^{-1}) is directed through an optically thin window into the ion production region toward the metal foil. The laser light impinges on the uncoated side of the foil, desorbing the intact, neutral analyte into the gas phase [11]. The laser beam is scanned to produce a continuous source of neutral analyte. Different scanning schemes were analyzed including random spot selection, spirals, vertical and horizontal methods. Starting at the upstream end of the foil, scanning vertically and subsequently moving downstream to obtain a new desorption area provides the most uniform ion intensities. The scanning procedure is achieved by a motorized mirror mount (Thorlabs KS1-Z8). A scan rate of 0.04 mm s^{-1} was found to give sufficient ion intensity while allowing maximum time per foil. This scan rate results in a desorption area of $\sim 8 \times 10^{-3}$ mm^2 per shot and an experiment duration of 45 minutes per foil. Electronically excited argon atoms or He^+ (Section 2.4) are generated upstream from the sample probe and the neutral analyte is subsequently ionized upon desorption. Ion intensities are directly correlated with laser power, which is consistent with previous work [8, 12].

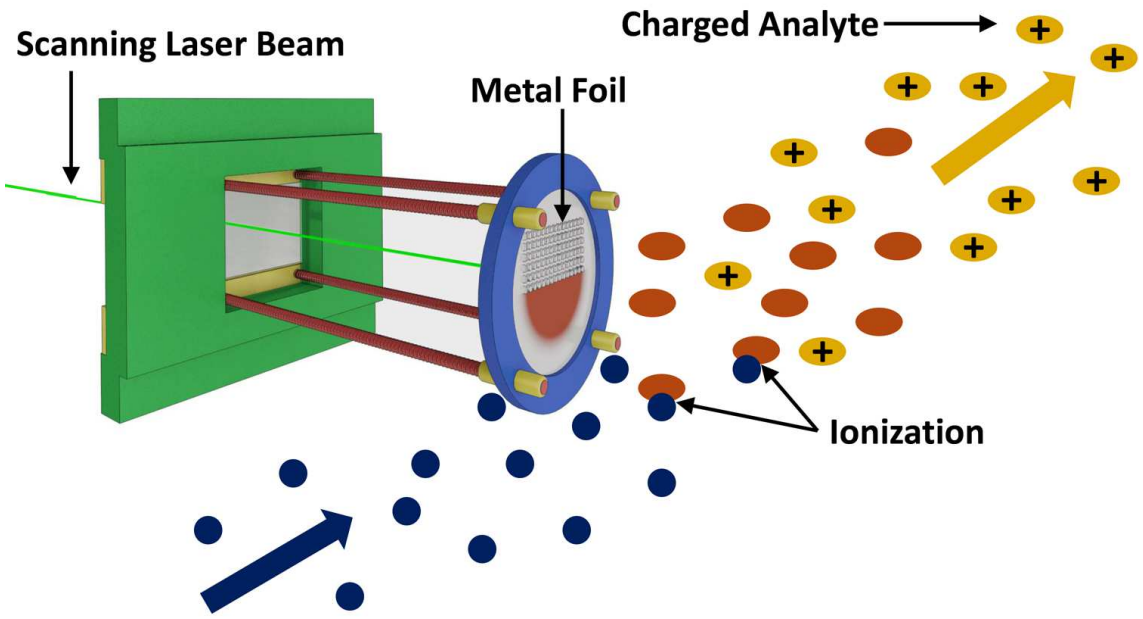

Figure 2.4: Laser induced acoustic desorption (LIAD) assembly. Ionized species produced upstream of the assembly (blue) interact with desorbed molecules (orange) to generate the ion of interest (yellow). The figure is adapted from an image produced by Ben Cole.

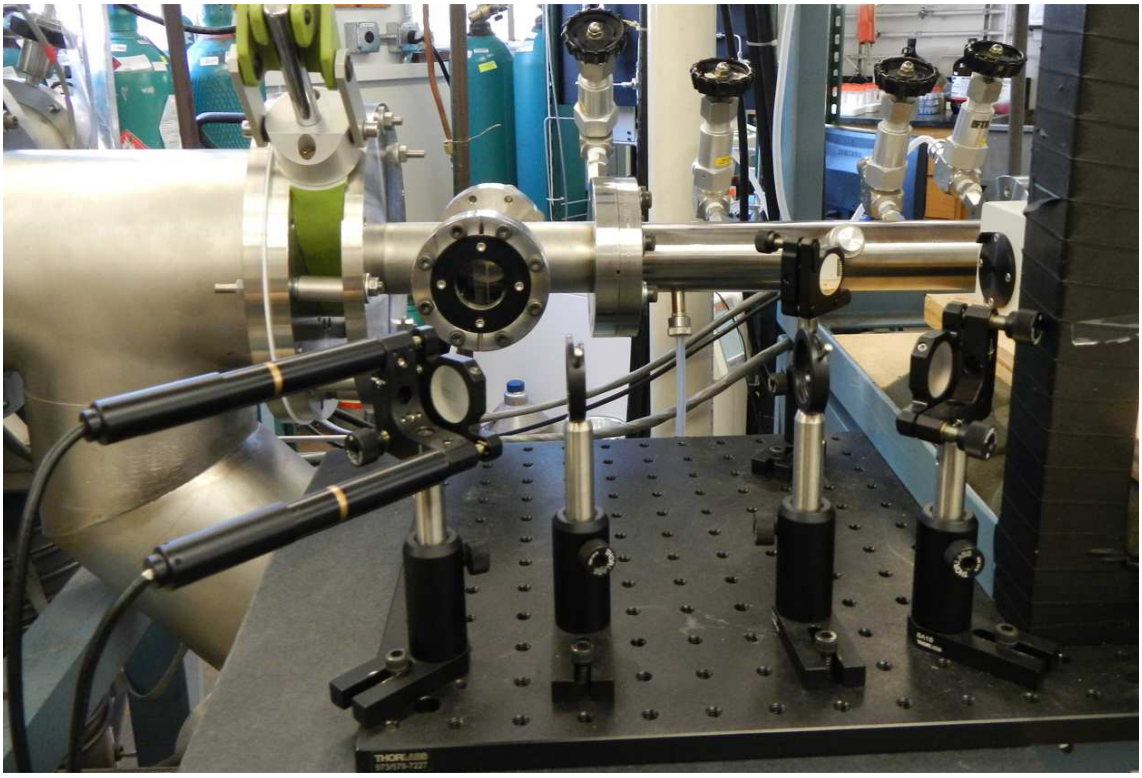

Figure 2.5: An image of the LIAD setup integrated into the FA-SIFT. The two movable lens mounts on the right are used to direct the laser light to the center of the movable mirror. The movable mirror on the left is controlled by preprogrammed movements. An optically thin window allows the laser light to enter the ion production region.

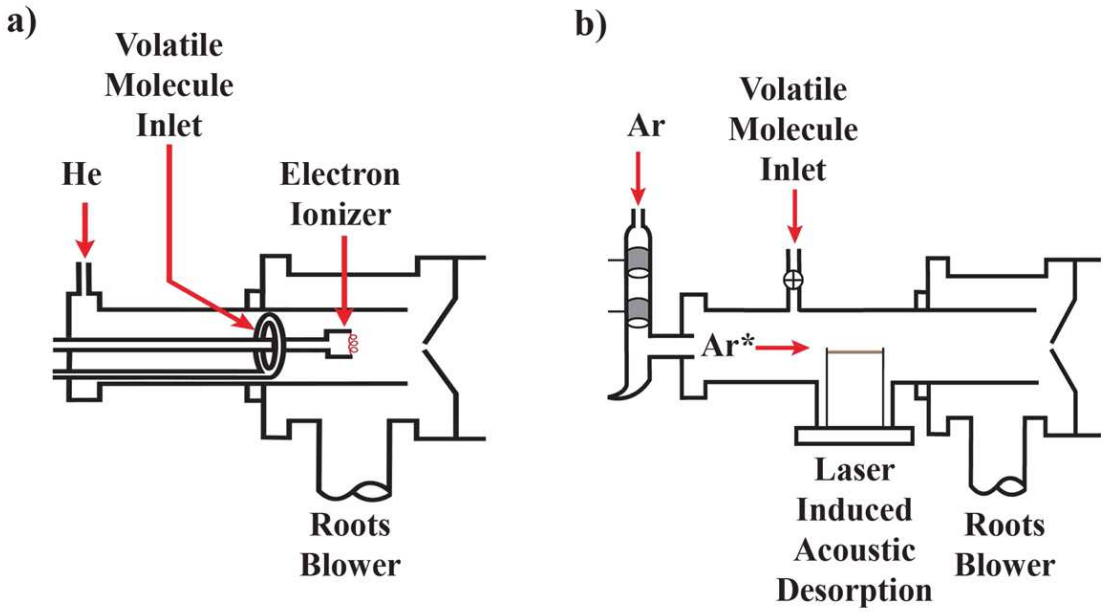

Figure 2.6: Schematic figures of the ion production region with different ionization and neutral introduction sources: (a) Electron ionization with a movable inlet neutral source, and (b) Penning ionization with the LIAD assembly.

2.4 Ion Formation

In this work, electron ionization, chemical ionization, and Penning ionization were used to generate the ions studied in Chapters 3–7 (Figure 2.6).

Electron ionization can be used to generate the ion of interest directly or indirectly via chemical ionization. In this work, a voltage bias is placed across an yttrium oxide coated iridium filament (4 V, 6 A). The filament is held at a potential 70 V more negative than the potential of the extraction grid. The low work function of the filament causes a current of electrons (1 μA–3 mA) to accelerate toward the grid, ionizing the gas medium, and resulting in a plasma (cations, anions, and electrons). For efficient ion transmission into the ion selection region, a flow tube pressure of ∼0.2–0.3 Torr He is maintained and ionization events usually occur less than 15 cm from the skimming nose cone. However, in the case of PAH cations, the ionization event takes place ∼35 cm from the skimming nose cone. This distance is extended due to the limitations of introducing adequate concentrations of solid samples into the ion production flow tube.

Alternatively, Penning ionization can be used to generate cationic species. In this work, argon gas flows through a hollow cathode dc discharge tube ($F_{Ar} = 2$ std atm L min^{-1}; Figure 2.6). A potential bias is placed on two hollow tantalum cylinders, located inside the discharge tube, with the anode downstream from the cathode. Electrons discharged from the anode interact with the gas to produce excited argon atoms [13]. The $^3P_2$ state of electronically excited Ar (Ar*) is the most probable metastable electron configuration. The $^3P_0$ and the $^1P_1$ states having similar energies and will be populated as well. The highest density of Ar* is generated when the potential difference is near the minimum threshold for initiating the discharge (∼200 V). It is likely that the excited state argon forms a short lived complex with the neutral molecule of interest. A valence electron from the neutral molecule fills the hole created in the metastable argon and the excited electron is subsequently released,

$$M + Ar^* \longrightarrow [M\text{–}Ar]^* \longrightarrow M^+ + Ar + e^-. \tag{2.1}$$

The energy difference between the ground state Ar($^1S_0$) and the first excited state Ar($^3P_2$) is 11.5 eV making this technique advantageous for organic molecules. Most organic molecules have ionization energies between 7 and 10 eV. The small excess of energy ensures minimal fragmentation during the ionization event [14].

2.5 Hydrogen Atom Generation

Atomic hydrogen is generated by flowing H_2 over a hot tungsten filament. A flow of high purity H_2 gas (99.999 %) is passed through a liquid nitrogen cooled, molecular sieve trap, flowed over a heated tungsten pre-dissociation filament, purified again by a liquid nitrogen cooled, molecular sieve trap, and flowed over a heated tungsten dissociation filament (Figure 2.1). The dissociation filaments are housed in water cooled quartz tubes [15]. The H/H_2 gas is transferred to the reaction flow tube through a Teflon tube. Atomic hydrogen is introduced into the reaction flow tube at a fixed reaction distance 75 cm from the detection nosecone. The reactant ion signal is monitored as a function of filament voltage, U, using a quadrupole mass filter coupled to an electron multiplier. The filament voltage is directly correlated to the concentration of atomic hydrogen. For the conditions used in this work (flow of H_2 = 8 std cm^3 s^{-1} and U = 35–70 V), only 1% of the H_2 is dissociated into H atom upon entry into the reaction flow tube. Although microwave discharge of H_2 is much more efficient (30% dissociation) [16], microwave sources require a slightly impure H_2 source to operate properly, and the heated filament generates a reproducible and variable H atom source without varying the H_2 flow [17]. The dissociation of H_2 on a hot filament is proposed as a catalytic two step process [18]:

$$W^* + H_2 \longleftrightarrow H + WH, \tag{2.2}$$

$$WH \longleftrightarrow W^* + H. \tag{2.3}$$

Direct measurement of the H atom concentration using an isothermal calorimeter, similar to that of Trainor et al. [15], has proved difficult due to the low H atom production in our

instrument. Here, calibration reactions are used to determine the concentration of H atoms as a function of filament voltage. For the reactions of PA(N)H cations with H atom, the calibration reaction with benzene cation was used:

$$C_6H_6^+ + H \longrightarrow C_6H_7^+, \tag{2.4}$$

$$\longrightarrow C_6H_5^+ + H_2, \tag{2.5}$$

with a known reaction rate constant of $k = 2.2 \times 10^{-10}$ cm^3 s^{-1} [19]. In the case of H atom reactions with anions, the calibration reaction with Cl^- was used:

$$H + Cl^- \longrightarrow HCl + e^-; \tag{2.6}$$

where $k = 9.6 \times 10^{-10}$ cm^3 s^{-1} [17].

2.6 Reaction Rate Constant Determination

Rate constants for reaction of ions with neutral molecules and hydrogen atom are determined using two different methods. Rate constants for ion-molecule reactions are determined by varying the reaction distance, while keeping the neutral concentration constant. Rate constants for ion-H atom reactions are determined by varying the H atom concentration at a fixed reaction distance. The expressions for determining each rate constant using experimental values are detailed in the subsections below.

2.6.1 Ion-Molecule Reactions

A generic bimolecular reaction between ion $A^\pm$ and neutral molecule N can be described as:

$$A^\pm + N \xrightarrow{k_{exp}} B^\pm + M. \tag{2.7}$$

The second order differential rate equation for monitoring the change in $A^\pm$ is

$$\frac{d[A^\pm]}{dt} = -k_{exp}\ [A^\pm\ ]\ [N]. \tag{2.8}$$

Because the concentration of the neutral molecule, N, is more than 2 orders of magnitude larger than that of the ion, the concentration of N remains unchanged. Under these pseudo first-order conditions the concentration of N can be approximated as a constant value. Thus, the integrated pseudo first-order rate equation is

$$\ln\frac{[\mathrm{A}^{\pm}]_{\mathrm{t}}}{[\mathrm{A}^{\pm}]_0} = -k_{\mathrm{exp}}\ [\mathrm{N}]\ \mathrm{t}, \tag{2.9}$$

where $[\mathrm{A}^{\pm}]_t$ is the concentration of $\mathrm{A}^{\pm}$ at any time t, $[\mathrm{A}^{\pm}]_0$ is the concentration of $\mathrm{A}^{\pm}$ at time zero, k_{exp} is the experimental bimolecular rate constant, [N] is the concentration of the neutral molecule N, and t is the reaction time. The reaction time is not directly measured. However, the ion velocity is determined by the helium flow and the reaction distance is a known quantity. Thus, solving the velocity equation for t,

$$\mathrm{t} = \frac{\mathrm{z}}{\mathrm{v}_{A^{\pm}}}. \tag{2.10}$$

Due to friction at the walls of the reaction flow tube, the helium carrier gas has a lower velocity at the walls and a higher velocity toward the center of the flow tube. Moreover, there is a radial gradient in ion density since ions are neutralized by collisions with the walls. Since the ions are concentrated on axis, where the helium velocity is greatest, their average velocity is greater than the average helium velocity. Thus, a previously measured velocity correction factor, $\alpha = 1.6$, must be included in Equation 2.10 to accurately describe the velocity of the ions. Thus,

$$\mathrm{v}_{A^{\pm}} = \alpha \cdot \mathrm{v}_{\mathrm{He}}, \tag{2.11}$$

$$\mathrm{t} = \frac{\mathrm{z}}{\alpha \cdot \mathrm{v}_{\mathrm{He}}}, \tag{2.12}$$

and the integrated rate equation becomes

$$\ln\frac{[\mathrm{A}^{\pm}]_{\mathrm{z}}}{[\mathrm{A}^{\pm}]_0} = \frac{-k_{\mathrm{exp}}\ [\mathrm{N}]\ \mathrm{z}}{\alpha \cdot \mathrm{v}_{\mathrm{He}}}. \tag{2.13}$$

The change in ion intensity, $[A^{\pm}]_z$, as a function of reaction distance, z, can be monitored for the seven neutral reactant inlets. Thus Equation 2.13 can be rearranged to

$$\frac{d\ln\frac{[A^{\pm}]_z}{[A^{\pm}]_0}}{dz} = \frac{-k_{\exp}\ [N]}{\alpha \cdot v_{He}}. \tag{2.14}$$

Since the initial ion intensity, $[A^{\pm}]_0$, is a constant value for the experiment, Equation 2.14 reduces to

$$\frac{d\ln[A^{\pm}]}{dz} = \frac{-k_{\exp}\ [N]}{\alpha \cdot v_{He}}. \tag{2.15}$$

Solving Equation 2.15 for $k_{\exp}$ results in an expression for the bimolecular rate constant,

$$k_{\exp} = -\frac{d\ln[A^{\pm}]}{dz}\frac{\alpha \cdot v_{He}}{[N]}. \tag{2.16}$$

Equation 2.16 takes on the form of y = -mx; where y = $k_{\exp}$, m = $\frac{d\ln[A^{\pm}]}{dz}$, and x = $\frac{\alpha \cdot v_{He}}{[N]}$. The natural logarithm of the ion intensities can be plotted as a function of reaction distance. This plot has a linear fit where the slope is equal to the change in ion intensity as a function of reaction distance, $\frac{d\ln[A^{\pm}]}{dz}$ (Figure 2.7). The ion intensity decreases as the reaction distance increases, and therefore reaction time increases. This inverse relationship results in a negative slope, which results in a positive value for $k_{\exp}$. The quantities α, v_{He}, and [N] are all measureable values. The mean velocity of the helium can be determined by knowing the flow of the helium (F_{He}), the cross-sectional area of the flow tube (πr_{FT}^2), and the pressure of helium in the flow tube (P_{He}). The flow of the helium, F_{He}, is measured by a helium flow meter that has been calibrated to ensure accurate measurement. The F_{He} is reported in units of std atm L min^{-1}. A temperature correction factor from standard temperature to experimental temperature, T, must be added to all equations where F_{He} is included,

$$F_{He}\left(\frac{\text{std atm L}}{\text{min}}\right) \cdot \left(\frac{\text{T (K)}}{273.16\ \text{K}}\right). \tag{2.17}$$

Equation 2.17 gives the corrected flow of helium at the experimental temperature. The radius of the flow tube is a known value, r_{FT} = 3.65 cm, and the helium pressure in the

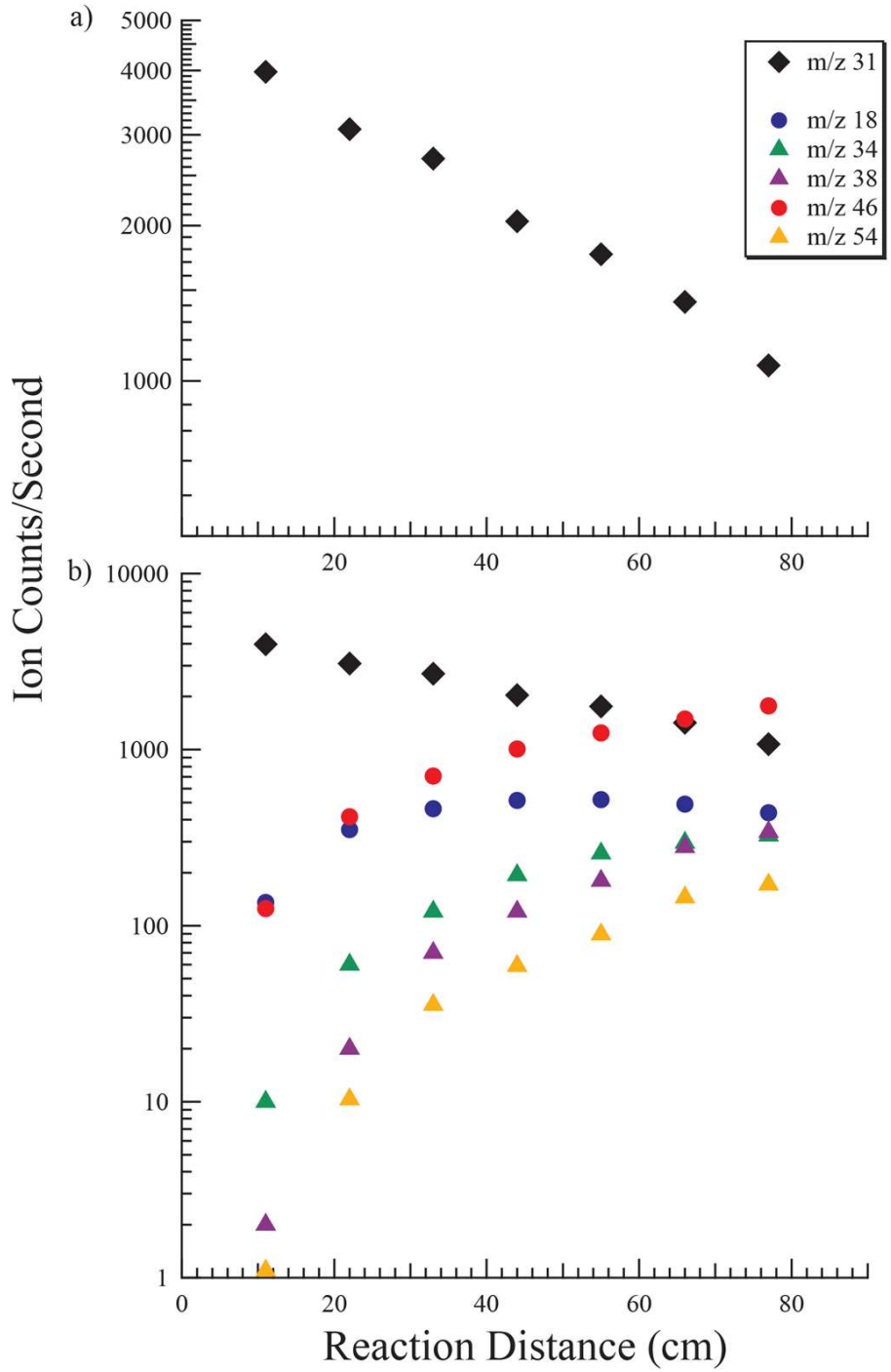

Figure 2.7: Plots of ion intensities (ion counts s^{-1}) on a logarithmic scale as a function of reaction distance (cm) for the reaction $CF^+ + CD_3OD$. (a) Plot of CF^+ intensity as a function of reaction distance, and (b) plot of all ion intensities as a function of reaction distance.

flow tube is measured with a differential pressure Baratron. Equation 2.18 describes this relationship with appropriate unit conversions,

$$\begin{aligned} v_{He}\left(\frac{cm}{s}\right) = \frac{F_{He}\left(\frac{\text{std atm L}}{\text{min}}\right)}{\pi r_{FT}^2\ (\text{cm})^2 \cdot P_{He}\ (\text{Torr})} \cdot \left(\frac{1000\ \text{cm}^3}{1\ \text{L}}\right) \\ \cdot \left(\frac{1\ \text{min}}{60\ \text{s}}\right) \cdot \left(\frac{760\ \text{Torr}}{1\ \text{atm}}\right) \cdot \left(\frac{T\ (\text{K})}{273.16\ \text{K}}\right). \end{aligned} \tag{2.18}$$

The concentration of neutral molecules, [N], is related to the pressure of the neutral molecules, P_N, through the ideal gas law. P_N can be determined by measuring the flow of the neutral, F_N, the pressure in the flow tube, P_{He}, and the flow of helium, F_{He},

$$P_N = \frac{F_N \cdot P_{He}}{F_{He}}. \tag{2.19}$$

The measurement of the helium pressure and the flow of helium have been described above. The flow of neutral molecules is determined by measuring the change in pressure as a function of time in a glass rack with a calibrated volume (V_{GR}). The pressure in an external glass rack is measured by a second differential pressure Baratron, which is integrated into a LabVIEW program that determines the value of $\frac{dP_N\ (\text{Torr})}{dt\ (\text{s})}$. The flow of neutral molecules is measured at room temperature, so a correction factor is not needed. These measurable values are related to the flow of the neutral by Equation 2.20,

$$F_N\left(\frac{\text{Torr cm}^3}{\text{s}}\right) = \frac{dP_N\ (\text{Torr})}{dt\ (\text{s})} \cdot V_{GR}\ (\text{cm}^3). \tag{2.20}$$

Similar to the helium flow temperature correction, a temperature dependent unit conversion must be included when converting concentration from a pressure to a particle density. Using the ideal gas law,

$$\begin{aligned} P \cdot \frac{V}{n}\left(\frac{\text{Torr cm}^3}{\text{particle}}\right) &= R \cdot T\left(\frac{\text{Torr cm}^3}{\text{particle}}\right) \\ &= 0.08206\left(\frac{\text{atm L}}{\text{mol K}}\right) \cdot T\ (\text{K}) \cdot \left(\frac{760\ \text{Torr}}{1\ \text{atm}}\right) \\ &\quad \cdot \left(\frac{1000\ \text{cm}^3}{1\ \text{L}}\right) \cdot \left(\frac{1\ \text{mol}}{6.0221 \times 10^{23}\ \text{particle}}\right) \\ &= \frac{T\ (\text{K})}{9.6565 \times 10^{18}\left(\frac{\text{particle K}}{\text{Torr cm}^3}\right)}. \end{aligned} \tag{2.21}$$

The neutral concentration, [N], is equated to the values described above by Equation 2.22,

$$[\mathrm{N}]\left(\frac{\text{particle}}{\text{cm}^3}\right) = \frac{\mathrm{F_N}\left(\frac{\text{Torr cm}^3}{\text{s}}\right)\mathrm{P_{He}}\ (\text{Torr})}{\mathrm{F_{He}}\left(\frac{\text{std atm L}}{\text{min}}\right)} \cdot \left(\frac{1\ \text{atm}}{760\ \text{Torr}}\right) \cdot \left(\frac{1\ \text{L}}{1000\ \text{cm}^3}\right) \cdot \left(\frac{60\ \text{s}}{1\ \text{min}}\right) \cdot \left(\frac{9.6565 \times 10^{18}\left(\frac{\text{particle K}}{\text{Torr cm}^3}\right)}{\text{T (K)}}\right) \cdot \left(\frac{273.16\ \text{K}}{\text{T (K)}}\right). \tag{2.22}$$

Including the new descriptions of the helium velocity and concentration of the neutral in terms of measurable quantities, Equation 2.16 gives

$$k_{\text{exp}}\left(\frac{\text{cm}^3}{\text{particle s}}\right) = -\frac{d\ln[\mathrm{A}^{\pm}]}{dz}\left(\frac{1}{\text{cm}}\right) \cdot \frac{\alpha \cdot \mathrm{F_{He}^2}\left(\frac{\text{std atm L}}{\text{min}}\right)^2}{\mathrm{F_N}\left(\frac{\text{Torr cm}^3}{\text{s}}\right)\mathrm{P_{He}^2}\ (\text{Torr})^2\ \pi \mathrm{r_{FT}^2}\ (\text{cm})^2} \cdot \left(\frac{760\ \text{Torr}}{1\ \text{atm}}\right)^2 \cdot \left(\frac{1000\ \text{cm}^3}{1\ \text{L}}\right)^2 \cdot \left(\frac{1\ \text{min}}{60\ \text{s}}\right)^2 \cdot \left(\frac{\text{T (K)}}{273.16\ \text{K}}\right)^2 \cdot \left(\frac{\text{T (K)}}{9.6565 \times 10^{18}\left(\frac{\text{particle K}}{\text{Torr cm}^3}\right)}\right). \tag{2.23}$$

To simplify Equation 2.23, the constants in the conversion factors can be combined into one expression,

$$\begin{aligned} \mathrm{C} &= \frac{\alpha}{\pi \mathrm{r_{FT}^2}(\text{cm})^2} \cdot \left(\frac{760\ \text{Torr}}{1\ \text{atm}}\right)^2 \cdot \left(\frac{1000\ \text{cm}^3}{1\ \text{L}}\right)^2 \cdot \left(\frac{1\ \text{min}}{60\ \text{s}}\right)^2 \cdot \left(\frac{1}{273.16\ \text{K}}\right)^2 \cdot \left(\frac{1}{9.6565 \times 10^{18}\left(\frac{\text{particle K}}{\text{Torr cm}^3}\right)}\right) \\ &= 8.512 \times 10^{-18}\left(\frac{\text{cm}^7\ \text{min}^2\ \text{Torr}^3}{\text{L}^2\ \text{s}^2\ \text{atm}^2\ \text{K}^3\ \text{particle}}\right). \end{aligned} \tag{2.24}$$

With appropriate units included, Equation 2.23 becomes,

$$k_{\text{exp}}\left(\frac{\text{cm}^3}{\text{particle s}}\right) = -\frac{d\ln[\mathrm{A}^{\pm}]}{dz}\left(\frac{1}{\text{cm}}\right) \cdot \frac{\mathrm{F_{He}^2}\left(\frac{\text{std atm L}}{\text{min}}\right)^2 \mathrm{T}^3(\text{K})^3}{\mathrm{F_N}\left(\frac{\text{Torr cm}^3}{\text{s}}\right)\mathrm{P_{He}^2}\ (\text{Torr})^2} \cdot \mathrm{C}\left(\frac{\text{cm}^7\ \text{min}^2\ \text{Torr}^3}{\text{L}^2\ \text{s}^2\ \text{atm}^2\ \text{K}^3\ \text{particle}}\right). \tag{2.25}$$

Finally, the expression for the determination of a generic bimolecular rate constant under pseudo first-order conditions in the FA-SIFT instrument can be simply described as,

$$k_{\text{exp}}\left(\frac{\text{cm}^3}{\text{particle s}}\right) = -\frac{d\ln[\mathrm{A}^{\pm}]}{dz} \cdot \frac{\mathrm{F_{He}^2\ T^3}}{\mathrm{F_N\ P_{He}^2}} \cdot 8.512 \times 10^{-18}. \tag{2.26}$$

For each reported ion-molecule rate constant, at least nine rate constants are measured over three different days. Neutral molecule concentrations and helium flows are varied to ensure there is no dependance of the rate constant on [N] or F_{He}.

2.6.2 Ion-H Atom Reactions

Alternatively, ion-H atom reaction rate constants are determined by varying the concentration of H atoms, [H], at a fixed reaction distance. This can be described by rearranging Equation 2.16,

$$k_{\text{exp}} = -\frac{d\ln[\text{A}^{\pm}]}{d[\text{H}]} \cdot \frac{\alpha \cdot \text{v}_{He}}{\text{z}}. \tag{2.27}$$

Since [H] cannot be directly measured, calibration reactions are used (Section 2.5). The rate constant equation for the calibration ion $\text{C}^{\pm}$ is equivalent to Equation 2.27. For a given value of $\frac{\alpha \cdot \text{v}_{He}}{\text{z}}$ the following relationship holds,

$$\frac{k_{\text{A}^{\pm}}}{\frac{d\ln[\text{A}^{\pm}]}{d[\text{H}]}} = \frac{k_{\text{C}^{\pm}}}{\frac{d\ln[\text{C}^{\pm}]}{d[\text{H}]}}. \tag{2.28}$$

Equation 2.28 can be rearranged to solve for $k_{\text{A}^{\pm}}$,

$$k_{\text{A}^{\pm}} = k_{\text{C}^{\pm}} \cdot \frac{\frac{d\ln[\text{A}^{\pm}]}{d[\text{H}]}}{\frac{d\ln[\text{C}^{\pm}]}{d[\text{H}]}}. \tag{2.29}$$

As described previously, the concentration of H atoms is directly related to the voltage applied to the tungsten filament, U,

$$k_{\text{A}^{\pm}} = k_{\text{C}^{\pm}} \cdot \frac{\frac{d\ln[\text{A}^{\pm}]}{d\text{U}}}{\frac{d\ln[\text{C}^{\pm}]}{d\text{U}}}. \tag{2.30}$$

Similar to the ion-neutral molecule reactions, a plot of the natural logarithm of the ion intensities as a function of filament voltage has a linear fit where the slope is equal to $\frac{d\ln[\text{X}^{\pm}]}{d\text{U}}$. The filament voltage for H atom generation is varied to produce different concentrations. Multiple voltage cycles are carried out and the slopes of $\frac{d\ln[\text{X}^{\pm}]}{d\text{U}}$ are averaged (Figure 2.8). Thus, $k_{\text{C}^{\pm}}$ is a known value that has been previously measured, $\frac{d\ln[\text{A}^{\pm}]}{d\text{U}}$ and $\frac{d\ln[\text{C}^{\pm}]}{d\text{U}}$ are determined experimentally, and $k_{\text{A}^{\pm}}$ is calculated using Equation 2.30.

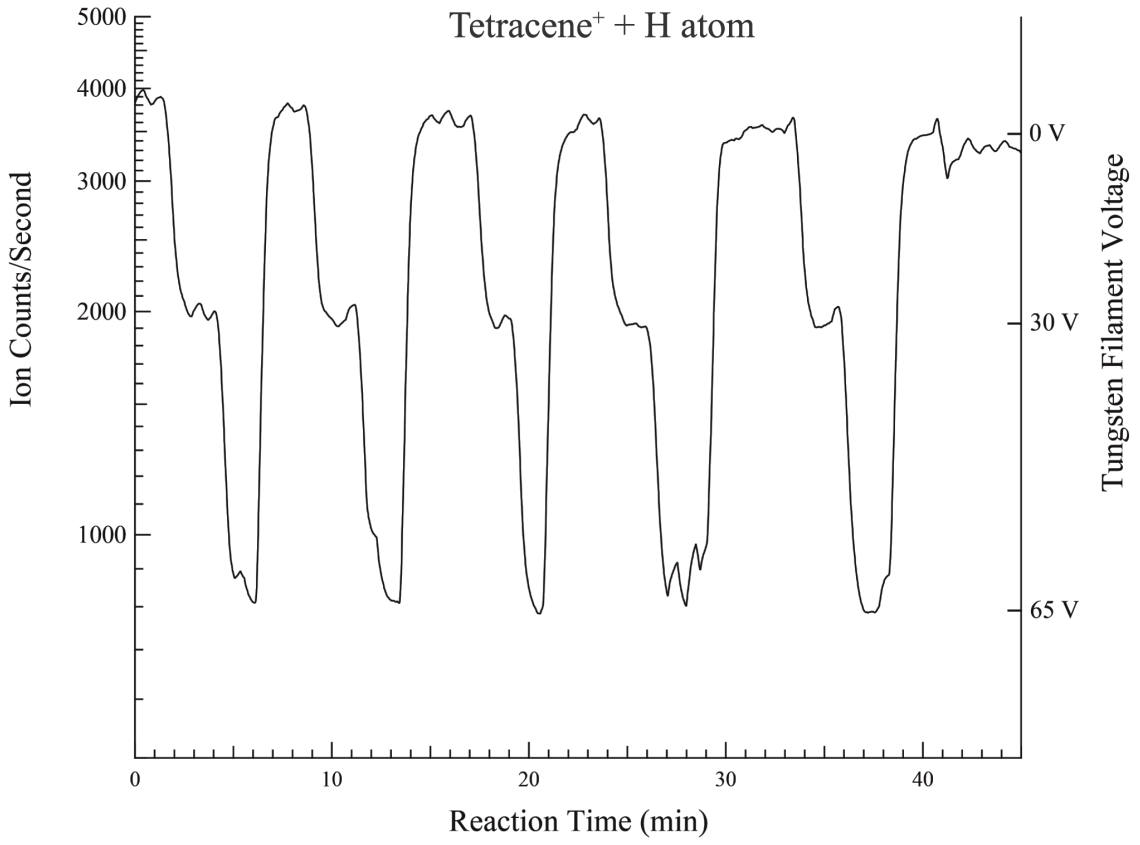

Figure 2.8: Plot of ion intensities (ion counts s^{-1}; on a logarithmic scale; left) and filament voltage (right) as a function of reaction time for the reaction of tetracene$^+$ with H atom. LIAD coupled with electron ionization is used to generate tetracene cations. The filament voltage for H_2 dissociation is varied to produce different H atom concentrations. Multiple voltage cycles are carried out and the slopes $\frac{d\ln[X^{\pm}]}{dU}$ are averaged.

2.7 Product Distribution Determination

Some ion-neutral reactions may result in multiple ionic products. For these reactions, product distributions are measured to determine the rate constant for each process. Many factors may influence the measurement of this distribution including: (1) non-uniform diffusion of all ions (2) non-uniform detection of all ions, and (3) secondary reactions. Large ions diffuse more slowly, resulting in lower loss rates at the walls and higher densities in the reaction flow tube. However, large ions generally have lower detection efficiencies. This inverse relationship usually allows for the detection of small and large ions without the introduction of a correction factor. This approach is tested for all reactions with multiple ionic products by comparing the total detected ion count at each of the seven inlets. To account for secondary reaction, the ratio of an individual product ion versus the total product ion intensity is plotted versus (1) fraction of parent ion remaining or (2) reaction distance. Primary product distributions are determined by extrapolating to (1) zero reaction of parent ion or (2) zero reaction distance (Figure 2.9). Using this method, secondary products intersect the y-axis at zero intensity. The values obtained by both analysis techniques are combined and an average product distribution is reported. Only product fractions greater than or equal to 0.10 are reported and there is an associated error of $\pm 30\%$ of the reported value.

2.8 Radiative Association Rate Constant Determination

Some ion-neutral reactions result in an association product. The ion and neutral form a new bond and the energy from this process is transferred into the molecules resulting in an excited complex with a limited lifetime,

$$\mathrm{A}^+ + \mathrm{B} \underset{k_{-1}}{\overset{k_1}{\rightleftharpoons}} \mathrm{AB}^{*+}. \tag{2.31}$$

Complexes with a large number of degrees of freedom, like protonated PAHs, live long enough that the excess energy can be removed by collisions or emission of radiation before the complex dissociates. In the interstellar medium, where densities are low, radiative stabilization

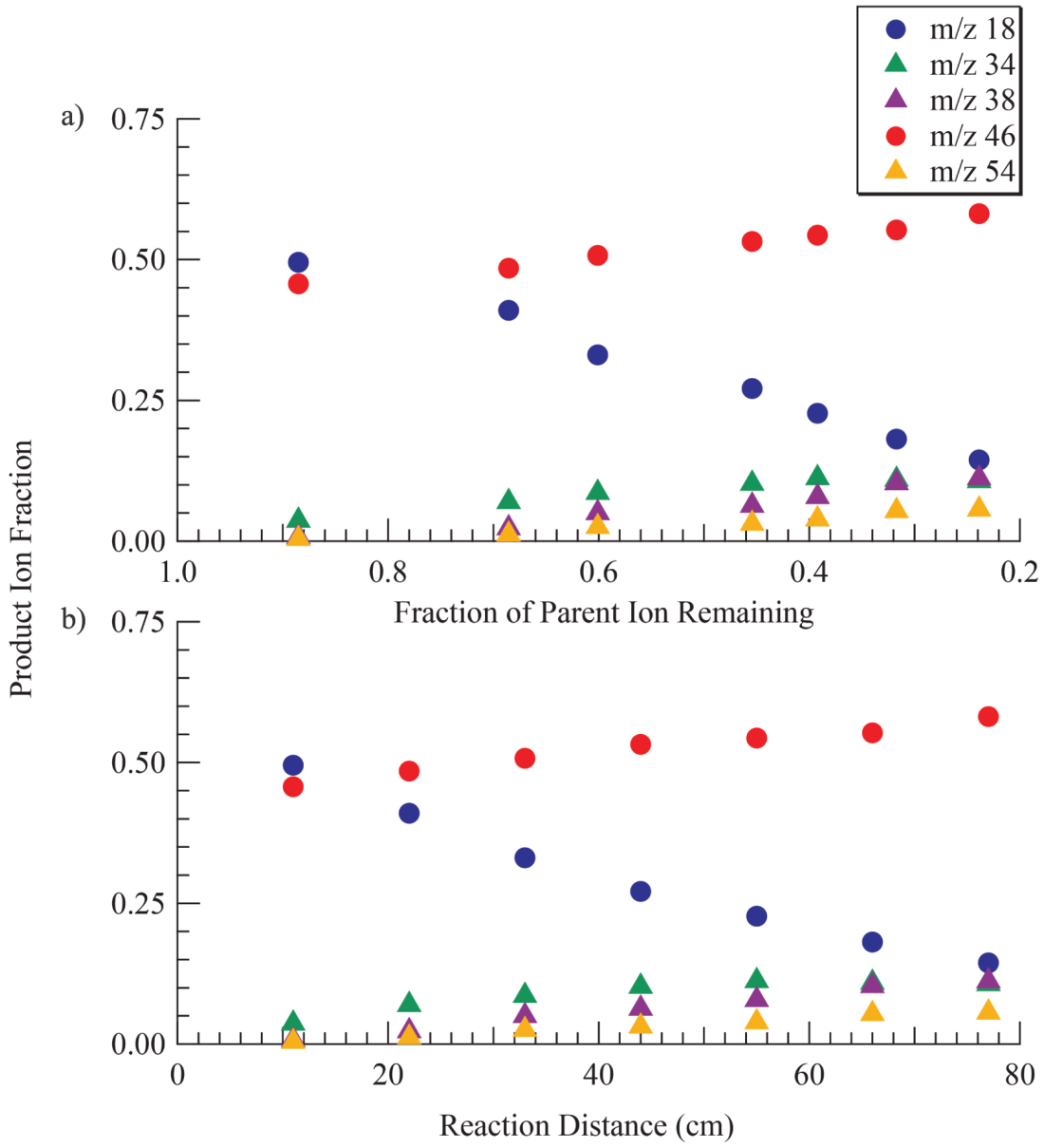

Figure 2.9: Product distributions for the ion molecule reaction $CF^+ + CD_3OD$. The ratio of the individual product ion to the total product ion intensity is plotted versus (a) fraction of parent ion remaining and (b) reaction distance. Primary product distributions are determined by extrapolating to (a) zero reaction of parent ion or (b) zero reaction distance. The ions at m/z 18 and 46 are primary products. The ions at m/z 34, 38, and 54 are secondary products.

is the dominant cooling mechanism,

$$AB^{*+} \xrightarrow{k_r} AB^+ + h\nu. \tag{2.32}$$

For PAHs, this results in emission of wavelengths in the infrared region (See Section 1.4). However, in the reaction flow tube, where the densities are high, complexes are stabilized by inelastic collisions with the buffer gas, M,

$$AB^{*+} + M \xrightarrow{k_{in}} AB^+ + M. \tag{2.33}$$

Equations 2.31–2.33 can be combined to relate the energy dissipating process in the flow tube to the processes occurring in the ISM,

$$k_{eff} = \frac{k_1\ (k_r + k_{in}[M])}{k_{-1} + k_r + k_{in}[M]}. \tag{2.34}$$

This effective bimolecular rate constant describes a situation where all four processes are taking place. For the conditions of the flow tube, $k_{-1} \gg k_r$ and $k_{-1} \gg k_{in}[M]$. Equation 2.34 simplifies to

$$k_{eff} = \frac{k_1\ (k_r + k_{in}[M])}{k_{-1}} = \frac{k_1\ k_r}{k_{-1}} + \frac{k_1\ k_{in}[M]}{k_{-1}} = k_{ra} + k_{3b}[M]; \tag{2.35}$$

where,

$$k_{ra} = \frac{k_1\ k_r}{k_{-1}} \tag{2.36}$$

is the radiative association rate constant, and

$$k_{3b} = \frac{k_1\ k_{in}}{k_{-1}} \tag{2.37}$$

is the three-body association rate constant. The radiative rate constant, k_r, for infrared emission is $\sim 10^2$–10^3 s^{-1} and the inelastic collision rate constant, k_{in}, for He at 300 K is 1–2 10^{-10} cm^3 s^{-1}. The effective bimolecular rate constant can be determined using the process described in Section 2.6.1. In the flow tube, the He densities are sufficiently high such that $k_{3b} \gg k_{ra}$. Thus, k_{3b} can be determined by measuring k_{eff} and the He density.

$$k_{3b} = \frac{k_{eff}}{[He]} \tag{2.38}$$

Equations 2.36 and 2.37 can be equated by a common factor, $\frac{k_1}{k_{-1}}$. This relationship allows for the determination of k_{ra},

$$k_{\mathrm{ra}} = \frac{k_{\mathrm{r}}\ k_{3\mathrm{b}}}{k_{\mathrm{in}}} \tag{2.39}$$

For large molecules like the PAHs included in this study, k_{eff} is constant over the range of He densities achievable in the reaction flow tube. Under saturated conditions only a lower limit of the radiative rate constant can be determined. This simple kinetic analysis allows for a first order approximation of the radiative rate constant from measured effective bimolecular rate constants in the FA-SIFT instrument [20].

2.9 Collision Rate Constant and Reaction Efficiency Determination

Reaction efficiencies, $k_{\mathrm{exp}}/k_{\mathrm{col}}$, are determined to allow comparison of different ion-neutral reactions. For nonpolar neutral molecules Langevin collision theory is used. The ion is treated as a point charge and the ion-induced dipole attraction of the neutral is considered [21]:

$$k_{\mathrm{Langevin}} = 2\pi q \left(\frac{\alpha}{\mu}\right), \tag{2.40}$$

where q is the charge of the ion, α is the polarizability of the neutral molecule, and μ is the reduced mass of the ion-molecule pair. In the case of polar neutral molecules, the parameterized trajectory theory of Su & Chesnavich [22] is used. This theory treats the ion as a point charge and the neutral molecule as a rigid rotor. The attractive potential of the permanent dipole and the ion-induced dipole are considered in this theory. Trajectory calculations were used to demonstrate that the ratio of the capture rate constant versus the Langevin rate constant depended on one parameter for most physically realistic systems. First, the capture parameter x is determined,

$$x = \frac{\mu_{\mathrm{D}}}{(2\alpha \mathrm{k_B T})^{1/2}}, \tag{2.41}$$

where μ_D is the permanent dipole moment of the neutral molecule, k_B is the Boltzmann constant, and T is the temperature. From the determination of x, a double fit line is used to calculate the capture rate constant,

$$k_{cap} = 0.4767x + 0.6200; \qquad x \geq 2 \tag{2.42}$$

$$= \frac{(x + 0.5090)^2}{10.526} + 0.9754; \qquad x \leq 2. \tag{2.43}$$

Finally, the collision rate constant is determined by multiplying k_{cap} with the Langevin collision rate constant (Equation 2.40),

$$k_{col} = k_{cap} \cdot k_{Langevin}. \tag{2.44}$$

This theory has been shown to determine collision rate constants with better than 97% accuracy [22].

For reactions of large anions with neutral species, where the charged species is highly polarizable, the point polarizable ion model is used (cf. Eichelberger et al. [23]). This model is useful for reactions of $[PAH–H]^-$ with H atom and neutral species that do not possess a permanent dipole moment. Reactions efficiencies, not rate constants, are compared to give insight into trends in reactivity.

2.10 Computational Methods

Ab initio and density functional theory calculations are used to support the experimental studies. The energies and structures for reactants, products, and intermediates involved in the reactions are calculated using *Gaussian 03* [24] and *Gaussian 09* [25]. B3LYP [26–28], MP2 [29], and CCSD(T) [30] calculations were carried out using Pople [31] and Dunning [32, 33] style basis sets, where appropriate. To provide additional insight into the reactions, potential energy surfaces are explored for several of the chemical systems.

2.11 References

1. Ferguson, E. E.; Fehsenfeld, F. C.; Schmeltekopf, A. L., Flowing Afterglow Measurements of Ion-Neutral Reactions. *Adv. At. Mol. Phys.* **1969**, *5*, 1.

2. Adams, N. G.; Smith, D., The Selected Ion Flow Tube (SIFT); A Technique For Studying Ion-Neutral Reactions. *Int. J. Mass Spectrom. Ion Phys.* **1976**, *21*, 349.

3. Grabowski, J. J. Studies of Gas Phase Ion-Molecule Reactions Using a Selected Ion Flow Tube. Ph.D. Thesis, University of Colorado, Boulder, 1983.

4. Van Doren, J. M.; Barlow, S. E.; DePuy, C. H.; Bierbaum, V. M., The Tandem Flowing Afterglow-SIFT-Drift. *Int. J. Mass Spectrom. Ion Process.* **1987**, *81*, 85.

5. Van Doren, J. M. The Tandem Flowing Afterglow-SIFT-Drift: Developments and Applications to Gas Phase Ion Chemistry. Ph.D. Thesis, University of Colorado, Boulder, 1987.

6. Bierbaum, V. M., Flow Tubes. In *Encyclopedia of Mass Spectrometry*, Armentrout, P. B., Ed.; Elsevier: Amsterdam, 2003; p 940.

7. Shea, R. C.; Petzold, C. J.; Campbell, J. L.; Li, S.; Aaserud, D. J.; Kenttämaa, H. I., Characterization of Laser-Induced Acoustic Desorption Coupled with a Fourier Transform Ion Cyclotron Resonance Mass Spectrometer. *Anal. Chem.* **2006**, *78*, 6133.

8. Zinovev, A. V.; Veryovkin, I. V.; Moore, J. F.; Pellin, M. J., Laser-Driven Acoustic Desorption of Organic Molecules from Back-Irradiated Solid Foils. *Anal. Chem.* **2007**, *79*, 8232.

9. Bald, I.; Dabkowska, I.; Illenberger, E., Probing Biomolecules by Laser-Induced Acoustic Desorption: Electrons at Near Zero Electron Volts Trigger Sugar-Phosphate Cleavage. *Angew. Chem. Int. Ed.* **2008**, *47*, 8518.

10. Nyadong, L.; Quinn, J. P.; Hsu, C. S.; Hendrickson, C. L.; Rodgers, R. P.; Marshall, A. G., Atmospheric Pressure Laser-Induced Acoustic Desorption Chemical Ionization Mass Spectrometry for Analysis of Saturated Hydrocarbons. *Anal. Chem.* **2012**, *84*, 7131.

11. Shea, R. C.; Petzold, C. J.; Liu, J.-a.; Kenttämaa, H. I., Experimental Investigations of the Internal Energy of Molecules Evaporated via Laser-Induced Acoustic Desorption into a Fourier Transform Ion Cyclotron Resonance Mass Spectrometer. *Anal. Chem.* **2007**, *79*, 1825.

12. Shea, R. C.; Habicht, S. C.; Vaughn, W. E.; Kenttämaa, H. I., Design and Characterization of a High-Power Laser-Induced Acoustic Desorption Probe Coupled with a Fourier Transform Ion Cyclotron Resonance Mass Spectrometer. *Anal. Chem.* **2007**, *79*, 2688.

13. Diebold, G. J.; Rivas, I. V.; Shafeizad, S.; McFadden, D. L., Detection of Several Electronically Metastable Atomic States by Gas Phase EPR. *Chem. Phys.* **1980**, *52*, 453.

14. Anderson, D. R.; Bierbaum, V. M.; DePuy, C. H.; Grabowski, J. J., Flowing Afterglow Studies of Organic Positive Ions Generated by Penning Ionization Using Metastable Argon Atoms. *Int. J. Mass Spectrom. Ion Phys.* **1983**, *52*, 65.

15. Trainor, D. W.; Ham, D. O.; Kaufman, F., Gas Phase Recombination of Hydrogen and Deuterium Atoms. *J. Chem. Phys.* **1973**, *58*, 4599.

16. Le Page, V.; Keheyan, Y.; Snow, T. P.; Bierbaum, V. M., Reactions of Cations Derived from Naphthalene with Molecules and Atoms of Interstellar Interest. *J. Am. Chem. Soc.* **1999**, *121*, 9435.

17. Howard, C. J.; Fehsenfeld, F. C.; McFarland, M., Negative Ion-Molecule Reactions with Atomic Hydrogen in the Gas Phase at 296 K. *J. Chem. Phys.* **1974**, *60*, 5086.

18. Mankelevich, Y. A.; Ashfold, M. N. R.; Umemoto, H., Molecular Dissociation and Vibrational Excitation on a Metal Hot Filament Surface. *J. Phys. D.* **2014**, *47*, 025503.

19. Scott, G. B. I.; Fairley, D. A.; Freeman, C. G.; McEwan, M. J.; Adams, N. G.; Babcock, L. M., $C_mH_n^+$ Reactions with H and H_2: An Experimental Study. *J. Phys. Chem. A* **1997**, *101*, 4973.

20. Herbst, E.; Smith, D.; Adams, N. G.; McIntosh, B. J., Association Reactions. Theoretical Shortcomings. *J. Chem. Soc., Faraday Trans. 2* **1989**, *85*, 1655.

21. Gioumousis, G.; Stevenson, D. P., Reactions of Gaseous Molecule Ions with Gaseous Molecules. V. Theory. *J. Chem. Phys.* **1958**, *29*, 294.

22. Su, T.; Chesnavich, W. J., Parametrization of the Ion-Polar Molecule Collision Rate Constant by Trajectory Calculations. *J. Chem. Phys.* **1982**, *76*, 5183.

23. Eichelberger, B. R.; Snow, T. P.; Bierbaum, V. M., Collision Rate Constants for Polarizable Ions. *J. Am. Soc. Mass. Spectrom.* **2003**, *14*, 501.

24. Frisch, M. J.; Trucks, G. W.; Schlegel, H. B.; Scuseria, G. E.; Robb, M. A.; Cheeseman, J. R.; Scalmani, G.; Barone, V.; Mennucci, B.; Petersson, G. A. et al. *Gaussian 03*, Revision E.01; Gaussian Inc.: Wallingford, CT, 2003.

25. Frisch, M. J.; Trucks, G. W.; Schlegel, H. B.; Scuseria, G. E.; Robb, M. A.; Cheeseman, J. R.; Scalmani, G.; Barone, V.; Mennucci, B.; Petersson, G. A. et al. *Gaussian 09*, Revision D.01; Gaussian Inc.: Wallingford, CT, 2009.

26. Becke, A. D., Density-Functional Thermochemistry. III. The Role of Exact Exchange. *J. Chem. Phys.* **1993**, *98*, 5648.

27. Lee, C.; Yang, W.; Parr, R. G., Development of the Colle-Salvetti Correlation-Energy Formula into a Functional of the Electron Density. *Phys. Rev. B* **1988**, *37*, 785.

28. Kendall, R. A.; Dunning, T. H., Jr.; Harrison, R. J., Electron Affinities of the First-Row Atoms Revisited. Systematic Basis Sets and Wave Functions. *J. Chem. Phys.* **1992**, *96*, 6796.

29. Møller, C.; Plesset, M. S., Note on an Approximation Treatment for Many-Electron Systems. *Phys. Rev.* **1934**, *46*, 618.

30. Bartlett, R. J.; Musiał, M., Coupled-Cluster Theory in Quantum Chemistry. *Rev. Modern Phys.* **2007**, *79*, 291.

31. Ditchfield, R.; Hehre, W. J.; Pople, J. A., Self-Consistent Molecular-Orbital Methods. IX. An Extended Gaussian-Type Basis for Molecular-Orbital Studies of Organic Molecules. *J. Chem. Phys.* **1971**, *54*, 724.

32. Dunning, T. H., Jr., Gaussian Basis Sets for Use in Correlated Molecular Calculations. I. The Atoms Boron Through Neon and Hydrogen. *J. Chem. Phys.* **1989**, *90*, 1007.

33. Dunning, T. H., Jr.; Peterson, K. A.; Wilson, A. K., Gaussian Basis Sets for Use in Correlated Molecular Calculations. X. The Atoms Aluminum Through Argon Revisited. *J. Chem. Phys.* **2001**, *114*, 9244.

Chapter 3

Gas-Phase Reactions of Polycyclic Aromatic Hydrocarbon Cations and their Nitrogen-Containing Analogs with H Atoms

3.1 Introduction

Polycyclic aromatic hydrocarbon (PAH) cations have long been proposed as possible carriers of the diffuse interstellar absorption bands [1–3] and the unidentified infrared emission bands (UIRs; [4–6]). The UIR bands are ubiquitous throughout the interstellar medium (ISM) [7], vary with different environmental conditions [8, 9], and show features characteristic of aromatic species [10]. Although the mid-IR spectra will most likely not lead to the identification of individual PAHs, the generation of the NASA Ames PAH IR spectral database [10] has aided in identifying classes of PAHs. Included in this list are PAH cations and polycyclic aromatic nitrogen heterocycles (PANHs) [12, 13]. Given that PAH cations contribute to the IR emission spectra, it is expected that PANH cations exist in these regions as well [14]. The origin of PAHs in the universe is still not completely understood; however, it has been likened to the PAH formation in the incomplete combustion of flames [15]. Several computational studies have revealed gas-phase mechanisms for incorporating nitrogen into an aromatic ring system [16–18]. PA(N)H cations likely exist in the highest abundance in the diffuse regions of the ISM due to the high photon flux [19]. Here, atomic hydrogen dominates the chemical landscape and the hydrogenation and charge state of the molecules is determined by the size of the PA(N)H, radiation flux, and PA(N)H chemistry [20]. Alternatively, neutral PAHs and H_2 are dominant in denser regions of the ISM. The

study by Le Page et al. [21] of the charge and hydrogenation state of PAHs in the diffuse medium concluded that PAHs with fewer than 30 carbon atoms are either destroyed or severely dehydrogenated; in contrast, large PAHs (greater than 30 carbon atoms) display normal hydrogenation in competition with the protonated form. Here, we have extended the studies previously carried out in our laboratory to include reactions of H atoms with additional PAH cations as well as with PANH cations. The structures of the species investigated are shown in Figure 3.1.

3.2 Methods

Reactions of PA(N)H cations with H atom and neutral molecules are investigated using a flowing afterglow-selected ion flow tube (FA-SIFT). Rate constants are measured under pseudo first-order conditions. Density functional theory calculations are carried out to support the experimental results.

3.2.1 Experimental Methods

The experiments are carried out at 298 K using an FA-SIFT instrument (Figure 2.1). Here, PA(N)H neutral molecules that are sufficiently volatile are introduced into the gas phase by evaporation of the liquid or solid species at room temperature or with gentle heating when needed. The introduction of tetracene into the gas phase is achieved using the laser induced acoustic desorption (LIAD) technique, described in Section 2.3. The parent cations of naphthalene, quinoline, and isoquinoline were generated by Penning ionization utilizing excited state Ar [22, 23]. While Penning ionization is a gentle technique, it is difficult to generate high densities of electronically excited Ar. Parent cation formation is made even more difficult due to the low vapor pressure of the neutral species and the long distance the ions must travel before they enter the ion selection region. PA(N)H cations were also generated using He^+ produced using electron ionization [24]. The results for napthalene, quinoline, and isoquinoline were compared for both ionization methods and no

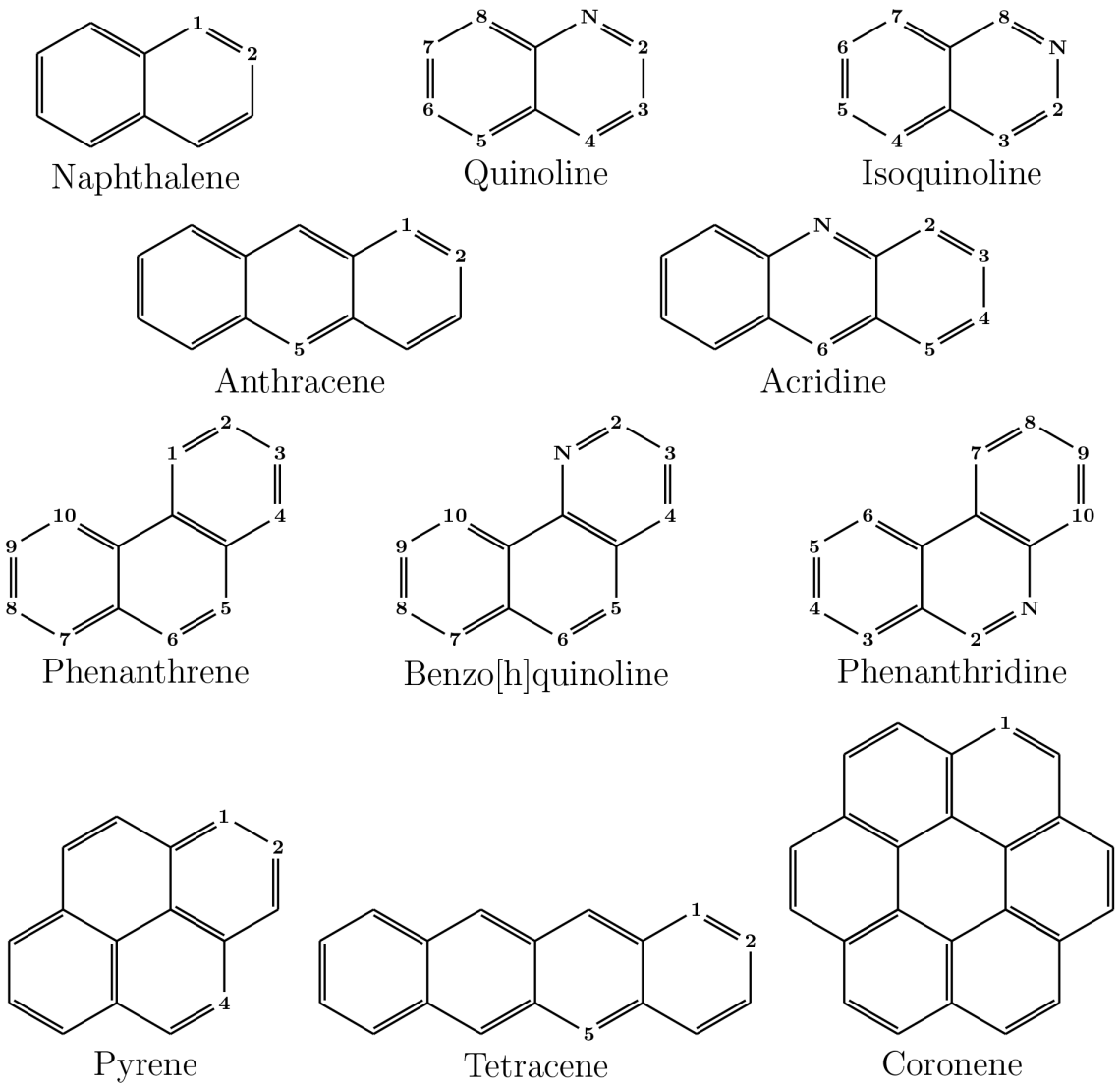

Figure 3.1: Names, structures, and numbering of the distinct positions of the PA(N)Hs included in this study.

differences were found in the rate constants or product distributions. The reactant ions are then sampled, mass-selected using a quadrupole mass filter, injected into the reaction flow tube, and collisionally cooled by a helium carrier gas (0.30–0.45 Torr) prior to addition of neutral reactants. Atomic hydrogen is introduced into the reaction flow tube at a fixed reaction distance (Section 2.5). Hydrogen atoms are generated by thermal dissociation of H_2 gas on a hot tungsten filament. The reactant ion signal is monitored as a function of filament voltage using a quadrupole mass filter coupled to an electron multiplier. The filament voltage is directly proportional to the concentration of atomic hydrogen, which is determined using the calibration reaction:

$$C_6H_6^+ + H \longrightarrow C_6H_7^+ \tag{3.1}$$

$$\longrightarrow C_6H_5^+ + H_2, \tag{3.2}$$

with a known reaction rate constant of $k = 2.2 \times 10^{-10}$ cm^3 s^{-1} [25]. Alternatively, measured concentrations of stable neutral reactant molecules are added to the reaction flow tube through a manifold of inlets. The reactant ion signal and kinetics are monitored as a function of reaction distance. Rate constants or upper limits in reactivity are derived using pseudo first order kinetics [26].

Tetracene cations were generated by introducing neutral tetracene into the reaction flow tube utilizing the LIAD technique with subsequent ionization from He^+. In this work, 0.05 mg of solid tetracene was desolved in benzene. A fixed-flow airbrush (Badger 200nh) was used to apply the solution to a thin titanium foil (12.7μm, Alfa Aesar), 3.1 cm in diameter. After the tetracene solution was applied to the foil, it was mounted on a probe where it was held in place between two stainless steel rings. The probe is inserted into the ion production flow tube so that the foil was held in the center and desorption was perpendicular to the He flow (Figure 2.1). An unfocused, pulsed laser beam (Continuum Minilite II, Nd:YAG, 532 nm, 3 mm beam diameter, 15 Hz, 25 mJ pulse^{-1}) is directed through an optically thin window into the ion production region toward the metal foil. The laser light impinges on the

uncoated side of the foil, desorbing the intact, neutral tetracene into the gas phase [27]. The laser beam is scanned to produce a continuous source of neutral analyte using a motorized mirror mount (Thorlabs KS1-Z8). A scan rate of 0.04 mm s^{-1} was found to give sufficient ion intensity while allowing maximum experimental time per foil. This scan rate results in a desorption area of $\sim 8 \times 10^{-3}$ mm^2 per shot and an experiment duration of 45 minutes per foil. Ion intensities are directly correlated with laser power, which is consistent with previous work [27, 28].

The neutral reagents included in this study are as follows: hydrogen (H_2; 99.999% with the gas further purified by passage through a molecular sieve trap immersed in liquid nitrogen), carbon monoxide (CO; 99.5%), ammonia, (NH_3; 99.9995%), water (H_2O; HPLC grade), carbon dioxide (CO_2; $\geq$ 99%), naphthalene ($C_{10}H_8$; 97%), quinoline (C_9H_7N; 98%), isoquinoline (C_9H_7N; 97%), anthracene ($C_{14}H_{10}$; 97%), acridine ($C_{13}H_9N$; 97%), phenanthrene ($C_{14}H_{10}$; 97%), benzo[h]quinoline ($C_{13}H_9N$; 97%), phenanthridine ($C_{13}H_9N$; 97%), and tetracene ($C_{18}H_{12}$; 98%).

3.2.2 Computational Methods

We have carried out density functional theory calculations to support experimental studies. We computed structures, geometries, and energies for reactants, intermediates, and products involved in the reactions using *Gaussian 09* [29] at the B3LYP/6-311G(*d,p*) level of theory [30, 31]. This method and basis set have been shown to accurately determine energies of PAHs [32]. Similar to the work of Holm et al. [32], we have found only small differences ($<$ 0.5 kcal mol^{-1}) in the computed reaction energies when comparing the basis sets 6-311G(*d,p*) and 6-311++G(*2d,p*). Therefore, reaction enthalpies are determined at 298 K using theoretically calculated geometries and energies with the 6-311G(*d,p*) basis set.

Table 3.1: PA(N)H cation/H atom association reactions

Ionic Reactant	k_{exp}[a] (10^{-10} cm^3 s^{-1})	Efficiency[b]	ΔH_{exp}[c] (kcal mol^{-1})	Association at N ΔH_{theor}[d] (kcal mol^{-1})	Association at C ΔH_{theor}[d,e] (kcal mol^{-1})
Naphthalene$^+$	1.9[f]	0.10	66.1	—	64.5
Quinoline$^+$	1.9	0.10	113.2	109.7	72.0
Isoquinoline$^+$	1.8	0.095	110.6	108.4	67.0
Anthracene$^+$	1.3	0.068	67.7	—	63.2
Acridine$^+$	1.4	0.074	98.8	97.2	61.9
Phenanthrene$^+$	1.7	0.090	65.7	—	61.6
Benzo[h]quinoline$^+$	1.7	0.090	—	96.7	65.1
Phenanthridine$^+$	1.7	0.090	—	104.6	68.6
Pyrene$^+$	1.4[g]	0.074	65.4	—	62.8
Tetracene$^+$	1.3	0.068	63.6	—	59.9
Coronene$^+$	1.4[h]	0.074	60.4	—	57.8

Notes. No measurable rate constants were obtained for reactions with H_2, CO, NH_3, H_2O, and CO_2 and we report a conservative upper limit for the rate constants of $k \leq 1 \times 10^{-12}$ cm^3 s^{-1}.

[a] Rate coefficients are measured at 0.30–0.45 Torr helium. The experimental precision, reported as 1σ of the mean, is $\pm 10\%$ and the total error is estimated to be $\pm 50\%$.

[b] The reaction efficiency is reported as k_{exp}/k_{col}. The collisional rate constant, k_{col}, is determined by Langevin theory [33] and gives a value of 1.9×10^{-9} cm^3 s^{-1} for all reactions of PA(N)H$^+$ with H atom.

[c] Values determined using Hess's law with experimental values for ionization energies, bond energies, proton affinities, and heats of formation taken from [34, 35]. The values correspond to association at C for PAH cations and to association at N for PANH cations.

[d] B3LYP/6-311G(d,p) theory level including zero-point energy correction and thermal energy correction at 298 K.

[e] Reported values are calculated for association at the carbon atom yielding the greatest exothermicity (See Appendix A).

[f] Le Page et al. [36]

[g] Le Page et al. [24]

[h] Betts et al. [37]

3.3 Results and Discussion

The reactions of PA(N)H cations with H atom are summarized in Table 3.1; values include effective two-body reaction rate constants, collision rate constants, reaction efficiencies, and enthalpies of reaction. The experimental precision, reported as 1σ of the mean, is $\pm 10\%$ for all reactions and the total error is estimated to be $\pm 50\%$. We report reaction efficiencies as $k_{\mathrm{exp}}/k_{\mathrm{col}}$, where k_{col} is the collision rate constant determined by Langevin theory [33]. Experimental enthalpies of reaction, ΔH_{exp}, are determined using Hess's law with ionization energies, bond energies, proton affinities, and heats of formation taken from the NIST Chemistry WebBook [34] and from the 89th edition of the CRC Handbook of Chemistry and Physics [35]. In addition, we determine enthalpies of reaction at 298 K using density functional theory calculations. No measurable rate constants were obtained for reactions with H_2, CO, NH_3, H_2O, and CO_2. Therefore, we report a conservative upper limit for the rate constants of $k \leq 1 \times 10^{-12}$ cm^3 s^{-1}. All reactions with H atom proceed through association via a third body; however, in the ISM, radiative stabilization will likely preserve these association species. The reaction conditions of the experimental apparatus are not representative of interstellar temperatures and pressures [3]; however, this systematic study combined with previous findings [24, 36, 37] gives valuable insight into the reactivity of PAH and PANH cations. Our measured effective two-body rate constants can be used to compute a lower limit to the radiative association rate constant [38]. Although all reactions proceed via the same mechanism, two trends can be seen: (1) there are subtle differences in reactivity for PA(N)H cations of different size and geometry, and (2) there is no measurable difference in reactivity between PAH and PANH cations with H atom.

3.3.1 Size and Geometry Dependence

The reactions of PA(N)H cations with H atom all proceed through association to form a hydrogenated cationic species. The association complex is stabilized in the FA-SIFT

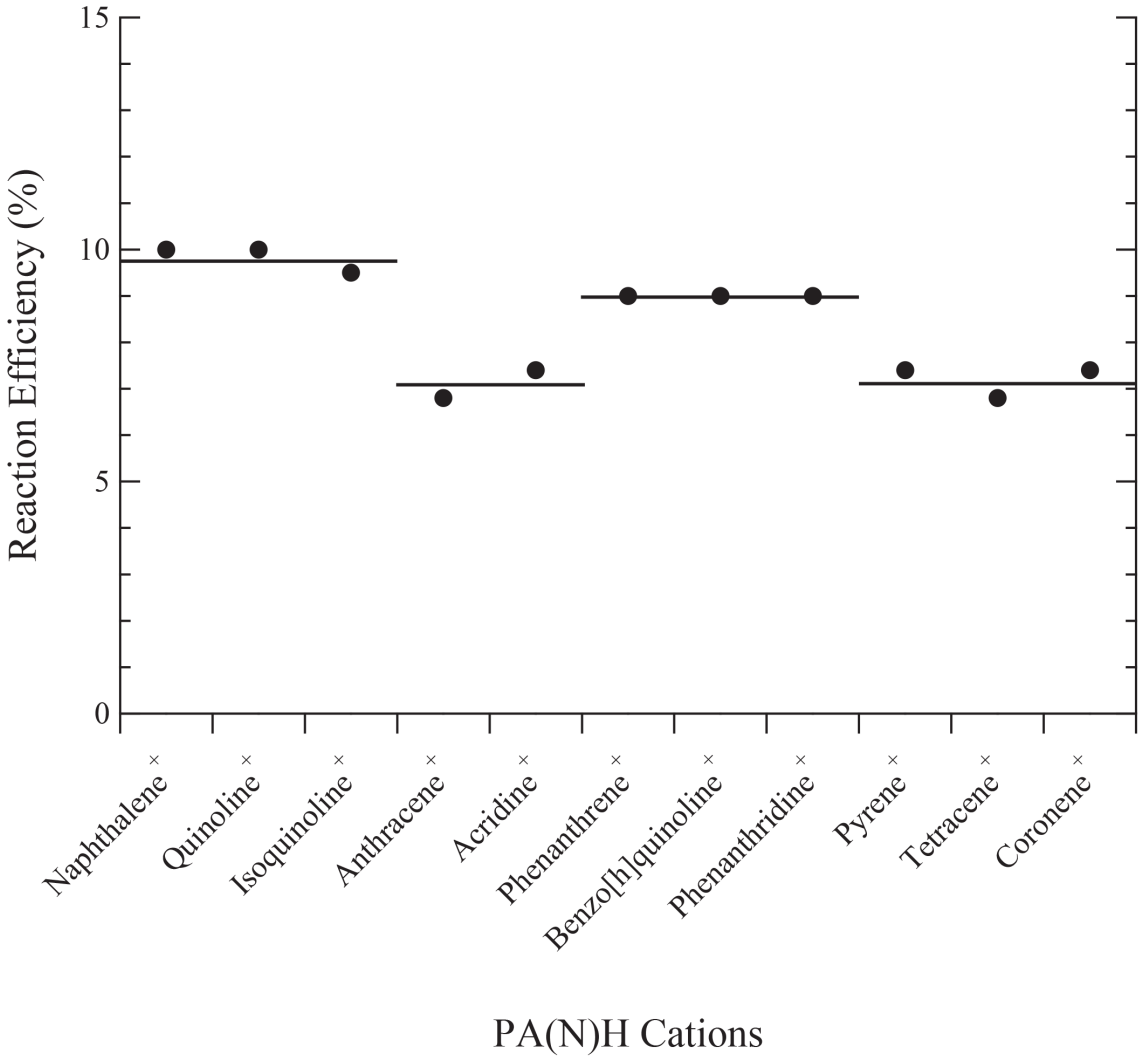

Figure 3.2: A plot of the reaction efficiency for the reaction of PA(N)H cations with H atom. The solid horizontal lines have been added to indicate that the encompassed data points are equivalent within experimental precision. Reaction efficiencies are reported as $k_{\text{exp}}/k_{\text{col}}$, where k_{col} is the collision rate constant determined by Langevin theory [33]. Rate constants for naphthalene, pyrene and coronene are taken from Le Page et al. [36], Le Page et al. [24], and Betts et al. [37], respectively.

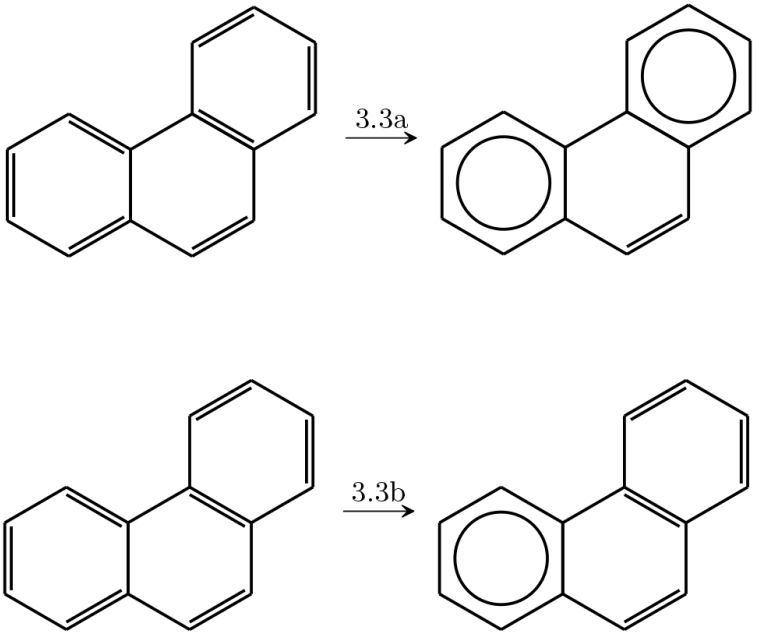

Figure 3.3: Two different Kekulé (left) and Clar (right) representations of phenanthrene. Clar's rule has been applied to the Kekulé structures to produce the Clar structures. In this representation, three double bonds in one ring are replaced by a circle. According to Clar's rule, the formula that best represents the molecule contains the greatest number of rings (3.3a) [42].

experiments by the He buffer gas. In the ISM, the density is too low for this to occur, and radiative association is the most likely mechanism for stabilizing the complex. Herbst & Le Page [39] have shown that a PAH as small as naphthalene has enough degrees of freedom to stabilize the association complex through radiative emission. In addition, the computed effective two-body rate constant remained constant over large temperature (50–300 K) and density (10^4–10^{16} cm^{-3}) ranges. This phenomenon should be enhanced for the larger PA(N)Hs that are proposed to exist in the ISM due to the increased number of degrees of freedom. In addition, association reactions for [PAH-H]$^+$ + H_2 have been observed in low pressure ion cyclotron resonance experiments for the reactions of

$$C_6H_5^+ + H_2 \longrightarrow C_6H_7^+ \qquad \text{[40], and} \tag{3.3}$$

$$C_{10}H_7^+ + H_2 \longrightarrow C_{10}H_9^+ \qquad \text{[36, 41].} \tag{3.4}$$

When comparing the PA(N)H cations included in this study, the reactivity of these species decreases with increasing size and quickly reaches an asymptotic value. This can be seen in Figure 3.2 when comparing the linear structures. The reaction efficiency reaches a constant value of ∼7%. The solid horizontal lines have been added to indicate that the encompassed data points are equivalent within experimental precision.

It is also evident that the angular structure of phenanthrene, benzo[h]quinoline, and phenanthridine enhances their reactivity with H atom compared to the linear structures of anthracene and acridine. This may be explained by applying Clar's rule to the Kekulé structures; in this representation, three double bonds in one ring (a sextet) are replaced by a circle [42]. According to Clar's rule, the formula that best represents the molecule contains the greatest number of sextets (rings). In the case of phenanthrene, two different formulas can be drawn (Figure 3.3). Figure 3.3a is the best representative picture, with a ring at each end of the molecule and a fixed double bond in the center. This fixed double bond at the 5, 6 position reacts more like an olefin than an aromatic species in the neutral molecule, which may relate to the slight increase in reactivity in the parent cation [42]. However, this

enhanced reactivity is relatively small (9% versus 7%).

3.3.2 PAH versus PANH Cations

The reactivities of PAH and PANH cations with H atom are equivalent within experimental precision, when comparing PA(N)H cations of the same size and geometry (Figure 3.2). The exothermicities of the reaction for association at the nitrogen atom and at the carbon atom yielding the greatest exothermicity are listed in Table 3.1. For a complete list of calculated exothermicities see Appendix A. It has been suggested that the H atom associates at the most exothermic site for the reaction of PAH cations with H atom [43]. Although association at the nitrogen is almost twice as exothermic, the reactivity toward H atom is identical for PAH and PANH cations. We have explored the reaction coordinate for the interaction of quinoline cation with H atom and were unable to find any barriers for association of H atom at any site. However, there are barriers above the energy of the reactants for the transfer of the H atom between different sites. In addition, the triplet state association product of all PA(N)H^+ cations with H atom is above the energy of the reactants. The theoretical calculations of Dryza et al. [44] indicate that the lowest energy structure of the quinoline and isoquinoline cation has an electron removed from the pi system and not the lone pair on the nitrogen atom. This electron configuration will likely result in similar mechanisms for the reaction of PAH cations and PANH cations with H atom, when comparing PA(N)H cations of the same size.

Given the lack of difference in reactivity, we suggest that the reactions of large PAH and PANH cations with H atom may be approximated by a single effective two-body rate constant, $k = 1 \times 10^{-10}$ cm^3 s^{-1}, which gives a lower limit to the radiative association rate constant of $k > 7 \times 10^{-14}$ cm^3 s^{-1} [38].

3.4 Conclusion

We have continued the study of PAH cations previously carried out by our laboratory and extended the study to include nitrogen heterocycles. The LIAD technique was successfully adapted to an FA-SIFT to access large, non-volatile organic species. The LIAD technique can be used to study much larger PA(N)H ions and other non-volatile organic species; however, the pulsed nature of this technique coupled to the FA-SIFT makes studies of large species nontrivial. In addition, the results from this study indicate that a complete study of all possible PAH configurations may not be necessary. Several conclusions are derived from this study:

1. PA(N)H cations are unreactive with H_2, CO, NH_3, H_2O, and CO_2 within our measurement capabilities. We place a conservative upper limit of $k \leq 1 \times 10^{-12}$ cm^3 s^{-1} on these processes.

2. PA(N)H cations show a slight difference in reactivity toward H atom for molecules of the same formula, but different geometries.

3. Reactions of H atom with PAH and PANH cations with the same structure and geometry exhibit no measurable difference in reaction efficiency.

4. The reaction efficiency of PA(N)H cations with H atom decreases slightly as the size of the cation increases but reaches a constant value of $\sim$7%.

5. The chemistry of PAH cations with H atoms is important in diffuse regions of the ISM, where ionized PAHs and H atoms are abundant [19]; however, neutral PAHs are more abundant in dark clouds where H_2 is dominant. This is consistent with observations [45].

The modeled rate coefficient for the reaction of PAH cations with H atom used by Le Page et al. [20] works well for small PAHs (<16 carbon atoms); however, it is evident from our results that larger PAHs deviate from this equation. For example, using the model suggested by Le Page et al. [20], the rate constants for anthracene, tetracene, and coronene should be smaller. In addition, there should be no difference in reactivity between anthracene

and phenanthrene. Because it is likely that PA(N)H cations with 30–50 carbon atoms will have normal hydrogen coverage in the diffuse ISM, we suggest that a single rate constant is sufficient to describe the reactions of PA(N)H cations with H atom.

3.5 References

1. Sarre, P. J., The Diffuse Interstellar Bands: A Major Problem in Astronomical Spectroscopy. *J. Mol. Spectrosc.* **2006**, *238*, 1.

2. Pathak, A.; Sarre, P. J., Protonated PAHs as Carriers of Diffuse Interstellar Bands. *Mon. Not. R. Astron. Soc. Lett.* **2008**, *391*, L10.

3. Snow, T. P.; Bierbaum, V. M., Ion Chemistry in the Interstellar Medium. *Annu. Rev. Anal. Chem.* **2008**, *1*, 229.

4. Léger, A.; Puget, J. L., Identification of the Unidentified IR Emission Features of Interstellar Dust? *Astron. Astrophys.* **1984**, *137*, L5.

5. Allamandola, L. J.; Tielens, A. G. G. M.; Barker, J. R., Polycyclic Aromatic Hydrocarbons and the Unidentified Infrared Emission Bands: Auto Exhaust Along the Milky Way! *Astrophys. J.* **1985**, *290*, L25.

6. Allamandola, L. J.; Hudgins, D. M.; Sandford, S. A., Modeling the Unidentified Infrared Emission with Combinations of Polycyclic Aromatic Hydrocarbons. *Astrophys. J. Lett.* **1999**, *511*, L115.

7. Snow, T. P.; McCall, B. J., Diffuse Atomic and Molecular Clouds. *Annu. Rev. Astron. Astrophys.* **2006**, *44*, 367.

8. Peeters, E.; Hony, S.; Kerckhoven, C. V.; Tielens, A. G. G. M.; Allamandola, L. J.; Hudgins, D. M.; Bauschlicher, C. W., The Rich 6 to 9 μm Spectrum of Interstellar PAHs. *Astron. Astrophys.* **2002**, *390*, 1089.

9. van Diedenhoven, B.; Peeters, E.; Kerckhoven, C. V.; Hony, S.; Hudgins, D. M.; Allamandola, L. J.; Tielens, A. G. G. M., The Profiles of the 3-12 Micron Polycyclic Aromatic Hydrocarbon Features. *Astrophys. J.* **2004**, *611*, 928.

10. Li, A.; Draine, B. T., The Carriers of the Interstellar Unidentified Infrared Emission Features: Aromatic or Aliphatic? *Astrophys. J. Lett.* **2012**, *760*, L35.

11. Bauschlicher, C. W., Jr.; Boersma, C.; Ricca, A.; Mattioda, A. L.; Cami, J.; Peeters, E.; Sánchez de Armas, F.; Puerta Saborido, G.; Hudgins, D. M.; Allamandola, L. J., The NASA Ames Polycyclic Aromatic Hydrocarbon Infrared Spectroscopic Database: The Computed Spectra. *Astrophys. J. Supp. Ser.* **2010**, *189*, 341.

12. Cami, J., Analyzing Astronomical Observations with the NASA Ames PAH Database. Hammonds, M.; Pathak, A.; Candian, A.; Sarre, P. J., Spectroscopy of Protonated and Deprotonated PAHs. *EAS Pub. Ser.* **2011**, *46*, 117.

13. Hudgins, D. M.; Bauschlicher, C. W., Jr.; Allamandola, L. J., Variations in the Peak Position of the 6.2 μm Interstellar Emission Feature: A Tracer of N in the Interstellar Polycyclic Aromatic Hydrocarbon Population. *Astrophys. J.* **2005**, *632*, 316.

14. Mattioda, A. L.; Rutter, L.; Parkhill, J.; Head-Gordon, M.; Lee, T. J.; Allamandola, L. J., Near-Infrared Spectroscopy of Nitrogenated Polycyclic Aromatic Hydrocarbon Cations from 0.7 to 2.5 μm. *Astrophys. J.* **2008**, *680*, 1243.

15. Cherchneff, I.; Barker, J. R.; Tielens, A. G. G. M., Polycyclic Aromatic Hydrocarbon Formation in Carbon-Rich Stellar Envelopes. *Astrophys. J.* **1992**, *401*, 269.

16. Ricca, A.; Bauschlicher, C. W., Jr.; Rosi, M., Mechanisms for the Incorporation of a Nitrogen Atom into Polycyclic Aromatic Hydrocarbon Cations. *Chem. Phys. Lett.* **2001**, *347*, 473.

17. Landera, A.; Mebel, A. M., Mechanisms of Formation of Nitrogen-Containing Polycyclic Aromatic Compounds in Low-Temperature Environments of Planetary Atmospheres: A Theoretical Study. *Faraday Discuss.* **2010**, *147*, 479.

18. Soliman, A.-R.; Hamid, A. M.; Attah, I.; Momoh, P.; El-Shall, M. S., Formation of Nitrogen-Containing Polycyclic Cations by Gas-Phase and Intracluster Reactions of Acetylene with the Pyridinium and Pyrimidinium Ions. *J. Am. Chem. Soc.* **2012**, *135*, 155.

19. Ruiterkamp, R.; Cox, N. L. J.; Spaans, M.; Kaper, L.; Foing, B. H.; Salama, F.; Ehrenfreund, P., PAH Charge State Distribution and DIB Carriers: Implications from the Line of Sight Toward HD 147889. *Astron. Astrophys.* **2005**, *432*, 515.

20. Le Page, V.; Snow, T. P.; Bierbaum, V. M., Hydrogenation and Charge States of PAHs in Diffuse Clouds. I. Development of a Model. *Astrophys. J. Supp. Ser.* **2001**, *132*, 233.

21. Le Page, V.; Snow, T. P.; Bierbaum, V. M., Hydrogenation and Charge States of Polycyclic Aromatic Hydrocarbons in Diffuse Clouds. II. Results. *Astrophys. J.* **2003**, *584*, 316.

22. Diebold, G. J.; Rivas, I. V.; Shafeizad, S.; McFadden, D. L., Detection of Several Electronically Metastable Atomic States by Gas Phase EPR. *Chem. Phys.* **1980**, *52*, 453.

23. Anderson, D. R.; Bierbaum, V. M.; DePuy, C. H.; Grabowski, J. J., Flowing Afterglow Studies of Organic Positive Ions Generated by Penning Ionization using Metastable Argon Atoms. *Int. J. Mass Spectrom. Ion Phys.* **1983**, *52*, 65.

24. Le Page, V.; Keheyan, Y.; Snow, T. P.; Bierbaum, V. M., Gas Phase Chemistry of Pyrene and Related Cations with Molecules and Atoms of Interstellar Interest. *Int. J. Mass Spectrom.* **1999**, *185–187*, 949.

25. Scott, G. B. I.; Fairley, D. A.; Freeman, C. G.; McEwan, M. J.; Adams, N. G.; Babcock, L. M., $C_mH_n^+$ Reactions with H and H_2: An Experimental Study. *J. Phys. Chem. A* **1997**, *101*, 4973.

26. Bierbaum, V. M., Flow Tubes. In *Encyclopedia of Mass Spectrometry*, Armentrout, P. B., Ed.; Elsevier: Amsterdam, 2003; p 940.

27. Shea, R. C.; Habicht, S. C.; Vaughn, W. E.; Kenttämaa, H. I., Design and Characterization of a High-Power Laser-Induced Acoustic Desorption Probe Coupled with a Fourier Transform Ion Cyclotron Resonance Mass Spectrometer. *Anal. Chem.* **2007**, *79*, 2688.

28. Zinovev, A. V.; Veryovkin, I. V.; Moore, J. F.; Pellin, M. J., Laser-Driven Acoustic Desorption of Organic Molecules from Back-Irradiated Solid Foils. *Anal. Chem.* **2007**, *79*, 8232.

29. Frisch, M. J.; Trucks, G. W.; Schlegel, H. B.; Scuseria, G. E.; Robb, M. A.; Cheeseman, J. R.; Scalmani, G.; Barone, V.; Mennucci, B.; Petersson, G. A. et al. *Gaussian 09*, Revision D.01; Gaussian Inc.: Wallingford, CT, 2009.

30. Becke, A. D., Density-Functional Thermochemistry. III. The Role of Exact Exchange. *J. Chem. Phys.* **1993**, *98*, 5648.

31. Lee, C.; Yang, W.; Parr, R. G., Development of the Colle-Salvetti Correlation-Energy Formula into a Functional of the Electron Density. *Phys. Rev. B* **1988**, *37*, 785.

32. Holm, A. I. S.; Johansson, H. A. B.; Cederquist, H.; Zettergren, H., Dissociation and Multiple Ionization Energies for Five Polycyclic Aromatic Hydrocarbon Molecules. *J. Chem. Phys.* **2011**, *134*, 044301.

33. Gioumousis, G.; Stevenson, D. P., Reactions of Gaseous Molecule Ions with Gaseous Molecules. V. Theory. *J. Chem. Phys.* **1958**, *29*, 294.

34. Linstrom, P. J.; Mallard, W. G., Eds., In *NIST Chemistry WebBook, NIST Standard Reference Database Number 69*; NIST: Gaithersburg, MD, 2014.

35. Lide, D. R., Ed., *CRC Handbook of Chemistry and Physics*, 89th ed.; CRC Press: Boca Raton, FL, 2008.

36. Le Page, V.; Keheyan, Y.; Snow, T. P.; Bierbaum, V. M., Reactions of Cations Derived from Naphthalene with Molecules and Atoms of Interstellar Interest. *J. Am. Chem. Soc.* **1999**, *121*, 9435.

37. Betts, N. B.; Stepanovic, M.; Snow, T. P.; Bierbaum, V. M., Gas-Phase Study of Coronene Cation Reactivity of Interstellar Relevance. *Astrophys. J.* **2006**, *651*, L129.

38. Herbst, E.; Smith, D.; Adams, N. G.; McIntosh, B. J., Association Reactions. Theoretical Shortcomings. *J. Chem. Soc. Faraday Trans. 2* **1989**, *85*, 1655.

39. Herbst, E.; Le Page, V., Do H Atoms Stick to PAH Cations in the Interstellar Medium? *Astron. Astrophys.* **1999**, *344*, 310.

40. Ausloos, P.; Lias, S. G.; Buckley, T. J.; Rogers, E. E., Concerning the Formation and the Kinetics of Phenylium Ions. *Int. J. Mass Spectrom. Ion Process.* **1989**, *92*, 65.

41. Le Page, V.; Keheyan, Y.; Bierbaum, V. M.; Snow, T. P., Chemical Constraints on Organic Cations in the Interstellar Medium. *J. Am. Chem. Soc.* **1997**, *119*, 8373.

42. Clar, E., In *Polycyclic Hydrocarbons*, Vol. 1, Academic Press:New York, NY, 1964.

43. Bauschlicher, C. W., Jr., The Reaction of Polycyclic Aromatic Hydrocarbon Cations with Hydrogen Atoms: The Astrophysical Implications. *Astrophys. J. Lett.* **1998**, *509*, L125.

44. Dryza, V.; Sanelli, J. A.; Robertson, E. G.; Bieske, E. J., Electronic Spectra of Gas-Phase Polycyclic Aromatic Nitrogen Heterocycle Cations: Isoquinoline$^+$ and Quinoline$^+$. *J. Phys. Chem. A* **2012**, *116*, 4323.

45. Herbig, G. H., The Diffuse Interstellar Bands. *Annu. Rev. Astron. Astrophys.* **1995**, *33*, 19.

Chapter 4

Chemistry of CF^+ and its Relevance to the Interstellar Medium

4.1 Introduction

Photodissociation regions (PDRs) in the interstellar medium (ISM) provide a complex environment where rich chemistry can occur. The gaseous medium is mostly neutral, H_2 and CO are the dominant forms of hydrogen and carbon, photon energies are low (6 eV $\leq h\nu \leq$ 13.6 eV) and gas densities can vary widely (0.25–10^7 cm^{-3}) (cf. Hollenbach & Tielens [1]). While the chemistry of the more abundant elements H, C, N, and O has been explored in detail, the chemical reactivity of less abundant elements, like F, has received far less attention [2]. However, the lack of study of fluorine-containing species does not indicate that its chemistry is insignificant. Fluorine is unique, in that its ionization energy is greater than that of atomic hydrogen (17.42282 eV compared to 13.59844 eV; [3]) and that it reacts with molecular hydrogen in an exothermic process to form HF and H [2]. Although this reaction has a $\sim$1 kcal mol^{-1} barrier, the reaction rate is enhanced by tunneling at low temperatures [2]. In regions where H_2 is significant, HF becomes the dominant reservoir for fluorine [4]. The HF bond is the strongest H–X bond and the molecule is very stable. In diffuse clouds with high photon flux, such as PDRs, the predicted HF abundance can even exceed the abundance of CO [2].

The HF molecule is destroyed by photoionization and by reactions with He^+, H_3^+, and

C^+. In the transition regions in PDRs where carbon can be ionized, the reaction

$$C^+ + HF \longrightarrow CF^+ + H \tag{4.1}$$

can produce significant amounts of CF^+. In fact, CF^+, which is isoelectronic with CO, is predicted to be the second most abundant fluorine-containing molecule, with typical column densities $\sim$1% that of HF [2]. The recent detection of the CF^+ ion in the Orion Bar [5, 6] and the Horsehead nebula [7, 8] has validated the initial predictions of Neufeld et al. [2]. In addition, CF^+ has been proposed as the carrier of the 1384 Å diffuse interstellar band [9]. No electronic spectra of CF^+ have been measured experimentally; however, preliminary theoretical calculations of the electronic transition of CF^+ from the ground $X^1\Sigma^+$ state to the excited $A^1\Pi$ state are promising [10].

The CF^+ ion is primarily destroyed by fast ion-electron recombination [4]. An experimentally measured CF^+ dissociative recombination rate was included in the most current model incorporating fluorine-containing molecules by Neufeld & Wolfire [4]. This experimentally measured, temperature dependent rate coefficient ($k = 5.2 \times 10^{-8}(T/300K)^{-0.8}$ cm^3 s^{-1}; [11]) is smaller than the rate coefficient assumed in the previous model ($k = 2 \times 10^{-7}(T/300K)^{-0.5}$ cm^3 s^{-1}; [5]), and results in an overestimation of the CF^+ abundance by a factor $\gtrsim 10$ compared to the observed abundances in the Orion Bar [4]. Neufeld & Wolfire [4] attributed this discrepancy to an overestimation of the assumed C^+ + HF reaction rate coefficient; however, no chemical reactions of CF^+ with neutral molecules were included, and indeed there have been few experimental studies of the chemistry of CF^+. Here, we present the reactivity of CF^+ with prototypical groups of compounds. We have included 22 species previously detected in the ISM (H, H_2, N_2, O_2, CO, NO, HCl, H_2O, NH_3, CO_2, CH_4, OCS, N_2O, SO_2, CH_2O, C_2H_4, CH_3OH, $(CH_3)_2O$, CH_3CHO, $(CH_3)_2CO$, HCO_2CH_3, and c-C_6H_6; [12]) as well as NF_3, CF_4, and $(CH_3CH_2)_2O$. Deuterated methanol was used in place of methanol in this study due to the appearance of m/z 31 as a product ion, which is isobaric with CF^+. Although deuterated methanol has not been detected in the interstellar medium,

the rate constant and interpretation of the results will be similar for methanol within our experimental accuracy.

4.2 Methods

Reactions of CF^+ with 24 neutral molecules and H atom are investigated using a flowing afterglow-selected ion flow tube (FA-SIFT). Rate constants or upper limits in reactivity are measured under pseudo first-order conditions. Computatinal chemistry calculations are carried out to support the experimental results and give insight into reaction mechanisms and product distributions.

4.2.1 Experimental Methods

The experiments are carried out at 298 K using an FA-SIFT instrument (Figure 2.1). In this work, C^+ ions are generated by ionization of CO gas (100 eV ionization energy) in a helium buffer gas (0.30 Torr). Fluorine gas is introduced downstream of the ionization event and allowed to react with C^+ to produce CF^+. Ions are sampled through a differentially pumped orifice and the reagent ion is selected using a quadrupole mass filter. CF^+ ions are then injected into the reaction flow tube, and entrained in a flow of helium (0.35–0.50 Torr). Molecular nitrogen (0.01 Torr) is added 24 cm downstream of the injection inlet to ensure efficient cooling of vibrationally excited CF^+ prior to addition of neutral reactants [13]. Measured concentrations of neutral reactant molecules are added to the reaction flow tube through a manifold of inlets. The reactant ion signal is monitored as a function of reaction distance using a quadrupole mass filter coupled to an electron multiplier. Rate constants or upper limits in reactivity are derived using pseudo first-order kinetics [14].

Alternatively, atomic hydrogen is introduced into the reaction flow tube at a fixed reaction distance and the kinetics are monitored as a function of neutral concentration. Hydrogen atoms are generated by thermal dissociation of molecular hydrogen gas on a hot tungsten filament. The reactant ion signal is monitored as a function of filament voltage,

which is directly correlated to the concentration of atomic hydrogen [15, 16].

Product branching fractions were determined for reactions with multiple ionic products. The fraction of the individual product ion versus the total product ion intensity is plotted versus (1) reaction distance or (2) fraction of parent ion remaining. Primary product distributions are determined by extrapolating the data to (1) zero reaction distance or (2) zero reaction of the parent ion. Three values from each method are combined and an average product distribution is reported. Primary products with a branching fraction less than 0.10 are not reported.

4.2.2 Computational Methods

We have carried out ab initio and density functional theory calculations to support experimental studies. All computations were analyzed using the *Gaussian 09* [17] suite of programs. We have computed structures and geometries for reactants, intermediates, and products involved in the reactions studied at the B3LYP/aug-cc-pVTZ level of theory [18–21]. Previous calculations have been performed on systems involving fluorine [22–24] and sulfur [25], however, these methods prove to be expensive for systems larger than six atoms. We have modeled our calculations on the work of Matus et al. [22] with two modifications: (1) The B3LYP functional describes the geometry of the molecules investigated more accurately than MP2, when comparing frequencies and bond lengths to experimental data and (2) extrapolation to the complete basis set for the aug-cc-pVnZ formalism is not necessary for the accuracy of this work. The B3LYP functional combined with the correlation consistent aug-cc-pVTZ basis set best describes the geometry of the molecules investigated in this study, except for SO_2. Using these geometries, single-point energies were calculated at the CCSD(T)/aug-cc-pVTZ level of theory [26].

Computational chemistry calculations can become complicated when sulfur is bound to a highly electronegative element like oxygen [25]. The work of Denis [25] explored the use of Pople-type basis sets, cc-pV(D+X)Z and aug-cc-pV(D+X)Z correlation-consistent

Dunning-type basis sets, and the augmented polarized-consistent (aug-pc-X) basis set with the B3LYP method. The Pople-type basis set 6-311++G(*3df, 2p*) is inexpensive compared to the other basis sets explored, and the calculated values for SO and SO_2 by Denis [25] are in good agreement with other calculations and with experiment. For the reaction of CF^+ + SO_2, the structures and geometries for reactants, intermediates, and products involved in the reaction are determined at the B3LYP/6-311++G(*3df, 2p*) level of theory. Using these geometries, single-point energies were calculated at the CCSD(T)/6-311++G(*3df, 2p*) level of theory.

4.3 Results and Discussion

The reactions of CF^+ with 25 neutral species are summarized in Table 4.1. Product(s), product branching fractions, rate constants, reaction efficiencies, and enthalpies of reaction are given. Product distribution errors are ±30% of the reported values. The experimental precision, reported as 1σ of the mean, is better than ±10% for all reactions and there is a total error of ±20% for the reported rate constants. We report reaction efficiencies as $k_{\mathrm{exp}}/k_{\mathrm{col}}$, where k_{col} is the collision rate constant determined by Langevin theory [27] for neutral reactants without a permanent dipole moment and by parametrized trajectory theory [28] for molecules that possess a permanent dipole moment [3]. Experimental enthalpies of reaction, ΔH_{exp}, are determined using Hess's law with ionization energies, bond energies, proton affinities, and heats of formation ($\Delta_{\mathrm{f}}H$) taken from NIST Standard Reference Database Number 69 [29] and from the 89th edition of the CRC Handbook of Chemistry and Physics [3]. In addition, we determine enthalpies of reaction at 298 K using computational chemistry calculations. As previously reported, CF^+ vibrations are not sufficiently cooled by collisions with He [13]. To ensure that no vibrationally excited CF^+ was present in the reaction region, N_2 gas was added just downstream of the injection inlet. $CF^+(v = 1)$ will charge transfer with NO, whereas $CF^+(v = 0)$ will not. The reaction of CF^+ + NO was monitored and N_2 gas was added until minimal (<3%) charge transfer was observed (flow of $N_2 \approx 4$ std

Table 4.1: Reactions of CF^+ with neutral molecules

M	Product(s)	Product[a] Fractions	k_{exp}[b] (10^{-9} cm^3 s^{-1})	Efficiency[c]	ΔH_{exp}[d] (kcal mol^{-1})	ΔH_{theor}[e] (kcal mol^{-1})
			Triatomics			
OCS	$SCF^+ + CO$	1.0	0.63	0.42	...	-52.3
N_2O	$N_2F^+ + CO$	1.0	0.44	0.44	...	-24.8
SO_2	$FCO^+ + SO$	0.65	1.1	0.57	-17.3	-28.7[f]
	$SO^+ + FCO$	0.15			-1.1	-6.5[f]
	$FSO^+ + CO$	0.20			...	-65.5[f]
			Oxygen-Containing Organics			
CD_3OD	$CD_3^+ + CDFO$	0.55	2.0	0.89	-53.4[g]	-49.4
	$C_2D_3O^+ + DF$	0.45			...	-72.5
$(CH_3)_2O$	$CH_3^+ + CH_3F + CO$	0.70	1.6	0.82	-44.2	-46.3
	$C_2H_3O^+ + CH_3F$	0.30			...	-74.2
$(CH_3CH_2)_2O$	$C_2H_5^+ + C_2H_5F + CO$	1.0	1.8	0.88	-84.4	-80.8
CH_3CHO	$C_2H_3^+ + CHFO$	0.60	2.7	0.84	-53.8	-49.3
	$FCO^+ + C_2H_4$	0.40			-40.7	-41.9
$(CH_3)_2CO$	$C_3H_5^+ + CHFO$	1.0	3.0	0.90	...	-86.4[h]
HCO_2CH_3	$CH_3^+ + CHFO + CO$	0.75	2.1	0.94	-45.6	-44.5
	$CHO^+ + CH_3F + CO$	0.25			-72.3	-73.3
			NX_3			
NF_3	$CF_2^+ + NF_2$	0.35	0.81	0.80	-9.7	-11.2
	$NF_2^+ + CF_2$	0.50			-5.2	-6.9
	$CF_3^+ + NF$	0.15			-77.6	-85.0
NH_3	$HCNH^+ + HF$	1.0	1.2	0.50	-94.2	-95.3
			Hydrocarbons			
C_2H_4	$CH_2CCH^+ + HF$	0.80	1.0	0.80	-63.3	-61.0
	$CH_2F^+ + C_2H_2$	0.20			-28.6	-24.5
c-C_6H_6[i]	$C_5H_4F^+ + C_2H_2$	0.35	1.6	1.06	...	-25.3
	$C_7H_6F^+$	0.65			...	...

Notes. No measurable rate constants were obtained for reactions with H, H_2, N_2, O_2, CO, NO, HCl, H_2O, CO_2, CH_4, CF_4, CH_2O and we report a conservative upper limit for the rate constants of $k \leq 1 \times 10^{-12}$ cm^3 s^{-1}. Several ΔH values are not determined due to insufficient experimental data or computational limitations.

[a] Error bars are ±30% of the reported values.

[b] Rate coefficients are measured at 0.30–0.50 Torr. The experimental precision, reported as 1σ of the mean, is ±10% and there is a total error of ±20% for the reported rate constants. For OCS, the total error is ±50%.

[c] The reaction efficiency is reported as k_{exp}/k_{col}. The collisional rate constant, k_{col}, determined by Langevin theory [27] for reactions involving neutral species having no dipole moment and parametrized trajectory theory [28] for those reactions involving neutral species possessing a permanent dipole moment.

[d] Values determined using Hess's law with experimental values for ionization energies, bond energies, proton affinities, and heats of formation [3, 29].

[e] Energies are reported at 298 K. Energies are calculated at the CCSD(T)/aug-cc-pVTZ//B3LYP/aug-cc-pVTZ level of theory unless otherwise noted.

[f] Energies are calculated at the CCSD(T)/6-311++G(*3df, 2p*)//B3LYP/6-311++G(*3df, 2p*) level of theory.

[g] The experimental $\Delta_f H^o_{298}$(CDFO) is estimated from $\Delta_f H^o_{298}$(CHFO).

[h] Energy calculated at the B3LYP/aug-cc-pVTZ level of theory.

[i] Product fractions determined at 0.30 Torr He.

atm L min^{-1}). Rate constants were measured with and without the addition of N_2 for OCS, SO_2, NF_3, CF_4, C_2H_4, CD_3OD, $(CH_3)_2O$, CH_3CHO, $(CH_3)_2CO$, HCO_2CH_3, c-C_6H_6. This sampling includes fast, intermediate, and slow reactions, and all reactions with multiple ionic products. There were no measurable differences in the rate constants, except for CF_4. All reported product distributions were measured with the addition of N_2 to the reaction flow tube, except for c-C_6H_6, which is reported for pure He as described below. Product branching fractions for the two different analysis methods described above agree within ±5%. The data from both methods are averaged and reported in Table 4.1. Trends in reactivity for reactions of CF^+ with triatomics, oxygen-containing organics, CX_4/NX_3, and hydrocarbon molecules are discussed below. In addition, many molecules show no reactivity toward CF^+.

4.3.1 Triatomics

The reactions of OCS, N_2O, and SO_2 with CF^+ vary in reactivity and product distribution, however, each reaction produces the stable CO molecule. The products SCF^+ and N_2F^+, which accompany the production of CO, are the only ionic products observed for reaction with OCS and N_2O, respectively. Reaction with SO_2 produces a number of ionic species: FCO^+ (0.65), SO^+ (0.15), and FSO^+ (0.20). The potential energy surface for CF^+ + SO_2, Figure 4.1, provides insight into the product distributions. Although production of FSO^+ and CO is the most energetically favored pathway, the transition state (TS) barrier that exists along the potential energy surface for fluorine transfer from C to S (TS2) is ∼0.5 kcal mol^{-1} below the energy of the reactants. This high barrier inhibits CO production and the FCO^+ + SO reaction channel dominates the product distribution. The reaction enthalpy for the production of SO^+ + FCO is comparable to the energy of TS2, and the product fractions of SO^+ and FSO^+ are similar. As previously mentioned, computational chemistry calculations involving molecules such as SO and SO_2 can be difficult. The calculated ΔH_{theor} values reported in Table 4.1 appear to be shifted by a constant value when compared to the experimentally determined reaction exothermicities. This may result from

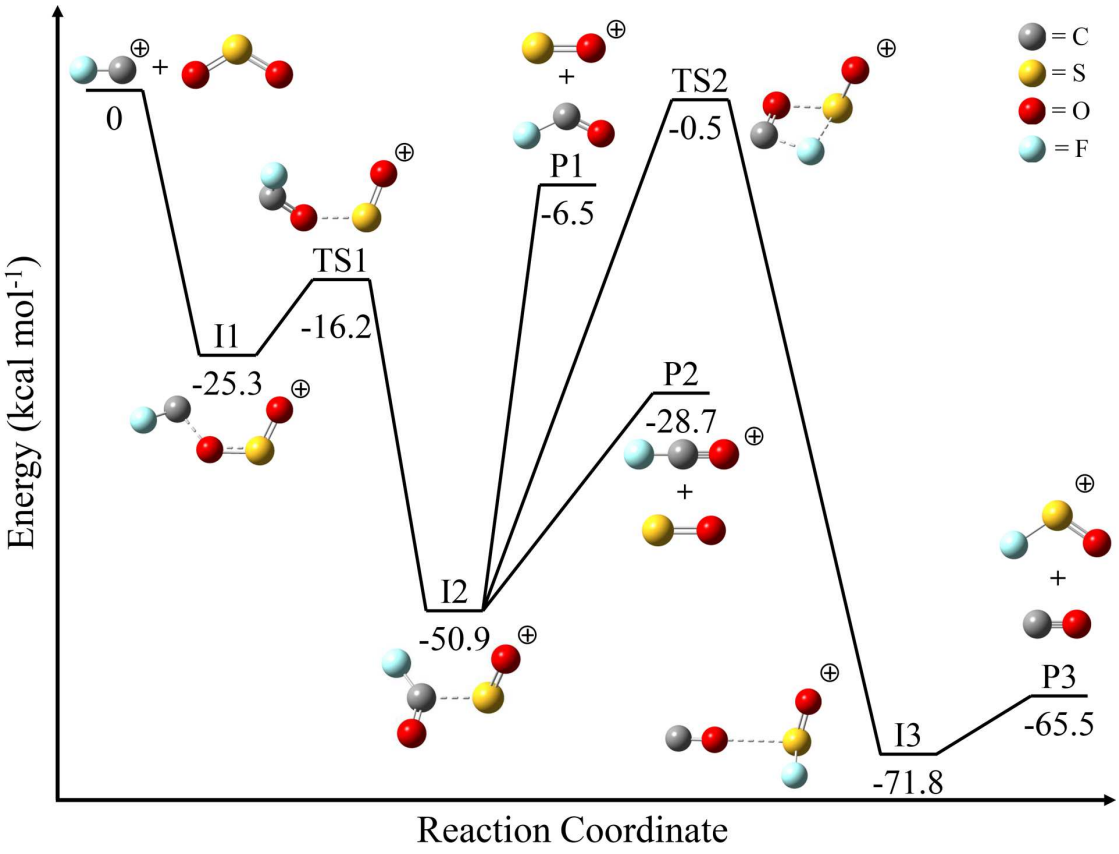

Figure 4.1: Reaction coordinate plot for the reaction $CF^+ + SO_2$. Intermediates (I), transition states (TS), and products (P) are labeled for reference. Energies were obtained from theoretical calculations performed at the CCSD(T)/6-311++G(*3df, 2p*)//B3LYP/6-311++G(*3df, 2p*) level of theory (kcal mol^{-1}).

an overestimation of the SO total atomization energy (TAE) and an underestimation of the SO_2 TAE in our theoretical calculations. Nonetheless, the general trends remain and data give insight into the reactivity and product distributions.

The absolute concentration of the OCS sample used in this study was initially unknown, and was determined using the calibration reaction CO^+ + OCS ($k = 1.2 \times 10^{-9}$ cm^3 s^{-1}; [30]). Therefore, the measured rate constant reported for the reaction of CF^+ + OCS has an associated error of ±50%. No reactivity was observed for the reactions of CF^+ with CO_2 and H_2O and we report a conservative upper limit for the rate constants of $k \leq 1 \times 10^{-12}$ cm^3 s^{-1}.

4.3.2 Oxygen-Containing Organics

Similar to the triatomics, reactions of CF^+ with CD_3OD, $(CH_3)_2O$, $(CH_3CH_2)_2O$, CH_3CHO, $(CH_3)_2CO$, and HCO_2CH_3 result in dominant neutral products, CO and CHFO. Deuterated methanol was used in this study to allow measurement of the reaction rate constant without hindrance from secondary ionic products that appear at m/z 31. Kinetic isotope effects are estimated to be small for this reaction, and the results for CD_3OD are expected to be similar to those of CH_3OH. According to our calculations, attack at the oxygen sites by CF^+ is a barrierless process for the oxygen-containing organics included in this study. Formation of an initial reactive complex at any of the carbons is likely inhibited by steric effects and unfavorable charge distribution. In addition, initial HF bond formation is not energetically favorable, as is evident by the endothermicity of the reverse reaction for Equation 4.1. All reactions of CF^+ with oxygen-containing organics are fast. This likely results from formation of a very stable pre-reaction complex (RO–CF^+) and the low barriers along the reaction surface. Two different sets of mechanistic pathways exist for the oxygen-

containing organics investigated in this study. First, the reaction:

$$CF^+ + ROR' \longrightarrow R^+ + [R'OCF] \quad (4.2)$$

$$\longrightarrow ROC^+ + [R'F] \quad (4.3)$$

is representative of reactions with CD_3OD, $(CH_3)_2O$, and $(CH_3CH_2)_2O$ (where R = CH_3, or CH_3CH_2 and R' = H, CH_3, or CH_3CH_2). Equation 4.2 is the less energetic pathway, yet it is the dominant reaction channel for CD_3OD and $(CH_3)_2O$, and the exclusive pathway for $(CH_3CH_2)_2O$. As shown in Figure 4.2, after the initial attack of CF^+ on the oxygen of CD_3OD, the TS barrier for hydrogen transfer to the CF^+ carbon (TS3, -23.0 kcal mol^{-1}) is similar in energy to hydrogen transfer to the fluorine (TS4, -22.8 kcal mol^{-1}). This similarity in energy results in almost equivalent distributions of Equations 4.2 and 4.3. The reaction mechanisms for CF^+ with $(CH_3)_2O$ and $(CH_3CH_2)_2O$ were not explored computationally. The lack of correlation between reaction enthalpy and product distribution for the reactions of $(CH_3)_2O$ is likely the result of the more exothermic reaction having a higher TS barrier.

Secondly, the reaction:

$$CF^+ + CH_3CRO \longrightarrow [C_2H_2R]^+ + CHFO \quad (4.4)$$

$$\longrightarrow FCO^+ + [C_2H_3R] \quad (4.5)$$

is representative of reactions with CH_3CHO and $(CH_3)_2CO$. Equation 4.4 involves hydrogen transfer from a methyl group to the CF^+ carbon and Equation 4.5 is an oxygen-atom abstraction with rearrangement of the neutral product. In the case of CH_3CHO, Equation 4.4 is slightly more exothermic than Equation 4.5, which is reflected by the product fractions, 0.60 compared to 0.40. The ionic product of Equation 4.5, FCO^+, is not observed for reaction with acetone. This is likely because the TS barrier (TS6) along the reaction coordinate to produce the products in Equation 4.5 is higher in energy than the TS (TS5) associated with Equation 4.4. The simplified potential energy surface for the reaction of $CF^+ + (CH_3)_2CO$ for Equations 4.4 and 4.5 is shown in Figure 4.3. Due to computational limitations, the

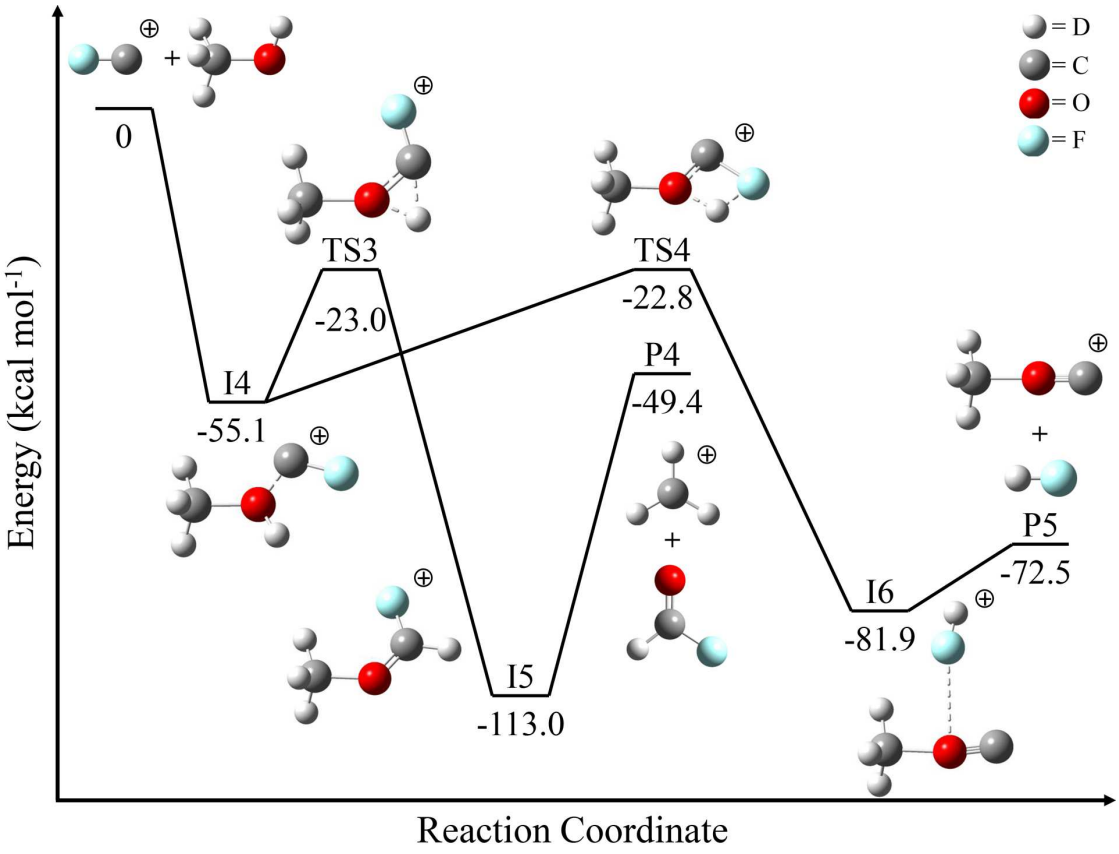

Figure 4.2: Reaction coordinate plot for the reaction $CF^+ + CD_3OD$. Intermediates (I), transition states (TS), and products (P) are labeled for reference. Energies were obtained from theoretical calculations performed at the CCSD(T)/aug-cc-pVTZ//B3LYP/aug-cc-pVTZ level of theory (kcal mol^{-1}).

geometries and energies in Figure 4.3 were calculated at the B3LYP/aug-cc-pVTZ level of theory. For the energies that were calculated using both levels of theory, B3LYP always predicts a lower energy by ∼10 kcal mol^{-1} and the general trends remain. The neutral product for Equation 4.4 is fluorinated formaldehyde since the mechanism for loss of HF and CO is inhibited by a TS above the energy of the reactants (not shown in Figure 4.3). In addition, the neutral products for Equation 4.5 for reaction of CF^+ with CH_3CHO and $(CH_3)_2CO$ are likely C_2H_4 and CH_2CHCH_3, respectively. The neutral species produced from oxygen-atom abstraction without rearrangement results in products above the energy of the reactants, 32.5 kcal mol^{-1} for FCO^+ + CH_3CH and 22.6 kcal mol^{-1} for FCO^+ + CH_3CCH_3.

The reaction of CF^+ with HCO_2CH_3 is the most efficient of the oxygen-containing organics. The reaction mechanisms were not explored computationally and neutral products are suggested. Similar to the reactions of $(CH_3)_2O$ and $(CH_3CH_2)_2O$, the lack of correlation between reaction enthalpies and product distributions are likely the result of the more exothermic reaction having a higher TS barrier.

4.3.3 CX_4/NX_3

The reactions of CF^+ with CH_4, CF_4, NH_3, and NF_3 vary widely in their reactivity and product distribution. CH_4 and CF_4 are unreactive with CF^+. Hydrogen transfer from CH_4 to CF^+ is not energetically allowed, and HF formation is unfavorable. Although previous work has assigned a rate constant for reaction with CF_4, the data were obscured by curvature in the pseudo first-order kinetic plots [13]. As described above, we have introduced N_2 to collisionally relax $CF^+(v > 0)$ and ensure that these ions are in the ground vibrational state. When CF^+ was not cooled by N_2, m/z 69 (CF_3^+) was observed in the product spectra. Morris et al. [13] reported ΔH_{exp} = -6 kcal mol^{-1} for the reaction

$$CF^+ + CF_4 \longrightarrow CF_3^+ + CF_2. \tag{4.6}$$

In contrast, using more recent values, we have determined that ΔH_{exp} = 5 kcal mol^{-1}.

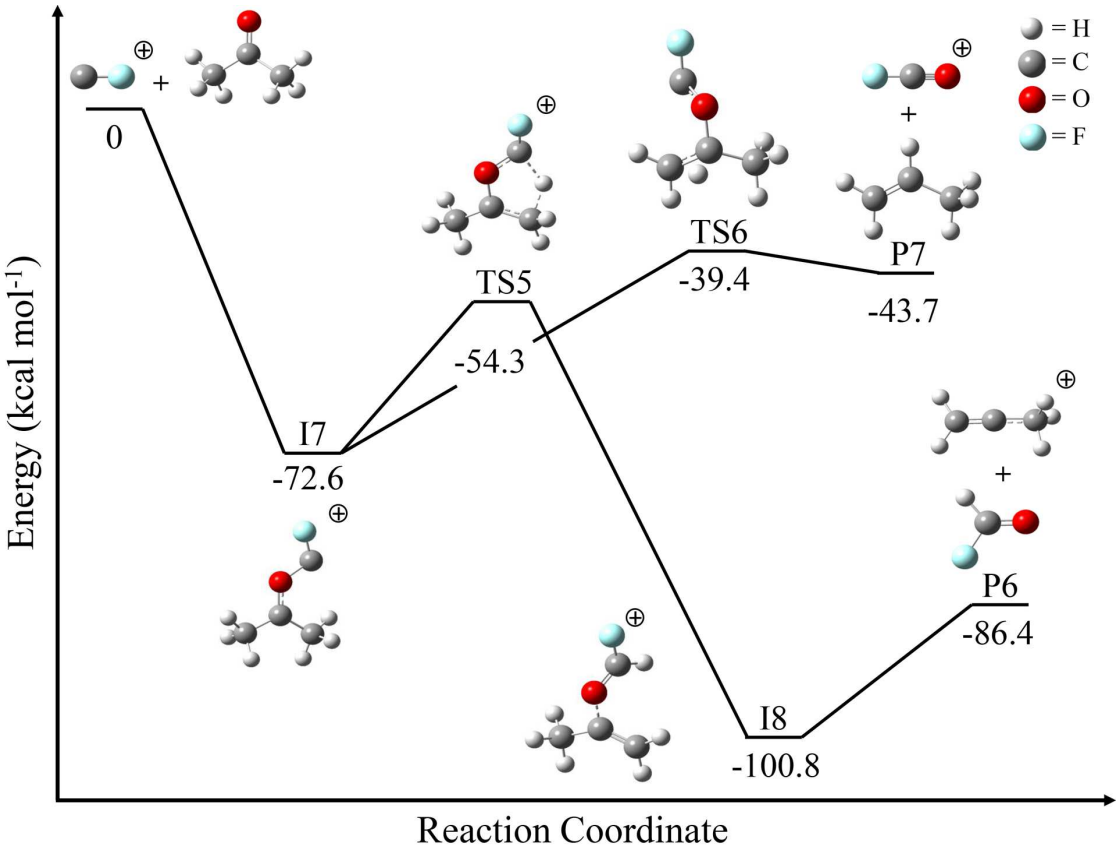

Figure 4.3: Reaction coordinate plot for the reaction $CF^+ + (CH_3)_2CO$. Intermediates (I), transition states (TS), and products (P) are labeled for reference. Energies were obtained from density functional theory calculations performed at the B3LYP/aug-cc-pVTZ level of theory (kcal mol^{-1}).

The $\Delta_f H$ of CF^+, CF_3^+, and CF_2 used in our study were taken from Harvey et al. [31] and have associated errors of approximately ± 1 kcal mol^{-1}, while the $\Delta_f H(CF_4)$ was taken from Linstrom & Mallard [29] and has an associated error of $\pm$ 1.2 kcal mol^{-1} . In addition, the $\Delta_f H(CF_3^+)$ used by Morris et al. [13] is 17 kcal mol^{-1} lower in energy than the value used here. Thus, we report no observed reaction for CF^+ with CF_4 and place a conservative upper limit on the rate constants for reaction of CF^+ with CH_4 and CF_4 of $k \leq 1 \times 10^{-12}$ cm^3 s^{-1}.

The reactions of CF^+ with NH_3 and NF_3 differ in their reaction efficiency and product distributions. The reaction of NH_3 with CF^+ involves formation of a CN triple bond, hydrogen transfer from N to C, and loss of HF. This multi-step mechanism likely makes this reaction less efficient than the NF_3 reaction. There are three isomers of [2H, C, N]$^+$: H_2CN^+, CNH_2^+, and $HCNH^+$. The first structure is highly unstable, and is not likely produced in this reaction [32]. We have calculated the proton affinity (PA) of CNH + $H^+ \longrightarrow CNH_2^+$ to be 130 kcal mol^{-1}. The experimentally determined PA of HCN is 170 kcal mol^{-1}. H_2O (PA = 165 kcal mol^{-1}) and C_2H_4 (PA = 160 kcal mol^{-1}) were used to probe the structure of [2H, C, N]$^+$. A sufficient amount of NH_3 was added to completely deplete the CF^+ ion intensity and H_2O or C_2H_4 was introduced downstream from this reaction event. If a significant amount of CNH_2^+ were present, rapid proton transfer reactions would be expected with H_2O and C_2H_4; however, these reactions were not observed, confirming the ionic structure as $HCNH^+$.

Three ionic products were observed for the reaction of CF^+ + NF_3: CF_2^+, NF_2^+, and CF_3^+. The reaction enthalpies for the formation of CF_2^+ + NF_2 and NF_2^+ + CF_2 are similar, but the product branching fraction for NF_2^+ is 0.50. From a Lewis structure formalism, the positive charge is located on the N atom. Although the IE of CF_2 (11.44 eV) is slightly lower than that of NF_2 (11.63 eV), it is more favorable for the positive charge to remain on the N in the association pre-reactive complex. Similar to the reaction mechanism for $(CH_3)_2CO$, the most energetically favored ionic product, CF_3^+, is the least favored in product distribution. The lack of correlation between reaction enthalpies and product distributions are likely the result of the more exothermic reaction having a higher TS barrier.

4.3.4 Hydrocarbons

The reactivity of the hydrocarbons CH_4, C_2H_4, and c-C_6H_6 with CF^+ has been explored. As mentioned above, CH_4 is unreactive with CF^+. The reaction with C_2H_4 has been studied previously [33]. Our reported overall rate constant of 1.0×10^{-9} cm^3 s^{-1} agrees with the value reported by Simpson & Tuckett [33] (1.1×10^{-9} cm^3 s^{-1}), within experimental errors. In addition, we observe the same ionic products and report equivalent branching fractions (Table 4.1) [33].

Reactions of ions with neutral polycyclic aromatic hydrocarbons (PAHs) are difficult to study in the FA-SIFT. However, we have examined the reaction of CF^+ with the building block of PAHs, c-C_6H_6. Two ionic products are observed for this reaction, $C_5H_4F^+$ and $C_7H_6F^+$. Addition of N_2 to the reaction flow tube to collisionally cool the CF^+ ions resulted in a fraction of >0.9 association product. For this reason, the product fractions and rate constant listed in Table 4.1 for the reaction of CF^+ with c-C_6H_6 are determined at 0.30 Torr He without the addition of N_2. The minor reaction channel under these experimental conditions is destruction of c-C_6H_6 with the loss of C_2H_2. The association product, $C_7H_6F^+$, is stabilized by the He buffer gas in the FA-SIFT. At the low pressures of the ISM, this association of CF^+ with PAHs may occur through radiative association [34].

As described above, vibrationally excited CF^+ is not efficiently cooled by He. We do observe a small fraction (≤ 0.1) of charge transfer with benzene using pure He as the buffer gas and attribute this to reaction with $CF^+(v > 0)$. Since all PAHs have lower IEs than CF, the charge transfer channel will compete with the C_2H_2-loss and radiative association channel. We were not able to calculate a theoretical reaction enthalpy for the formation c-$C_7H_6F^+$ due to computational limitations; however, this product must be lower in energy than the other two reaction channels because bond formation without bond breaking is highly exothermic.

4.3.5 Neutral Molecules Showing No Reaction

As mentioned above, CO_2, H_2O, CH_4 and CF_4 are unreactive with CF^+. In addition, no measurable rate constants were obtained for the reactions of CF^+ with H, H_2, N_2, O_2, CO, NO, HCl, and CH_2O and we report a conservative upper limit for the rate constants of $k \leq 1 \times 10^{-12}$ cm^3 s^{-1}.

4.4 Conclusion

We have investigated the reactivity of CF^+ with prototypical groups of compounds, many of which have been detected in the ISM. The results from this study indicate that:

(1) CF^+ is highly reactive with complex molecules, but relatively inert toward diatomic molecules. This will result in an increased destruction rate in dense molecular environments and allow survival of CF^+ in diffuse regions.

(2) The stable molecule CO is a dominant product in the reactions of CF^+.

(3) The variations in reactivity for the reactions involving SO_2, CD_3OD, $(CH_3)_2CO$, and NF_3 have been discussed by examining the potential energy surfaces. Dynamic effects due to transition state barriers along the potential energy surface likely control the reactivity of these processes.

(4) The reaction of CF^+ with CF_4 has been reexamined. The curved feature in the kinetic plots observed by previous researchers was likely the result of vibrationally excited CF^+.

We suggest, from a chemical standpoint, that CF^+ will have the greatest probability of detection in the regions where it is initially formed; these regions include the transition zones where the photon flux is sufficient to ionize C^+, but low enough that HF can form in high densities. This result is consistent with the suggestions that CF^+ is the carrier of the

1384 Å DIB since DIB intensities are known to be strongest in regions of high photon flux, where H atom is dominant, and diminish in dense regions where molecular hydrogen is in high abundance [35].

4.5 References

1. Hollenbach, D. J.; Tielens, A. G. G. M., Photodissociation Regions in the Interstellar Medium of Galaxies. *Rev. Modern Phys.* **1999**, *71*, 173.

2. Neufeld, D. A.; Wolfire, M. G.; Schilke, P., The Chemistry of Fluorine-Bearing Molecules in Diffuse and Dense Interstellar Gas Clouds. *Astrophys. J.* **2005**, *628*, 260.

3. Lide, D. R., Ed. *CRC Handbook of Chemistry and Physics*, 89th ed.; Taylor and Francis: Boca Raton, FL, 2008.

4. Neufeld, D. A.; Wolfire, M. G., The Chemistry of Interstellar Molecules Containing the Halogen Elements. *Astrophys. J.* **2009**, *706*, 1594.

5. Neufeld, D. A.; Schilke, P.; Menten, K. M.; Wolfire, M. G.; Black, J. H.; Schuller, F.; Müller, H. S. P.; Thorwirth, S.; Güsten, R.; Philipp, S., Discovery of Interstellar CF^+. *Astron. Astrophys.* **2006**, *454*, L37.

6. Nagy, Z.; Van der Tak, F. F. S.; Ossenkopf, V.; Gerin, M.; Le Petit, F.; Le Bourlot, J.; Black, J. H.; Goicoechea, J. R.; Joblin, C.; Röllig, M.; Bergin, E. A., The Chemistry of Ions in the Orion Bar I. – CH^+, SH^+, and CF^+. *Astron. Astrophys.* **2013**, *550*, A96.

7. Guzmán, V.; Pety, J.; Gratier, P.; Goicoechea, J. R.; Gerin, M.; Roueff, E.; Teyssier, D., The IRAM-30m Line Survey of the Horsehead PDR. *Astron. Astrophys.* **2012**, *543*, L1.

8. Guzmán, V.; Roueff, E.; Gauss, J.; Pety, J.; Gratier, P.; Goicoechea, J. R.; Gerin, M.; Teyssier, D., The Hyperfine Structure in the Rotational Spectrum of CF^+. *Astron. Astrophys.* **2012**, *548*, A94.

9. Roueff, E., *Private Communication*. **2014**.

10. Petsalakis, I. D.; Theodorakopoulos, G., Electronic States of CF^+. *Chem. Phys.* **2000**, *254*, 181.

11. Novotny, O.; Mitchell, J. B. A.; LeGarrec, J. L.; Florescu-Mitchell, A. I.; Rebrion-Rowe, C.; Svendsen, A.; Ghazaly, M. A. E.; Andersen, L. H.; Ehlerding, A.; Viggiano, A. A.; Hellberg, F.; Thomas, R. D.; Zhaunerchyk, V.; Geppert, W. D.; Montaigne, H.; Kaminska, M.; Österdahl, F.; Larsson, M., The Dissociative Recombination of Fluorocarbon Ions: II. CF^+. *J. Phys. B* **2005**, *38*, 1471.

12. Woon, D. E. The Astrochymist. http://astrochymist.com (accessed July 11, 2014).

13. Morris, R. A.; Viggiano, A. A.; Van Doren, J. M.; Paulson, J. F., Chemistry of CF_n^+ (n = 1–3) Ions with Halocarbons. *J. Chem. Phys.* **1992**, *96*, 2597.

14. Bierbaum, V. M., Flow Tubes. In *Encyclopedia of Mass Spectrometry*, Armentrout, P. B., Ed.; Elsevier: Amsterdam, 2003; p 940.

15. Trainor, D. W.; Ham, D. O.; Kaufman, F., Gas Phase Recombination of Hydrogen and Deuterium Atoms. *J. Chem. Phys.* **1973**, *58*, 4599.

16. Barckholtz, C.; Snow, T. P.; Bierbaum, V. M., Reactions of C_n^- and C_nH^- with Atomic and Molecular Hydrogen. *Astrophys. J. Lett.* **2001**, *547*, L171.

17. Frisch, M. J.; Trucks, G. W.; Schlegel, H. B.; Scuseria, G. E.; Robb, M. A.; Cheeseman, J. R.; Scalmani, G.; Barone, V.; Mennucci, B.; Petersson, G. A. et al. *Gaussian 09*, Revision D.01; Gaussian Inc.: Wallingford, CT, 2009.

18. Becke, A. D., Density-Functional Thermochemistry. III. The Role of Exact Exchange. *J. Chem. Phys.* **1993**, *98*, 5648.

19. Lee, C.; Yang, W.; Parr, R. G., Development of the Colle-Salvetti Correlation-Energy Formula into a Functional of the Electron Density. *Phys. Rev. B* **1988**, *37*, 785.

20. Dunning, T. H., Gaussian Basis Sets for Use in Correlated Molecular Calculations. I. The Atoms Boron Through Neon and Hydrogen. *J. Chem. Phys.* **1989**, *90*, 1007.

21. Dunning, T. H.; Peterson, K. A.; Wilson, A. K., Gaussian Basis Sets for Use in Correlated Molecular Calculations. X. The Atoms Aluminum Through Argon Revisited. *J. Chem. Phys.* **2001**, *114*, 9244.

22. Matus, M. H.; Nguyen, M. T.; Dixon, D. A.; Christe, K. O., Thermochemical Parameters of CHFO and CF_2O. *J. Phys. Chem. A* **2008**, *112*, 4973.

23. Nguyen, M. T.; Matus, M. H.; Ngan, V. T.; Haiges, R.; Christe, K. O.; Dixon, D. A., Energetics and Mechanism of the Decomposition of Trifluoromethanol. *J. Phys. Chem. A* **2008**, *112*, 1298.

24. Feller, D.; Peterson, K. A.; Dixon, D. A., Ab Initio Coupled Cluster Determination of the Heats of Formation of $C_2H_2F_2$, C_2F_2, and C_2F_4. *J. Phys. Chem. A* **2011**, *115*, 1440.

25. Denis, P. A., Basis Set Requirements for Sulfur Compounds in Density Functional Theory: a Comparison Between Correlation-Consistent, Polarized-Consistent, and Pople-Type Basis Sets. *J. Chem. Theo. Comp.* **2005**, *1*, 900.

26. Bartlett, R. J.; Musiał, M., Coupled-Cluster Theory in Quantum Chemistry. *Rev. Modern Phys.* **2007**, *79*, 291.

27. Gioumousis, G.; Stevenson, D. P., Reactions of Gaseous Molecule Ions with Gaseous Molecules. V. Theory. *J. Chem. Phys.* **1958**, *29*, 294.

28. Su, T.; Chesnavich, W. J., Parametrization of the Ion-Polar Molecule Collision Rate Constant by Trajectory Calculations. *J. Chem. Phys.* **1982**, *76*, 5183.

29. Linstrom, P. J., Mallard, W. G., Ed.; *NIST Chemistry WebBook, NIST Standard Reference Database Number 69*, 2014, http://webbook.nist.gov/chemistry/.

30. Adams, N. G.; Smith, D.; Grief, D., Reactions of H_nCO^+ Ions with Molecules at 300 K. *Int. J. Mass Spectrom. Ion. Phys.* **1978**, *26*, 405.

31. Harvey, J.; Bodi, A.; Tuckett, R. P.; Sztaray, B., Dissociation Dynamics of Fluorinated Ethene Cations: From Time Bombs on a Molecular Level to Double-Regime Dissociators. *Phys. Chem. Chem. Phys.* **2012**, *14*, 3935.

32. Burgers, P. C.; Holmes, J. L.; Terlouw, J. K., Gaseous $[H_2, C, N]^+$ and $[H_3, C, N]^{+\cdot}$ Ions. Generation, Heat of Formation, and Dissociation Characteristics of $[H_2CN]^+$, $[HCNH]^+$, $[CNH_2]^+$, $[H_2CNH]^{+\cdot}$, and $[HCNH_2]^{+\cdot}$. *J. Am. Chem. Soc.* **1984**, *106*, 2762.

33. Simpson, M. J.; Tuckett, R. P., Selected Ion Flow Tube Study of the Gas-Phase Reactions of CF^+, CF_2^+, CF_3^+, and $C_2F_4^+$ with C_2H_4, C_2H_3F, CH_2CF_2, and C_2HF_3. *J. Phys. Chem. A* **2012**, *116*, 8119.

34. Herbst, E.; Le Page, V., Do H Atoms Stick to PAH Cations in the Interstellar Medium? *Astron. Astrophys.* **1999**, *344*, 310.

35. Herbig, G. H., The Diffuse Interstellar Bands. *Annu. Rev. Astron. Astrophys.* **1995**, *33*, 19.

Chapter 5

Gas-Phase Reactions of Hydride Anion, H^-

5.1 Introduction

The anion of the hydrogen atom, though seemingly simple, has drawn much attention because of its involvement in many reactions important to our understanding of cosmology and astrophysics. Hydride, H^-, has been implicated in the formation of H_2, the first coolant available to the universe for seeding star and galaxy formation after the Big Bang [1]. Although detection of H^- in astrophysical environments remains elusive [2], a firm acceptance of its presence exists. The hydride ion has been correlated to the opacity of the Sun and other similar stars [3–6]. In addition, H^- has been predicted to exist in regions of the interstellar medium (ISM) such as the transition zones of photodissociation regions, dense clouds, and planetary nebulae [7]. In these dense environments the population of neutral hydrogen and free electrons suggests the existence of H^-. In 2000, Field [8] proposed a model suggesting hydride may also be involved in H_2 formation via an associative detachment (AD) process similar to the one that was important in the early universe. However, in this case, H^- production occurs on the surface of dust grains with weakly bound surface electrons rather than by direct electron capture by hydrogen atoms.

A variety of regions with the likely presence of H^- overlap molecular regions at their boundaries. An assorted range of chemical processes can be expected because of the reactivity of the hydride anion. Thus, an understanding of this reactivity should reveal the degree to which H^- drives astrophysical processes. Neutral reactants employed in this study

were chosen to map the chemistry of H^- with representatives from prototypical groups of compounds. Eleven of the compounds studied [C_2H_2, H_2O, CH_3CN, CH_3OH, $(CH_3)_2CO$, CH_3CHO, N_2O, CO_2, O_2, CO, and c-C_6H_6] have been detected in the interstellar medium (ISM)[9]. Rate constants for the reaction of H^- with the neutral molecules C_2H_2, H_2O, CH_3CN, N_2O, CO_2, O_2, CO, CH_3Cl, and c-C_6H_6 were previously determined to test ion-molecule collision models [10–17]. Here, we increase the number and source of existing measurements and contribute seven previously unmeasured reaction rate constants of H^- with the molecules CH_3OH, $(CH_3)_2CO$, CH_3CHO, CO_2, $(CH_3)_3CCl$, $(CH_3CH_2)_2O$, and D_2.

5.2 Methods

5.2.1 Experimental Methods

Experiments were carried out using a flowing afterglow apparatus [18, 19]. The hydride ion, m/z 1, poses two major challenges in that low mass ions are difficult to transport efficiently and are challenging to detect using a quadrupole mass filter. Attempts were made to generate H^- ions in the source flow tube; however, mass selection and injection into the reaction flow tube were not successful. Efficient scattering of hydride ions by helium in the injection process at the Venturi inlet is likely the cause of this difficulty [18]. In addition, tuning the detection quadrupole mass filter to transmit extremely low-mass ions is challenging due to the occurrence of the "on blast"; this is the transmission of all ions when the voltages on the quadrupole mass filter are set near zero. Proper tuning of the instrument was achieved with assistance from the staff at Extrel Corporation [18]. In this case, H^- is formed by electron ionization (70 eV ionization energy; 1–2 μA) on a trace amount of ammonia gas (NH_3; 99.9995%) via the dissociative attachment process [18]

$$NH_3 + e^- \longrightarrow H^- + NH_2. \tag{5.1}$$

Ions are formed in low density ($< 10^7$ ions cm^{-3}) to establish the existence of free diffusion. Sufficient concentration of NH_3 was used to ensure that hydride formation (ionization) was

complete before the reaction region. After the ionization event ions are thermalized by collisions with the helium carrier gas. Molecular reagents of known concentration are added to the reaction flow tube through a manifold of inlets. The decrease of the reactant-ion signal is monitored as a function of reaction distance by a quadrupole mass filter coupled to an electron multiplier. Reactions are carried out under pseudo first-order conditions and a standard kinetic analysis is used to determine rate constants [19].

The neutral reagents are acetylene (C_2H_2; $\geq$ 99.6%), water (H_2O; deionized), acetone [$(CH_3)_2CO$; $\geq$ 99.5%], acetonitrile (CH_3CN; 99.8%), methanol (CH_3OH; $\geq$ 99.9), acetaldehyde (CH_3CHO; $\geq$ 99.5%), nitrous oxide (N_2O; 99.0%), carbon dioxide (CO_2; $\geq$ 99%), oxygen (O_2; $\geq$ 99.994%), carbon monoxide (CO; 99.5%), methyl chloride (CH_3Cl; 99.5%), *tert*-butyl chloride [$(CH_3)_3CCl$; $\geq$ 99.5%], deuterium (D_2; $\geq$ 99.8%), diethyl ether [$(CH_3CH_2)_2O$; 99.9%], and benzene (c-C_6H_6; $\geq$ 99.9%).

5.2.2 Computational Methods

We have carried out ab initio calculations to support our experimental studies. Energies and structures for reactants, products, and intermediates involved in the reactions were determined using *Gaussian 09* [20]. The CCSD(T)/aug-cc-pVDZ level of theory is used for open-shell species such as molecular oxygen to minimize spin contamination on the energetics [21, 22]. Alternatively, all other calculations are carried out at the MP2(full)/aug-cc-pVDZ level of theory [23]. Reaction enthalpies are determined at 298 K using theoretically calculated energies. The potential energy surface for the reactions of H^- with N_2O, CO_2, and CH_3Cl have been explored, Section 5.3.

5.3 Results and Discussion

The results for all reactions are summarized in Table 5.1; this table includes rate constants, reaction efficiencies, prior literature values, and experimental and theoretical exothermicities determined at 298 K. We observe a wide range of rate constants and their resulting

Table 5.1: Hydride/neutral molecule reactions

Neutral Reactant	Product(s)	k_{exp}[a] (10^{-9} cm^3 s^{-1})	Efficiency[b] (k_{exp}/k_{col})	Literature Values (10^{-9} cm^3 s^{-1})	ΔH_{exp}[c] (kcal mol^{-1})	ΔH_{theor}[d] (kcal mol^{-1})
			Proton Abstraction Reactions			
C_2H_2	$C_2H^- + H_2$	3.1 ±0.3	0.70	4.42[e] (±25%)	-21.6	-24.1
H_2O[f]	$OH^- + H_2$	4.8 ±1.1	0.61	3.7[g] (±25%), 3.8[h] (±30%),	-10.3	-12.5
CH_3CN	$CH_2CN^- + H_2$	11 ±1	0.57	13[i] (±25%)	-26.3	-25.1
CH_3OH	$CH_3O^- + H_2$	6.1 ±0.8	0.66	N/A	-18.6	-19.5
$(CH_3)_2CO$	$CH_3COCH_2^- + H_2$	7.0 ±0.8	0.47	N/A	-31.8	-31.5
CH_3CHO	$CH_2CHO^- + H_2$	6.4 ±1.1	0.51	N/A	-34.9	-34.0
			Atom Abstraction/Addition Reactions			
N_2O	$OH^- + N_2$	1.0 ±0.1	0.23	1.1[j] (±0.3)	-87.7	-87.4
CO_2	HCO_2^-	0.09 ±0.02	0.022	N/A	-50.9	-52.0
			Associative Detachment Reactions			
O_2	$HO_2 + e^-$	1.4 ±0.1	0.46	1.2[j] (±20%)	-34.2	29.4[k]
CO	$CHO + e^-$	0.020 ±0.008	0.007	≅0.05[j]	2.1	-0.9
			S_N2/E2 Reactions			
CH_3Cl	$Cl^- + CH_4$	2.5 ±0.1	0.23	3.0[l] (±20%)	-85.0	-91.4
$(CH_3)_3CCl$	$Cl^- + H_2 + (CH_3)_2CCH_2$	4.0 ±0.5	0.32	N/A	-76.2	-78.0

Notes. No measurable rate constants were obtained for the reactions of H^- with D_2, $(CH_3CH_2)_2O$, c-C_6H_6.

[a] The error bars associated with the reported values represents 1σ of the mean of the experimental measurements. There is a total absolute error of ±20%.

[b] k_{col} is the collisional rate constant determined by Langevin theory [24] for reactions involving neutral species without a dipole moment and by parametrized trajectory theory [25] for those reactions involving neutral species with dipole moments.

[c] Values determined using Hess's law with experimental values for ionization energies, bond energies, electron affinities, and heats of formation [26, 27].

[d] Energies calculated at the MP2(full)/aug-cc-pVDZ theory level at 298 K.

[e] Mackay et al. [10]

[f] Stockdale et al. [13] reported an unreasonably high value of 5.4 (±1.6) × 10^{-7} cm^3 s^{-1}

[g] Betowski et al. [11]

[h] Melton & Neece [12]

[i] Mackay et al. [14]

[j] Dunkin et al. [15]

[k] Energy calculated at the CCSD(T)/aug-cc-pVDZ theory level at 298 K.

[l] Tanaka et al. [16]

efficiencies. There is a total absolute error of ±20% associated with the reported rate constants due to the experimental method. Furthermore, reaction rate constants are reported with error bars representing 1σ of the mean, an indication of the precision of our measurements. For comparison, we report reaction efficiencies as $k_{\mathrm{exp}}/k_{\mathrm{col}}$, where k_{col} is the collisional rate constant determined by Langevin theory [24] for reactions involving neutral species without a dipole moment [D_2, O_2, CO_2, C_2H_2, and c-C_6H_6] and by parametrized trajectory theory [25] for those reactions involving neutral species with dipole moments [CO, H_2O, N_2O, CH_3Cl, CH_3OH, CH_3CN, CH_3CHO, $(CH_3)_2CO$, $(CH_3)_3CCl$, and $(CH_3CH_2)_2O$; 26]. Enthalpies of reaction, ΔH_{exp}, have been determined using Hess's law with values for ionization energies, bond energies, electron affinities, and heats of formation taken from the CRC Handbook of Chemistry and Physics [26] and the NIST Chemistry WebBook [27]. For discussion, reactions have been categorized into five groups based on reaction mechanism: proton abstraction reactions, atom abstraction or addition reactions, associative detachment reactions, nucleophilic substitution (S_N2)/elimination (E2) reactions, and a final group where reactions are not observed.

5.3.1 Proton Abstraction Reactions

The neutral reagents C_2H_2, H_2O, CH_3CN, CH_3OH, $(CH_3)_2CO$, and CH_3CHO react with H^- to form H_2 via

$$\mathrm{RH} + \mathrm{H}^- \longrightarrow \mathrm{R}^- + \mathrm{H}_2. \tag{5.2}$$

Such proton abstraction reactions have relatively large rate constants ranging from 3.1×10^{-9} to 11×10^{-9} cm^3 s^{-1}. Similarly, reaction efficiencies are generally higher than other reactions in this study.

Mackay et al. [10] measured the rate constant for the proton transfer reaction of hydride with acetylene with a flowing afterglow instrument in a similar manner as described in Section 5.2 and reported $k = 4.42$ (±25%) $\times 10^{-9}$ cm^3 s^{-1}. In comparison, our measured

rate constant of $k = 3.1 \times 10^{-9}$ cm^3 s^{-1} agrees within the combined error bars.

The reaction of hydride with water is the only reaction in this study for which more than one rate constant measurement has been reported. Betowski et al. [11] determined a rate constant of $k = 3.7\ (\pm 25\%) \times 10^{-9}$ cm^3 s^{-1} for the reaction

$$H^- + H_2O \longrightarrow OH^- + H_2 \tag{5.3}$$

at 298 K using the flowing afterglow technique. Melton & Neece [12] carried out an energy-variable study for this reaction ranging from 0 to 10 eV and reported a value of $k = 3.8\ (\pm 30\%) \times 10^{-9}$ cm^3 s^{-1} at 0 eV. An earlier measurement from Stockdale et al. [13, 28] for the same reaction was reported as $k = 5.4\ (\pm 1.6) \times 10^{-7}$ cm^3 s^{-1}. Rate constants by Stockdale et al. [13, 28] were measured using a pulsed source time-of-flight mass spectrometer, and their reported rate constant measurement at 0 eV ion energy, in the laboratory frame, exceeds the collision rate constant by a factor of 60 and is therefore not physically reasonable. Our determination of this reaction rate constant is $k = 4.8 \times 10^{-9}$ cm^3 s^{-1}. The experimental conditions of our study are most similar to those of Betowski et al. [11] where ions were produced using a similar method (i.e., electron ionization on a precursor) and subsequently thermalized via collisions with carrier gas molecules.

Mackay et al. [14] reported a rate constant of $k = 1.3\ (\pm 25\%) \times 10^{-8}$ cm^3 s^{-1} for the reaction of hydride with CH_3CN. The measurement was made using a flowing afterglow instrument under conditions similar to those described in Section 5.2. Our reported value, $k = 1.1 \times 10^{-8}$ cm^3 s^{-1}, is within the combined error bars of our study and the former measurement. As with the data of Mackay et al. [14], we saw no evidence of nucleophilic displacement,

$$H^- + CH_3CN \nrightarrow CN^- + CH_4. \tag{5.4}$$

Although the reaction enthalpy is -53.0 kcal mol^{-1} for this mechanism, a transition state barrier 15.1 kcal mol^{-1} above the total energy of the reactants inhibits this reaction from occurring in our experiment.

The reactions of H^- with methanol, acetone, and acetaldehyde have not been previously studied. We report a rate constant for the proton transfer reaction of methanol with hydride as $k = 6.1 \times 10^{-9}$ cm^3 s^{-1}. The substitution mechanism for the methanol/hydride reaction producing OH^- and CH_4 is more exothermic (ΔH_{theor} = -37.0 kcal mol^{-1}) than the proton transfer mechanism (ΔH_{theor} = -18.6 kcal mol^{-1}). However, calculations predict a high transition state energy barrier of 13.2 kcal mol^{-1} along the reaction coordinate that effectively prevents this reaction. Our measured rate constants for the reaction of hydride with acetone, $k = 7.0 \times 10^{-9}$ cm^3 s^{-1}, and with acetaldehyde, $k = 6.4 \times 10^{-9}$ cm^3 s^{-1}, indicate rapid reactions.

5.3.2 Atom Abstraction/Addition Reactions

Reaction rate constants and efficiencies for the reactions of H^- with N_2O and CO_2 are markedly different than those of proton transfer reactions (Table 5.1). The reaction coordinate plot of H^- with N_2O is shown in Figure 5.1, with all energies relative to the total energy of the reactants. Attack of H^- on the terminal nitrogen atom can lead to: (1) oxygen atom abstraction with a small transition state barrier 20.6 kcal mol^{-1} below the energy of the reactants and (2) an AD mechanism that is inhibited by a transition state barrier 17.1 kcal mol^{-1} above the energy of the reactants. Similarly, direct attack on the oxygen atom leads to oxygen-atom abstraction. H^- attack at the terminal nitrogen is likely the most dominant mechanism for oxygen-atom abstraction because attack at the oxygen is hindered by a barrier only 0.2 kcal mol^{-1} below the energy of the reactants. Dunkin et al. [15] measured the reactivity of hydride with nitrous oxide and reported a rate constant of $k = 1.1 \times 10^{-9}$ cm^3 s^{-1}, which is in agreement with our measurement of $k = 1.0 \times 10^{-9}$ cm^3 s^{-1}.

For the reaction of H^- with CO_2, four reaction channels were investigated. Figure 5.2a shows the hydrogen atom attacking one of the terminal oxygen atoms of CO_2. The AD and oxygen-atom abstraction channels that would result from this attack are hampered by

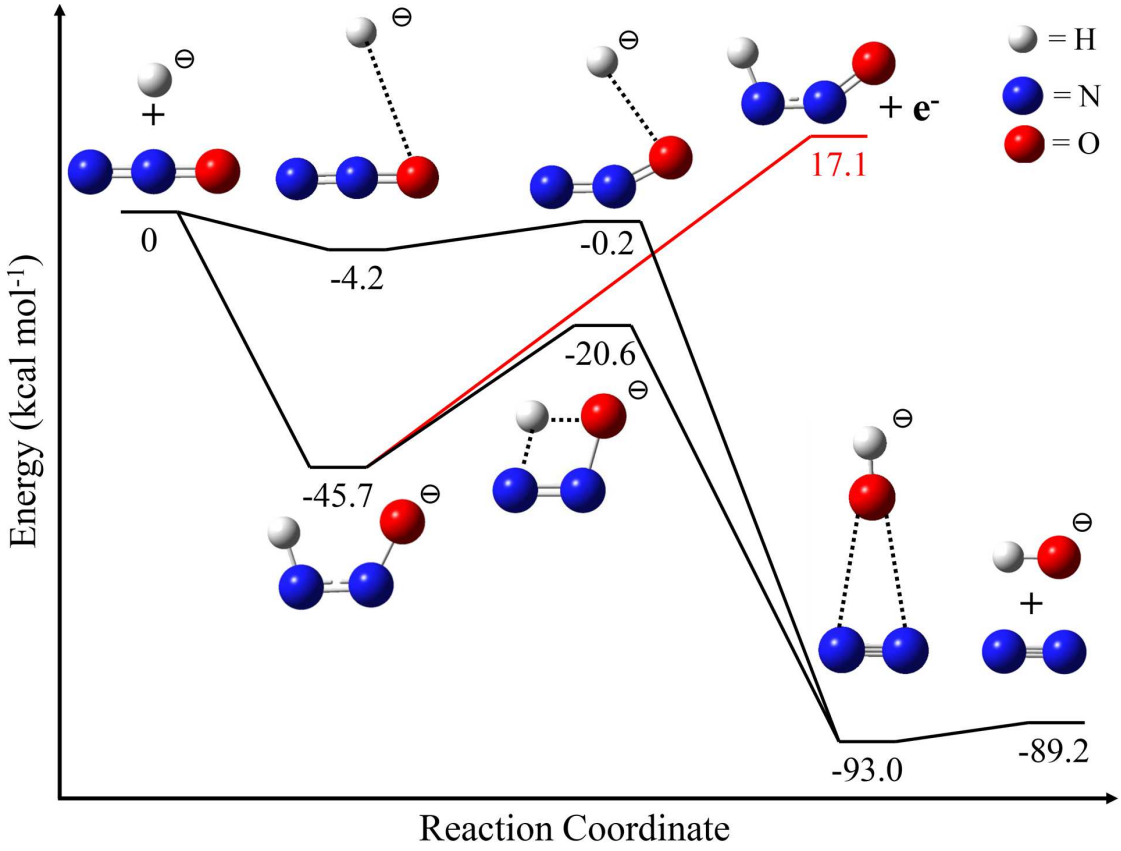

Figure 5.1: $H^- + N_2O$ reaction coordinate plot. Energetically allowed pathways are traced in black lines and disallowed (endothermic) pathways are traced in red lines. Energies obtained from calculations performed at the MP2(full)/aug-cc-pVDZ level of theory.

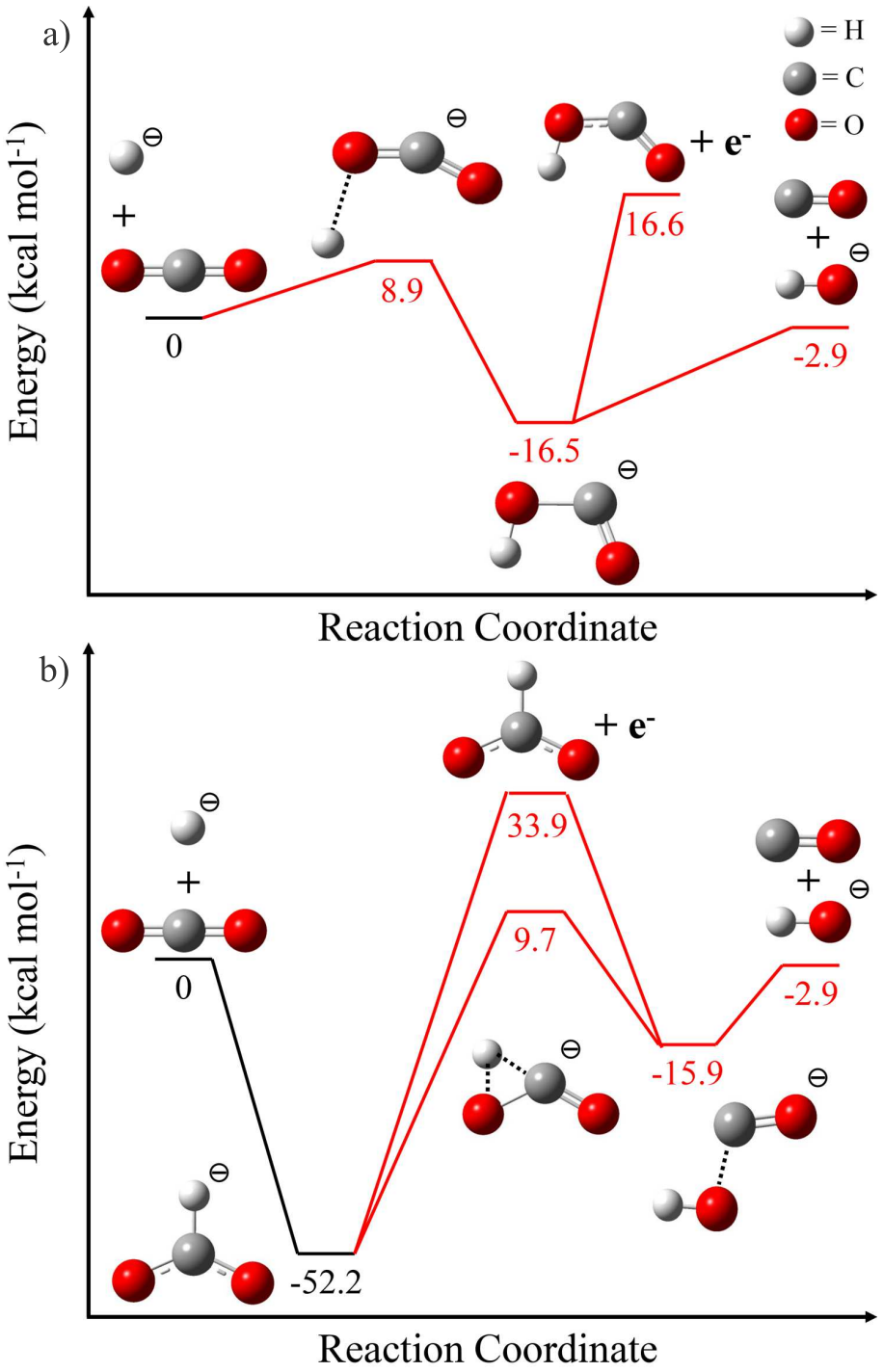

Figure 5.2: H^- + CO_2 reaction coordinate plots. (a) Reaction with attack at an oxygen atom. (b) Reaction with attack at carbon. Energetically allowed pathways are traced in black lines and disallowed (endothermic) pathways are traced in red lines. Energies obtained from calculations performed at the MP2(full)/aug-cc-pVDZ level of theory.

a transition state 8.9 kcal mol^{-1} above the energy of the reactants. Alternately, Figure 5.2b shows the hydrogen atom attacking the carbon atom of the CO_2. The AD channel producing the neutral association product with the hydrogen bound to the carbon is an endothermic process and does not occur. The atom-transfer reaction forming CO and HO^- from the reactant intermediate has a transition state barrier 9.7 kcal mol^{-1} higher in energy than the reactants and also does not occur. Reaction of H^- with CO_2 is slow. Our measured effective two-body rate constant for association is $k = 0.09 \times 10^{-9}$ cm^3 s^{-1}. The HCO_2^- ion is small and will likely not survive long enough to undergo radiative stabilization in the ISM.

5.3.3 Associative Detachment Reactions

Hydride reacts with molecular oxygen (O_2) and carbon monoxide (CO) via AD reactions. Similar to the proton transfer reactions discussed previously, these reactions proceed without barriers along the approach of reactants. A large difference is evident, however, when we compare efficiencies and rate constants for these reactions. The differences are attributed to relative enthalpies. The AD channel for the O_2 reaction is exothermic (ΔH_{exp} = -34.2 kcal mol^{-1}), whereas the CO reaction is essentially thermoneutral (ΔH_{exp} = 2.1 kcal mol^{-1}). This difference in enthalpy is also reflected in the measured rate constants, where the reaction with O_2 is approximately two orders of magnitude more efficient compared to reaction with CO.

In clarifying the electron affinity of O_2, Dunkin et al. [15] measured a rate constant of $k = 1.2$ ($\pm$20%) $\times 10^{-9}$ cm^3 s^{-1} for the $H^- + O_2$ reaction. They considered all possible formation products: $O_2^- + H$, $OH^- + O$, and $O^- + OH$. Hydroxide formation is plausible since this reaction is exothermic by 8.6 kcal mol^{-1}. O^- formation, however, is thermoneutral (0.4 kcal mol^{-1}) and cannot compete with the AD channel. Charge transfer is endothermic by 7.0 kcal mol^{-1} and should therefore not occur. A careful experimental search by Dunkin et al. [15] for these alternative products turned out negative. Similarly, our studies show clear evidence of the AD channel. However, the presence of background OH^- in our spectra

prevents quantitative branching ratio determination for relatively minor ionic products. Our measured rate constant of $k = 1.4 \times 10^{-9}$ cm^3 s^{-1} for the AD reaction is in good agreement with the previously published value.

5.3.4 S_N2/E2 Reactions

Hydride reactivity with methyl chloride proceeds via a substitution mechanism, and reaction with *tert*-butyl chloride proceeds via an elimination mechanism. The lower reaction efficiencies relative to the proton transfer reactions discussed earlier are due to transition states along the reaction coordinates that are near the energy of the reactants. The reaction coordinate plot for H^- + CH_3Cl is shown in Figure 5.3. Here, we consider proton abstraction and substitution channels for the methyl chloride reaction. While both channels have transition state barriers, the substitution channel has a lower barrier and is more exothermic overall (ΔH_{theor} = -91.5 kcal mol^{-1} for the substitution compared to -4.8 kcal mol^{-1} for the proton abstraction). Additionally, we saw no evidence of the weakly bound CH_3 anion.

Similarly, we considered a substitution mechanism for the *tert*-butyl chloride reaction. We cannot distinguish between competing mechanisms for this reaction since Cl^- is produced by both processes. However, theoretical calculations predict the substitution reaction to have a higher transition state barrier than the elimination reaction (ΔH_{theor} = 10.7 kcal mol^{-1} versus -8.4 kcal mol^{-1}). Therefore, only elimination occurs in this reaction.

Prior measurement of the rate constant for the methyl chloride reaction was reported as $k = 3.0$ ($\pm$20%) $\times 10^{-9}$ cm^3 s^{-1} by Tanaka et al. [16]. Our determination for the methyl chloride S_N2 reaction is $k = 2.5 \times 10^{-9}$ cm^3 s^{-1} and $k = 4.0 \times 10^{-9}$ cm^3 s^{-1} for the *tert*-butyl chloride E2 reaction.

5.3.5 Neutral Molecules Showing No Reaction

Some reactions in this study exhibited little or no reactivity. We saw no significant decrease of reactant ion or formation of product ions in the reaction of hydride with D_2,

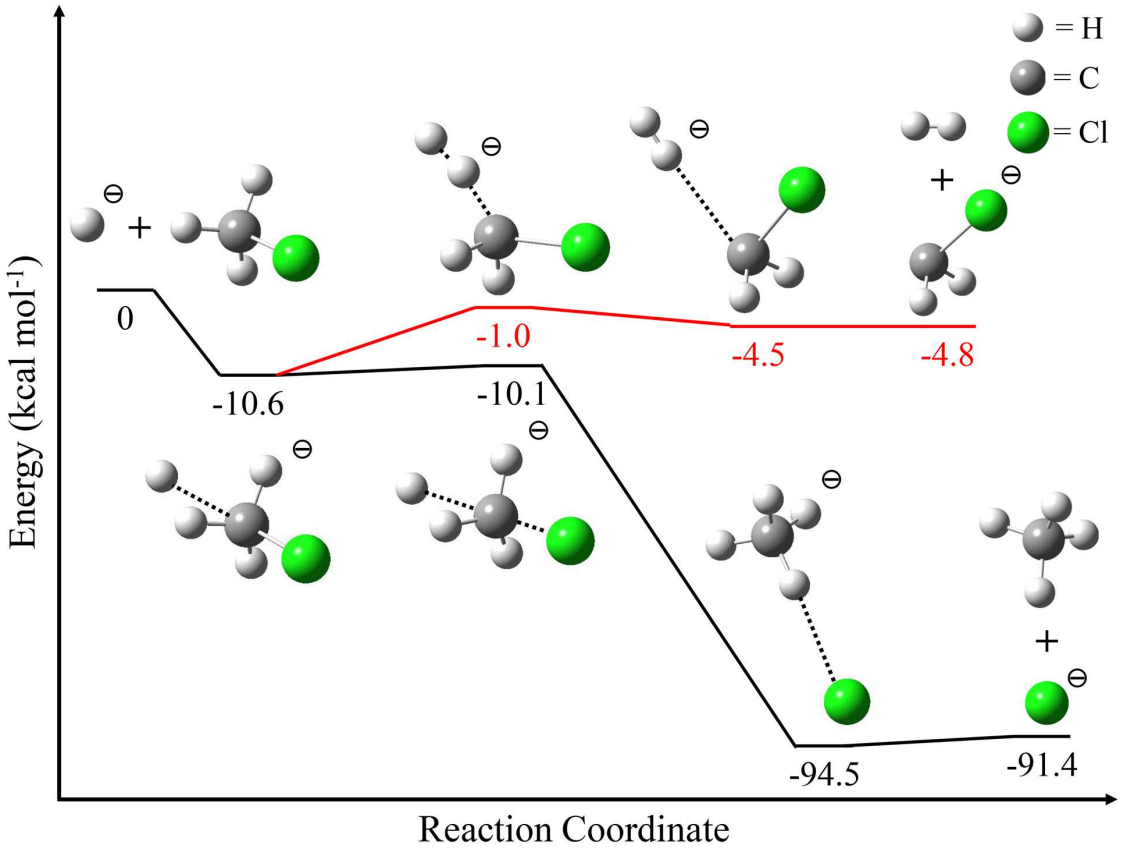

Figure 5.3: H^- + CH_3Cl reaction coordinate plot. An energetically allowed pathway is traced in black lines. The pathway traced in red, although energetically allowed, does not occur. Energies obtained from calculations performed at the MP2(full)/aug-cc-pVDZ level of theory.

$(CH_3CH_2)_2O$, and c-C_6H_6. We observe only slight falloff in hydride signal intensity with the addition of D_2 up to a neutral molecule density of $\sim 2 \times 10^{12}$ cm^{-3}. Based on our observation, we set an upper limit for the reaction rate constant as $k < 1 \times 10^{-11}$ cm^3 s^{-1}. However, our observations do show D^- production as H^- is depleted.

Typically, strong bases have been found to react prominently with ethers by elimination mechanisms [29]. However, calculations suggest that the elimination channel for the reaction of H^- with diethyl ether does not occur due to a barrier along the reaction coordinate that is 5.4 kcal mol^{-1} higher in energy than the reactants.

In reacting hydride with benzene, we noted a decrease in signal and made several attempts to measure a rate constant. In 14 attempts over the course of three days using two different high-purity benzene samples, we were left with a rate constant with an unreasonably low precision [2 ($\pm$2) $\times 10^{-11}$ cm^3 s^{-1}]. Experimental and calculated enthalpies suggest that the reaction is thermoneutral, a possible cause of the problem. The presence of a relatively stable adduct could account for a slight decrease in the reactant ion signal. Bohme & Young [17] studied the reaction of hydride with benzene in a series of bracketing experiments to determine electron affinities from thermal proton transfer reactions. Their study was performed using a flowing afterglow instrument, and generated H^- via electron ionization on NH_3 in helium as well. Their rate determination resulted only in limiting value, $k \gtrsim 5 \times 10^{-11}$ cm^3 s^{-1}.

5.4 Conclusion

Table 5.1 is a compilation of our results which provide an increase in the accuracy of existing rate constants and a contribution of several new rate constants. This study represents a chemical mapping of hydride reactivity with neutral species, many of which have been detected in the ISM. Experimental observations and contributions from ab initio calculations have accounted for a variety of reaction mechanisms and a range of reaction efficiencies.

5.5 References

1. Glover, S. C.; Savin, D. W.; Jappson, A.-K., Cosmological Implications of the Uncertainty in H^- Destruction Rate Coefficients. *Astrophys. J.* **2006**, *640*, 553.

2. Ross, T.; Baker, E. J.; Snow, T. P.; Destree, J. D.; Rachford, B. L.; Drosback, M. M.; Jensen, A. G., The Search for H^- in Astrophysical Environments *Astrophys. J.* **2008**, *684*, 358.

3. Wildt, R., Negative Ions of Hydrogen and the Opacity of Stellar Atmospheres. *Astrophys. J.* **1939**, *90*, 611.

4. Chandrasekhar, S., Some Remarks on the Negative Hydrogen Ion and its Absorption Coefficient. *Astrophys. J.* **1944**, *100*, 176.

5. Münch, D., A Theoretical Discussion of the Continuous Spectrum of the Sun. *Astrophys. J.* **1945**, 102, 385.

6. Chandrasekhar, S.; Breen, F. H., On the Continuous Absorption Coefficient of the Negative Hydrogen Ion. III. *Astrophys. J.* **1946**, *104*, 430.

7. Black, J. H., Molecules in Planetary Nebulae. *Astrophys. J.* **1978**, *222*, 125.

8. Field, D., H_2 Formation in Space: A Negative Ion Route? *Astron. Astrophys.* **2000**, *362*, 774.

9. Woon, D. E. The Astrochymist. http://astrochymist.com (accessed July 11, 2014).

10. Mackay, G. I.; Tanaka, K.; Bohme, D. K., Rate Constants at 297 K for Proton Transfer Reactions with C_2H_2: An Assessment of the Average Quadrupole Orientation Theory. *Int. J. Mass Spectrom. Ion Process.* **1977**, *24*, 125.

11. Betowski, D.; Payzant, J. D.; Mackay, G. I.; Bohme, D. K., Rate Coefficients at 297 K for Proton Transfer Reactions with H_2O. Comparisons with Classical Theories and Exothermicity. *Chem. Phys. Lett.* **1975**, *31*, 321.

12. Melton, C. E.; Neece, G. A., Rate Constants and Cross Sections for the Production of OH^- from O^- and H^- in Water. *J. Am. Chem. Soc.* **1971**, *93*, 6757.

13. Stockdale, J. A. D.; Compton, R. N.; Reinhardt, P. W., Studies of Negative-Ion-Molecule Reactions in the Energy Region from 0 to 3 eV. *Phys. Rev.* **1969**, *184*, 81.

14. Mackay, G. I.; Betowski, L. D.; Payzant, J. D.; Schiff, H. I.; Bohme, D. K., Rate Constants at 297 K for Proton Transfer Reactions with Hydrocyanic Acid and Acetonitrile. Comparisons with Classical Theories and Exothermicity. *J. Phys. Chem.* **1976**, *80*, 2919.

15. Dunkin, D. B.; Fehsenfeld, F. C.; Ferguson, E. E., Rate Constants for the Thermal Energy Reactions of H^- with O_2, NO, CO, and N_2O. *J. Chem. Phys.* **1970**, *53*, 987.

16. Tanaka, K.; Mackay, G. I.; Payzant, J. D.; Bohme, D. K., Gas-Phase Reactions of Anions with Halogenated Methanes at 297 K. *Can. J. Chem.* **1976**, *54*, 1643.

17. Bohme, D. K.; Young, L. B., Electron Affinities from Thermal Proton Transfer Reactions: C_6H_5 and $C_6H_5CH_2$. *Can. J. Chem.* **1971**, *49*, 2918.

18. Martinez, O., Jr.; Yang, Z.; Betts, N. B.; Snow, T. P.; Bierbaum, V. M., Experimental Determination of the Rate Constant for the Associative Detachment Reaction $H^- + H \longrightarrow H_2 + e^-$ at 300 K. *Astrophys. J.* **2009**, *705*, L172.

19. Bierbaum, V. M., Flow Tubes. In *Encyclopedia of Mass Spectrometry*, Armentrout, P. B., Ed.; Elsevier: Amsterdam, 2003; p 940.

20. Frisch, M. J.; Trucks, G. W.; Schlegel, H. B.; Scuseria, G. E.; Robb, M. A.; Cheeseman, J. R.; Scalmani, G.; Barone, V.; Mennucci, B.; Petersson, G. A. et al. *Gaussian 09*, Revision D.01; Gaussian Inc.: Wallingford, CT, 2009.

21. Bartlett, R. J.; Musiał, M., Coupled-Cluster Theory in Quantum Chemistry. *Rev. Modern Phys.* **2007**, *79*, 291.

22. Dunning, T. H., Jr., Gaussian Basis Sets for Use in Correlated Molecular Calculations. I. The Atoms Boron Through Neon and Hydrogen. *J. Chem. Phys.* **1989**, *90*, 1007.

23. Møller, C.; Plesset, M. S., Note on an Approximation Treatment for Many-Electron Systems. *Phys. Rev.* **1934**, *46*, 618.

24. Gioumousis, G.; Stevenson, D. P., Reactions of Gaseous Molecule Ions with Gaseous Molecules. V. Theory. *J. Chem. Phys.* **1958**, *29*, 294.

25. Su, T.; Chesnavich, W. J., Parametrization of the Ion-Polar Molecule Collision Rate Constant by Trajectory Calculations. *J. Chem. Phys.* **1982**, *76*, 5183.

26. Lide, D. R., Ed., *CRC Handbook of Chemistry and Physics*, 89th ed.; CRC Press: Boca Raton, FL, 2008.

27. Linstrom, P. J.; Mallard, W. G., Eds., In *NIST Chemistry WebBook, NIST Standard Reference Database Number 69*; NIST: Gaithersburg, MD, 2014.

28. Stockdale, J. A. D.; Compton, R. N.; Reinhardt, P. W., Measurement of the Cross Section for the Reactions $H^- + H_2O \longrightarrow OH^- + H_2$ and $D^- + D_2O \longrightarrow OD^- + D_2$ at Incident Ion Energies near 2 eV. *Phys. Rev. Lett.* **1968**, *21*, 664.

29. DePuy, C. H.; Bierbaum, V. M., Gas-Phase Elimination Reactions of Ethers Induced by Amide and Hydroxide Ions. *J. Am. Chem. Soc.* **1981**, *103*, 5034.

Chapter 6

Gas-Phase Reactions of Polycyclic Aromatic Hydrocarbon Anions with Molecules of Interstellar Relevance

6.1 Introduction

The detection of benzene in the circumstellar medium (CSM) of the preplanetary nebula CRL 618 provided the first evidence that aromatic species exist in space [1]. Although benzene is not a polycyclic aromatic hydrocarbon (PAH), it represents the building block for these compounds. Therefore, its chemistry is prototypical of aromatic molecules and we have included benzene in this study. Although no specific PAHs have been identified in the interstellar medium (ISM), the inclusion of PAHs in astrophysical models has dramatic consequences. Previous models that have included PAH neutrals and anions show significant effects in the chemistry of interstellar clouds. In dense clouds, free electrons are replaced by negative PAHs, which become the dominant carriers of negative charge [2, 3]. The fraction of ionized atomic species is also reduced in the presence of PAHs in diffuse and dense clouds because of the increased recombination rate between atomic positive ions and PAH anions as compared to atomic positive ion-electron recombination [3, 4].

Small PAHs and their derivatives are also proposed to exist in the CSM. In particular, deprotonated PAH anions may be found in dense regions where these molecules can be shielded from photodissociation and photoionization [5]. Many formation mechanisms for benzene have been proposed. The formation of the phenyl radical is included in both the radical-based reaction scheme [6] and the ion-based reaction scheme [7] for benzene chem-

istry in protoplanetary nebulae [8]. In addition, a formation route for the naphthyl radical has been proposed [6, 9]. Subsequently, dehydrogenated PAH radicals can combine with low-energy free electrons to form dehydrogenated PAH anions [5]. Through these reaction mechanisms, the phenyl radical and phenide anion may coexist with benzene and its neutral and anionic derivatives [5, 8, 10, 11].

However, models that include PAHs neglect to include the dehydrogenated neutral and anionic PAHs. The dehydrogenated PAH anions may be more stable in the ISM and CSM because of the larger electron affinity (EA) of the PAH radicals ($>$ 1 eV) as compared to the parent PAHs (0.5–1 eV; [12, 13]). Because of the large difference in EA, we suggest that astrophysical models should include not only anions of the PAH parent molecules but also the dehydrogenated PAH anion counterparts. The structures of the neutral and most stable anionic dehydrogenated PAH molecules are shown in Figure 6.1.

6.2 Methods

Reaction rate constants of anion-neutral reactions are measured using a flowing afterglow-selected ion flow tube (FA-SIFT) instrument. Reactions of small dehydrogenated PAH anions with H atoms and neutral molecules of interstellar relevance are investigated. The experimental reactions are further supported by ab initio calculations.

6.2.1 Experimental Methods

The experiments are carried out using an FA-SIFT apparatus. In this work, amide (NH_2^-) is generated using electron ionization (70 eV ionization energy) of ammonia gas (NH_3; 99.9995%) in a helium buffer gas. The dehydrogenated PAH anions are produced in the source flow tube by the proton abstraction reaction of the neutral aromatic molecule with amide,

$$NH_2^- + R\text{–}H \longrightarrow R^- + NH_3. \tag{6.1}$$

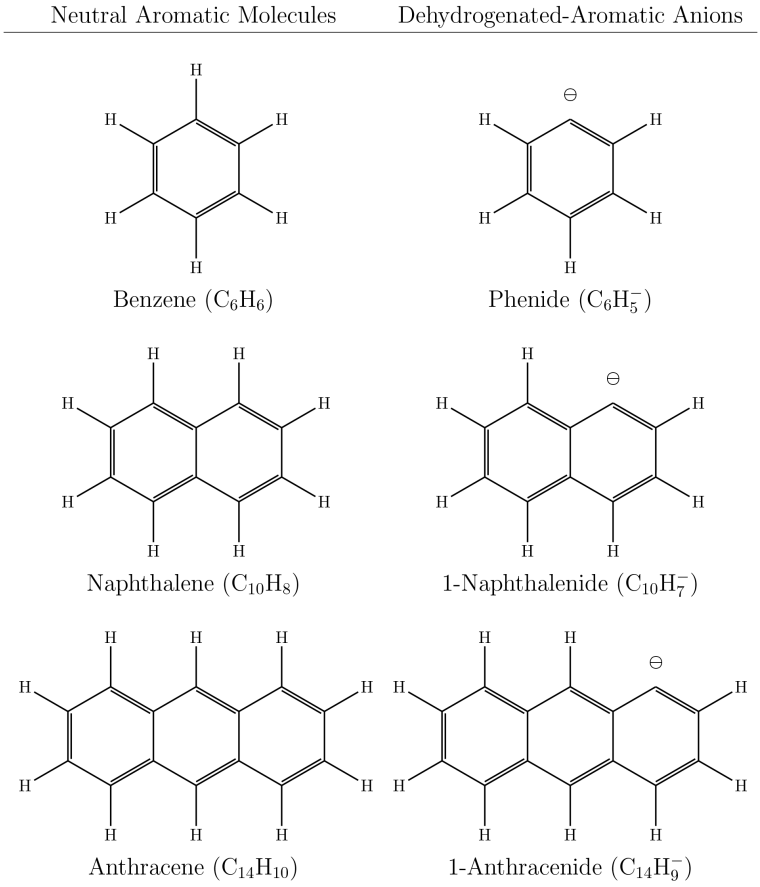

Figure 6.1: Name, chemical formula, and structure of the neutral aromatic molecules and their corresponding dehydrogenated-aromatic anion. The anions shown are the lowest energy isomers (MP2(full)/aug-cc-pVDZ level of theory).

The ions generated are sampled into the low-pressure ion selection region and mass selected using a quadrupole mass filter. Ions of a single mass-to-charge ratio are then injected into the reaction flow tube, entrained in a flow of helium carrier gas, and collisionally cooled before the introduction of neutral reactants. Molecular reactants of known concentration are added to the reaction flow tube through a manifold of inlets. Reactant ions are sampled through a small orifice into the detection chamber and the decrease in the reactant ion signal is monitored as a function of reaction distance using a quadrupole mass filter coupled to an electron multiplier.

Alternatively, atomic hydrogen is introduced into the reaction flow tube at a fixed reaction distance and the kinetics are monitored as a function of neutral concentration. Hydrogen atoms are generated by thermal dissociation of hydrogen gas on a hot tungsten filament. The reactant ion signal is monitored as a function of filament voltage, which is directly correlated to the concentration of atomic hydrogen [14]. Hydrogen atom concentration is determined with the well-known rate constant for the calibration reaction

$$Cl^- + H \longrightarrow HCl + e^-, \tag{6.2}$$

with a value of $k = 9.6 \times 10^{-10}$ cm^3 s^{-1} [15]. The reactant ion signal is monitored as a function of reaction distance or filament voltage. Rate constants are derived using pseudo first order kinetics [16].

Product branching fractions were determined for reaction of $C_6H_5^-$ with N_2O. The ratio of the individual product ion versus the total product ion intensity is plotted versus (1) reaction distance or (2) fraction of parent ion remaining. Primary product distributions are determined by extrapolating the data to (1) zero reaction distance or (2) zero reaction of parent ion. These values are combined and an average product distribution is reported.

The neutral reagents included in this study are as follows: hydrogen (H_2; 99.999% with the gas further purified by passage through a molecular sieve trap immersed in liquid nitrogen), deuterium (D_2; 99.8% with the gas further purified by passage through a molecular sieve

trap immersed in liquid nitrogen), carbon monoxide (CO; 99.5%), oxygen (O_2; 99.994%), carbon dioxide (CO_2; 99%), nitrous oxide (N_2O; 99.0%), acetylene (C_2H_2; 99.6%), methanol (CH_3OH; 99.9%), acetonitrile (CH_3CN; 99.8%), acetone [$(CH_3)_2CO$; 99.5%], acetaldehyde (CH_3CHO; 99.5%), methyl chloride (CH_3Cl; 99.5%), and diethyl ether [$(CH_3CH_2)_2O$; 99.9%].

6.2.2 Computational Methods

We have carried out ab initio calculations to support experimental studies. We computed energies and structures for reactants, products, and intermediates involved in the reactions using *Gaussian 03* [17] and *Gaussian 09* [18]. The CCSD(T)/aug-cc-pVDZ level of theory is used for open-shell species such as molecular oxygen to minimize spin contamination on the energetics [19, 20]. Alternatively, all other calculations are carried out at the MP2(full)/aug-cc-pVDZ level of theory [21]. Reaction enthalpies are determined at 298 K using theoretically calculated energies. All rate constants are measured at 298 K. However, the temperatures in dense molecular clouds are much lower [22], and the temperatures of circumstellar environments cover a large range [23]; we present here the first experimental data for these reactions. A variable temperature study would be valuable; however, for reactions with no barrier there is often minimal dependence on temperature. The potential energy surface for the reaction of $C_6H_5^-$ with O_2 has been explored, Subsection 6.3.2.

6.3 Results and Discussion

The reactions of phenide with neutral molecules are divided into four different categories based on reaction mechanisms: proton abstraction, atom abstraction/association, nucleophilic substitution (S_N2), and no reaction. Reactions of dehydrogenated PAH anions with H atoms showed a decrease in reaction efficiency with increasing size of the PAH while reactions with H_2 and D_2 did not occur at a measurable rate.

Table 6.1: $C_6H_5^-$ + neutral molecule reactions

Neutral Reactant	Products	k_{exp}[a] (10^{-10} cm^3 s^{-1})	Efficiency	ΔH_{exp}[c]	$\Delta H_{theor(298\ K)}$[d]
			k_{exp}/k_{col}	(kcal mol^{-1})	(kcal mol^{-1})
Proton Abstraction Reactions					
C_2H_2	$C_6H_6 + C_2H^-$	10.8	1.1[e]	-22.7	-23.3
CH_3OH	$C_6H_6 + CH_3O^-$	18.0	0.92	-19.6	-19.0
CH_3CN	$C_6H_6 + CH_2CN^-$	28.0	0.78	-28.8	-24.6
$(CH_3)_2CO$	$C_6H_6 + CH_3COCH_2^-$	19.1	0.74	-32.9	-31.0
CH_3CHO	$C_6H_6 + CH_2CHO^-$	17.0	0.68	-35.6	-33.5
Atom Abstraction/Association Reactions					
CO_2	$C_6H_5CO_2^-$	6.2	0.83	-56.9	-58.2
O_2	$C_6H_5O^- + O$	0.08	0.01	-32.1	-37.9
N_2O	56% $C_6H_5O^- + N_2$	0.36	0.04	-110	-111
	44% $C_6H_5N_2O^-$			N/A	-45.8
Nucleophilic Substitution (S_N2)					
CH_3Cl	$C_6H_5CH_3 + Cl^-$	6.8	0.36	-76.4	-82.2

Notes. N/A indicates insufficient experimental data to calculate value. No measurable rate constants were obtained for reactions with CO, $(CH_3CH_2)_2O$ and we report a conservative upper limit for the rate constants of $k \leq 1 \times 10^{-12}$ cm^3 s^{-1}.

[a] The experimental precision, reported as 1σ of the mean, is $\pm 10\%$ and there is a total error of $\pm 20\%$ for the reported rate constants.

[b] k_{col} is determined according to Langevin theory [24] for reactions involving neutral species having no dipole moment and parameterized trajectory theory [25] for those reactions involving neutral species with dipole moments.

[c] Values determined using additivity methods with experimental values for ionization energies, bond energies, electron affinities, and heats of formation [12, 26].

[d] MP2(full)/aug-cc-pVDZ and CCSD(T)/aug-cc-pVDZ theory level including zero-point and thermal energy corrections at 298 K.

[e] The reaction efficiency using Langevin collision rate theory to calculate the collision rate is 1.1 [24]. The reaction efficiency using the point polarizable ion-collision model is 0.98 [28].

6.3.1 Reactions of Phenide with Neutral Molecules

The reactions of phenide with neutral molecules are summarized in Table 6.1; this table includes reaction rate constants, collision rate constants, reaction efficiencies, and enthalpies of reaction. The experimental precision, reported as 1σ of the mean, is $\pm 10\%$ for all reactions and there is a total error of $\pm 20\%$ for the reported rate constants. For comparison, we report reaction efficiencies as $k_{\text{exp}}/k_{\text{col}}$, where k_{col} is the collision rate constant determined by Langevin theory [24] for neutral reactants without a permanent dipole moment (CO_2, O_2, and C_2H_2) and by parameterized trajectory theory [25] for molecules that possess a permanent dipole moment (CO, N_2O, CH_3OH, CH_3CN, $(CH_3)_2CO$, CH_3CHO, CH_3Cl, and $(CH_3CH_2)_2O$) [26]. We determine experimental enthalpies of reaction, ΔH_{exp}, using Hess's law with bond dissociation energies, ionization energies, electron affinities, and other enthalpies of reaction taken from the NIST Chemistry WebBook, NIST Standard Reference Database Number 69 [12], or from the 89th edition of the CRC Handbook of Chemistry and Physics [26]. For comparison, we also determine enthalpies of reaction at 298 K using ab initio calculations. We then determine theoretical enthalpies of reaction using the calculated energies. The FA-SIFT instrument is only able to detect ionic products; however, experimental and calculated enthalpies of reaction aid in determining the neutral counterpart. The mechanisms observed for the reactions studied include proton abstraction reactions, atom-abstraction or association reactions, a nucleophilic substitution reaction (S_N2), and a last category where no reactions are observed. For discussion, we use these reaction mechanisms to divide the neutral reactant molecules into four different categories.

6.3.1.1 Proton Abstraction Reactions

Neutral reactants C_2H_2, CH_3OH, CH_3CN, $(CH_3)_2CO$, and CH_3CHO are observed to react with phenide via proton abstraction:

$$C_6H_5^- + R\text{–}H \longrightarrow R^- + C_6H_6. \tag{6.3}$$

The reactions of phenide with CH_3OH and $(CH_3)_2CO$ were previously studied by Bieńkowski & Danikiewicz [27]; however, reaction rate constants were not measured. The deprotonated R^- was the only ionic product observed by Bieńkowski & Danikiewicz [27], which is consistent with our results.

These proton abstraction reactions are barrierless processes resulting in large rate constants, which range from 1.08×10^{-9} to 2.80×10^{-9} cm^3 s^{-1}. The reaction efficiencies vary from 0.68 to 1.1. However, the reaction efficiencies do not directly correlate with exothermicity, suggesting that there are minor dynamical effects in the reaction pathways studied. The reaction efficiency for C_2H_2, using Langevin theory [24] to calculate the collision rate constant, is greater than unity. However, if the collision rate constant is calculated using a more current theory, such as the point polarizable ion (PPI) model [28], the reaction efficiency is 0.98. A more advanced model may be needed to better understand the reaction dynamics for these two species; however, the result remains that this reaction is highly efficient.

6.3.1.2 Atom-Abstraction/Association Reactions

The association product observed in our experiment for the reaction of phenide with CO_2 is consistent with the results of Bierbaum et al. [29], Bieńkowski & Danikiewicz [27], and others (see Bieńkowski & Danikiewicz [27] for further references). However, reaction rate constants have not been previously reported. Gas-phase reactions of carbanions, such as phenide, with CO_2 are known to yield association products:

$$R^- + CO_2 \longrightarrow RCOO^-. \tag{6.4}$$

These reactions occur by a barrierless pathway and proceed with high efficiency. This effect can be seen by the large rate constant and reaction efficiency for the reaction of phenide with CO_2 as compared to the association pathway for the reaction of phenide with N_2O. The reaction rate constant listed in Table 6.1 for the reaction of phenide with CO_2 is an

effective two-body rate constant. The three-body rate constants and lower limit of the association rate constant can be determined using the method described in Section 2.8.

Alternatively, the reaction of phenide with O_2 proceeds through an atom-abstraction mechanism,

$$C_6H_5^- + O_2 \longrightarrow C_6H_5O^- + O, \tag{6.5}$$

where $C_6H_5O^-$ is the only detected product. Studies by Wenthold et al. [30], using a flowing afterglow-triple quadrupole apparatuse, detected ionic products of $C_6H_5O^-$, $C_6H_4O_2^-$, and c-$C_5H_5^-$, whereas Bieńkowski & Danikiewicz [27] reported ionic products $C_6H_5O^-$, $C_6H_4O_2^-$, and O_2^-. However, no experimental rate constants were reported. In our experiments, all ionic and neutral reactants are collisionally cooled to their vibrational ground state by the helium buffer gas; thus, O_2 is in the triplet state and phenide is in the singlet state. The reaction pathways to yield the products $C_6H_4O_2^-$ + H and c-$C_5H_5^-$ + CO_2 require spin conversion, which is quantum mechanically forbidden, indicating that the production of these ions is likely inefficient. In addition, electron transfer from phenide (EA = 1.15 eV; [31]) to O_2 (EA = 0.45 eV; [32]) is not energetically allowed. The theoretical reaction coordinate plot for the reaction of phenide with O_2 is shown in Figure 6.2. The reaction proceeds through a lower energy complex (-30.1 kcal mol^{-1}) to the first transition state that is almost thermoneutral (-3.2 kcal mol^{-1}). The low reaction rate constant and low reaction efficiency observed may be due to the relatively high barrier. After the first transition state, the reaction progresses to a second low energy complex (-34.9 kcal mol^{-1}), toward a second transition state (-23.7 kcal mol^{-1}), and onto the products with an overall reaction enthalpy of -37.8 kcal mol^{-1}. c-$C_6H_5O^-$ and O atom are the resulting products because the formation of ring-opened structures is not energetically allowed.

Unlike CO_2 and O_2, the reaction of phenide with N_2O proceeds through two reaction pathways: association and atom abstraction. This reaction was observed by Bierbaum et al. [29], Kass et al. [33], and Wenthold et al. [30], who also noted that the atom abstrac-

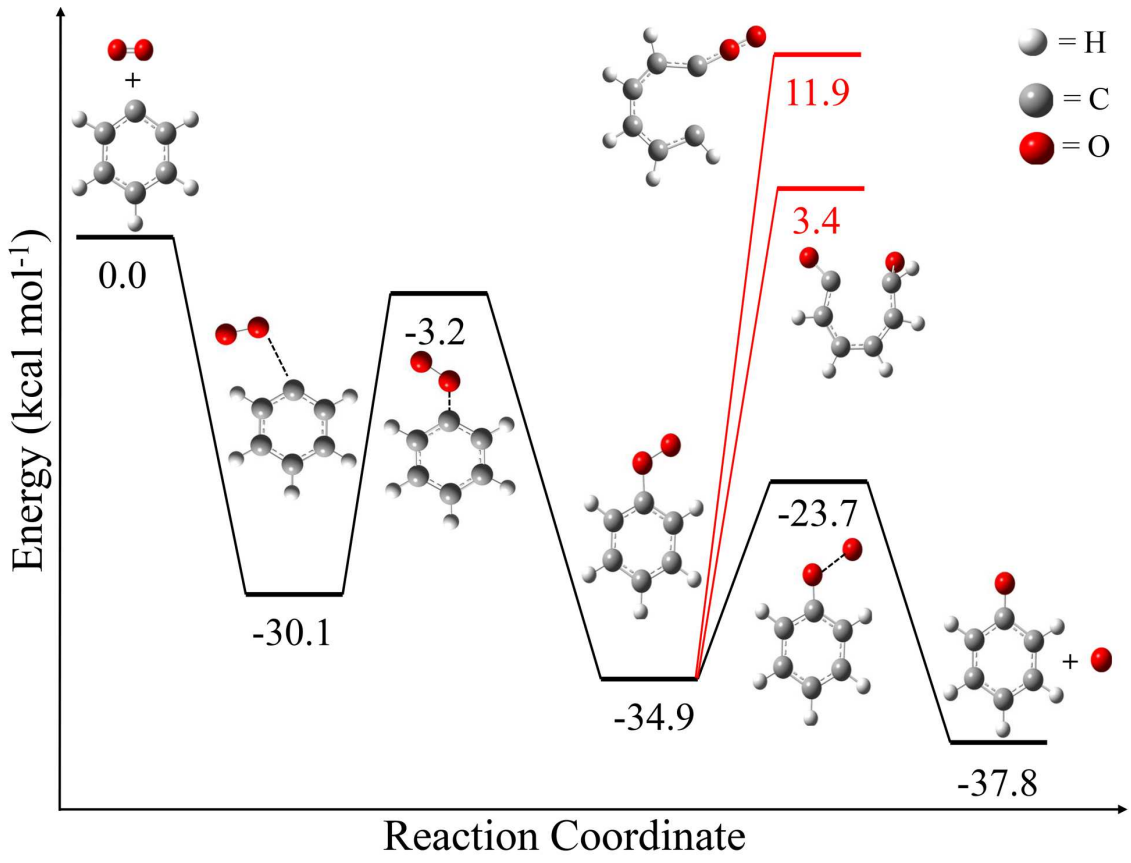

Figure 6.2: $C_6H_5^- + O_2$ reaction coordinate plot. The black lines indicate the energetically allowed pathways. The red lines indicate endothermic reaction pathways. Energies were obtained from ab initio calculations performed at the CCSD(T)/aug-cc-pVDZ level of theory (kcal mol^{-1}).

tion reaction was the dominant mechanism. However, no experimental rate constants were reported. The complete reaction coordinate path has been mapped by Liang et al. [34] at the MP2/6-31++G(d, p) level of theory. The association product observed experimentally is most likely a stable intermediate along one of the two lower energy pathways toward the atom abstraction products. This association product is formed through a three-body collision in the reaction flow tube. Although three-body reactions are unlikely in the ISM and CSM, the large number of degrees of freedom in large PAHs (> 30 carbon atoms) may be sufficient to allow stabilization through radiative emission.

6.3.1.3 Nucleophilic Substitution (S_N2) Reactions

The reaction of phenide with CH_3Cl is the only system in this study that has a previously reported rate constant. For this reason, we chose to study the reaction of $C_6H_5^-$ + CH_3Cl to validate the accuracy of our measurements. The reaction studied by Bohme & Young [35] was carried out in a flowing afterglow instrument under similar experimental conditions to our current setup. Their measured reaction rate constant of 8.7×10^{-10} cm^3 s^{-1} agrees with our measured value of 6.8×10^{-10} cm^3 s^{-1}, within the error associated with each measurement. The only ionic product observed in both studies was Cl^-. Bohme & Young [35] proposed three different reaction mechanisms; however, Equation 6.6 is the only energetically allowed pathway, with an estimated reaction enthalpy of ΔH_{exp} = -76.4 kcal mol^{-1},

$$C_6H_5^- + CH_3Cl \longrightarrow Cl^- + C_6H_5CH_3. \tag{6.6}$$

The other two proposed mechanisms, which result in Cl^- and multiple neutral products, are substantially endothermic, rendering them inactive in our experimental setup as well as the ISM and CSM.

6.3.1.4 Neutral Molecules Showing No Reaction

Some reactions in this study exhibit no measurable reactivity and we report a conservative upper limit for the rate constants of $k \leq 1 \times 10^{-12}$ cm^3 s^{-1}. The reactions of phenide with CO and $(CH_3CH_2)_2O$ resulted in no measurable decrease in the reactant ion or increase in product ion(s). The addition reaction of $C_6H_5^-$ + CO is exothermic by 13.7 kcal mol^{-1}; however, three-body stabilization is not observed. Strong bases such as phenide predominantly react with ethers by an elimination reaction [36]. Diethyl ether has not been detected in the ISM or CSM; however, the reaction of phenide with diethyl ether was studied to probe the E2 mechanism for aromatic systems. The reaction of $(CH_3CH_2)_2O$ by the E2 mechanism results in energetically favored products, but there is a barrier of 5.0 kcal mol^{-1} above the energy of the reactants along the reaction coordinate that inhibits this reaction.

6.3.2 Reactions of Dehydrogenated Aromatic Anions with H, H_2, and D_2

The results of the reactions of phenide ($C_6H_5^-$), naphthalenide ($C_{10}H_7^-$), and anthracenide ($C_{14}H_9^-$) with atomic hydrogen (H) are summarized in Table 6.2. For these reactions with H atoms, the experimental precision, reported as 1σ of the mean, is better than $\pm 10\%$ for all reactions and there is a total error of $\pm 50\%$ associated with the rate constants. The collision rate constants, k_{col}, for reactions with H atoms are calculated using the PPI model [28]. All other values listed in Table 6.2 are calculated in the same manner as described in Subsection 6.3.1.

The reactions of dehydrogenated aromatic anions with atomic hydrogen are exothermic and proceed purely through an associative detachment pathway:

$$R^- + H \longrightarrow R\text{–}H + e^-. \tag{6.7}$$

Although it is energetically feasible, the association reaction of anthracenide with H atoms to produce the anthracene radical anion ($C_{14}H_{10}^-$) was not observed. This pathway does not compete with the extremely exothermic associative detachment mechanism that can dissi-

Table 6.2: Dehydrogenated aromatic anion/H atom reactions

Ionic Reactant	Products	k_{exp}[a] (10^{-10} cm^3 s^{-1})	k_{col}[b] (10^{-10} cm^3 s^{-1})	Efficiency k_{exp}/k_{col}	ΔH_{exp}[c] (kcal mol^{-1})	ΔH_{theor}[d] (kcal mol^{-1})
$C_6H_5^-$	$C_6H_6 + e^-$	10.1	24.6	0.41	-88.1	-84.3
$C_{10}H_7^-$	$C_{10}H_8 + e^-$	8.6	25.7	0.33	-80.4	-78.5
$C_{14}H_9^-$	$C_{14}H_{10} + e^-$	7.8	26.3	0.30	N/A	-73.8

Notes. N/A indicates insufficient experimental data to calculate value.

[a] The experimental precision, reported as 1σ of the mean, is $\pm 10\%$ for all reactions and there is a total error of $\pm 50\%$.

[b] k_{col} is determined according to the point polarizable-ion model [28].

[c] Values determined using additivity methods with experimental values for ionization energies, bond energies, electron affinities, and heats of formation [12, 26].

[d] MP2(full)/aug-cc-pVDZ theory level including zero-point and thermal energy corrections at 298 K.

pate the internal energy more easily. The reactions with H atoms show a decrease in the rate constant and in reaction efficiency with increasing size of the aromatic compounds (Table 6.2). This trend may be due to the decrease in deprotonation enthalpy of the neutral aromatic compounds with increasing size. Although the deprotonation enthalpy for anthracene is not known experimentally, we report a theoretically calculated value of 391 kcal mol^{-1} for the most stable isomer, 1-anthracenide. The most stable ionic form for all deprotonated PAHs investigated is shown in Figure 6.1. Naphthalene and anthracene have multiple deprotonation sites; however, the energy difference between these different sites is small (< 5 kcal mol^{-1}). Experimental work carried out by Reed & Kass [37] has shown that the hydrogens on naphthalene are indistinguishable by H–D exchange, where every deuterium on $C_{10}D_7^-$ is exchanged for hydrogen. Ervin et al. [38] have shown that this method of preparation of the naphthyl anion produces predominantly 1-naphthalenide, the most stable isomer. However, because of the small energy difference in deprotonation sites and the method of generation of the napthalenide and anthracenide anions, we are unable to determine a ratio of each individual isomer. Therefore, the rate constants reported in Table 6.2 include all isomeric forms.

In contrast to the H atom studies, the reactions of dehydrogenated PAH anions with H_2 and D_2 exhibit no measurable rate constant. This result is consistent with the relative gas-phase acidities (ΔG_{acid}) of H_2, C_6H_6, and $C_{10}H_8$ which are 394.2 $\pm$0.1 [39], 392.4 $\pm$0.4 [40], and 385.6 $\pm$1.4 kcal mol^{-1} [37], respectively. Although the gas-phase acidity of anthracene is not known experimentally, we report a $\Delta G_{\text{acid}} = 381$ kcal mol^{-1} for the most stable isomer (Table 6.2). Therefore, deprotonation reactions of H_2 by the PAH anions are endothermic, and will not occur in our instrument or the ISM and CSM. The same argument can be applied to D_2, where the free energy for heterolytic cleavage is 394.9 $\pm$0.1 kcal mol^{-1} [41].

6.4 Conclusion

Reaction rate constants for small dehydrogenated PAH anions with H atoms and neutral molecules have been measured experimentally. The phenide anion is very basic and will deprotonate many classes of organic molecules. Although the basicity decreases slightly from phenide to naphthalenide to anthracenide, these ions are still more basic than many organic molecules [12]. Under equilibrium conditions and long times, it is possible that molecules with a small ΔG_{acid}, like HCN, would be deprotonated. However, the assumed abundance of PAHs in the ISM is greater than that of the smaller molecular species [3, 42, 43], and we propose that these anionic PAH species may exist in dense regions of the ISM and CSM and should be included in chemical models of these environments. The reactions of O_2 and N_2O resulted in oxygen addition to the phenide anion. However, due to the low reaction efficiency and low abundance of oxygen-containing molecules, this is likely not the major mechanism for addition of oxygen to PAHs. The results listed in Tables 6.1 and 6.2 provide measured rate constants that can be adopted in astrochemical models. Experiments and contributions from ab initio calculations have accounted for a variety of reaction mechanisms and a range of reaction efficiencies.

6.5 References

1. Cernicharo, J.; Heras, A. M.; Tielens, A. G. G. M.; Pardo, J. R.; Herpin, F.; Guélin, M.; Waters, L. B. F. M., Infrared Space Observatory's Discovery of C_4H_2, C_6H_2, and Benzene in CRL 618. *Astrophys. J. Lett.* **2001**, *546*, L123.

2. Lepp, S.; Dalgarno, A., Polycyclic Aromatic Hydrocarbons in Interstellar Chemistry. *Astrophys. J.* **1988**, *324*, 553.

3. Wakelam, V.; Herbst, E., Polycyclic Aromatic Hydrocarbons in Dense Cloud Chemistry. *Astrophys. J.* **2008**, *680*, 371.

4. Lepp, S.; Dalgarno, A.; van Dishoeck, E. F.; Black, J. H., Large Molecules in Diffuse Interstellar Clouds. *Astrophys. J.* **1988**, *329*, 418.

5. Carelli, F.; Sebastianelli, F.; Baccarelli, I.; Gianturco, A., Electron-Driven Reactions in Proto-Planetary Atmospheres: Metastable Anions of Gaseous o-Benzyne. *Astrophys. J.* **2010**, *712*, 445.

6. Frenklach, M.; Feigelson, E. D., Formation of Polycyclic Aromatic Hydrocarbons in Circumstellar Envelopes. *Astrophys. J.* **1989**, *341*, 372.

7. Woods, P. M.; Millar, T. J.; Herbst, E.; Zijlstra, A. A., The Chemistry of Protoplanetary Nebulae. *Astron. Astrophys.* **2003**, *402*, 189.

8. Widicus Weaver, S. L.; Remijan, A. J.; McMahon, R. J.; McCall, B. J., A Search for ortho-Benzyne (o-C_6H_4) in CRL 618. *Astrophys. J.* **2007**, *671*, L153.

9. Cherchneff, I.; Barker, J. R.; Tielens, A. G. G. M., Polycyclic Aromatic Hydrocarbon Formation in Carbon-Rich Stellar Envelopes. *Astrophys. J.* **1992**, *401*, 269.

10. Carelli, F.; Grassi, T.; Gianturco, F. A., Electron Attachment Rates for PAH Anions in the ISM and Dark Molecular Clouds: Dependence on their Chemical Properties. *Astron. Astrophys.* **2013**, *549*, A103.

11. Carelli, F.; Grassi, T.; Sebastianelli, F.; Gianturco, F. A., Electron-Attachment Rates for Carbon-Rich Molecules in Protoplanetary Atmospheres: the Role of Chemical Differences. *Mon. Not. R. Astron. Soc.* **2013**, *428*, 1181.

12. Linstrom, P. J.; Mallard, W. G., Eds., In *NIST Chemistry WebBook, NIST Standard Reference Database Number 69*; NIST: Gaithersburg, MD, 2014.

13. Hammonds, M.; Pathak, A.; Candian, A.; Sarre, P. J., Spectroscopy of Protonated and Deprotonated PAHs. *EAS Pub. Ser.* **2011**, *46*, 373.

14. Trainor, D. W.; Ham, D. O.; Kaufman, F., Gas Phase Recombination of Hydrogen and Deuterium Atoms. *J. Chem. Phys.* **1973**, *58*, 4599.

15. Howard, C. J.; Fehsenfeld, F. C.; McFarland, M., Negative Ion-Molecule Reactions with Atomic Hydrogen in the Gas Phase at 296 K. *J. Chem. Phys.* **1974**, *60*, 5086.

16. Bierbaum, V. M., Flow Tubes. In *Encyclopedia of Mass Spectrometry*, Armentrout, P. B., Ed.; Elsevier: Amsterdam, 2003; p 940.

17. Frisch, M. J.; Trucks, G. W.; Schlegel, H. B.; Scuseria, G. E.; Robb, M. A.; Cheeseman, J. R.; Montgomery, J. A., Jr.; Vreven, T.; Kudin, K. N.; Burant, J. C. et al. *Gaussian 03*, Revision E.01; Gaussian Inc.: Wallingford, CT, 2003.

18. Frisch, M. J.; Trucks, G. W.; Schlegel, H. B.; Scuseria, G. E.; Robb, M. A.; Cheeseman, J. R.; Scalmani, G.; Barone, V.; Mennucci, B.; Petersson, G. A. et al. *Gaussian 09*, Revision D.01; Gaussian Inc.: Wallingford, CT, 2009.

19. Bartlett, R. J.; Musiał, M., Coupled-Cluster Theory in Quantum Chemistry. *Rev. Modern Phys.* **2007**, 79, 291.

20. Dunning, T. H., Jr., Gaussian Basis Sets for Use in Correlated Molecular Calculations. I. The Atoms Boron Through Neon and Hydrogen. *J. Chem. Phys.* **1989**, *90*, 1007.

21. Møller, C.; Plesset, M. S., Note on an Approximation Treatment for Many-Electron Systems. *Phys. Rev.* **1934**, *46*, 618.

22. Snow, T. P.; Bierbaum, V. M., Ion Chemistry in the Interstellar Medium. *Annu. Rev. Anal. Chem.* **2008**, *1*, 229.

23. Cherchneff, I., The Formation of Polycyclic Aromatic Hydrocarbons in Evolved Circumstellar Environments. *EAS Pub. Ser.* **2011**, *46*, 177.

24. Gioumousis, G.; Stevenson, D. P., Reactions of Gaseous Molecule Ions with Gaseous Molecules. V. Theory. *J. Chem. Phys.* **1958**, *29*, 294.

25. Su, T.; Chesnavich, W. J., Parametrization of the Ion-Polar Molecule Collision Rate Constant by Trajectory Calculations. *J. Chem. Phys.* **1982**, *76*, 5183.

26. Lide, D. R., Ed., *CRC Handbook of Chemistry and Physics*, 89th ed.; CRC Press: Boca Raton, FL, 2008.

27. Bieńkowski, T.; Danikiewicz, W., Generation and Reactions of Substituted Phenide Anions in an Electrospray Triple Quadrupole Mass Spectrometer. *Rapid Comm. Mass Spectrom.* **2003**, *17*, 697.

28. Eichelberger, B. R.; Snow, T. P.; Bierbaum, V. M., Collision Rate Constants for Polarizable Ions. *J. Am. Soc. Mass Spectrom.* **2003**, *14*, 501.

29. Bierbaum, V. M.; DePuy, C. H.; Shapiro, R. H., Gas Phase Reactions of Anions with Nitrous Oxide and Carbon Dioxide. *J. Am. Chem. Soc.* **1977**, *99*, 5800.

30. Wenthold, P. G.; Hu, J.; Squires, R. R., Gas-Phase Reactions of the Benzyne Negative Ions. *J. Mass Spectrom.* **1998**, *33*, 796.

31. Gunion, R. F.; Gilles, M. K.; Polak, M. L.; Lineberger, W. C., Ultraviolet Photoelectron Spectroscopy of the Phenide, Benzyl and Phenoxide Anions, with Ab Initio Calculations. *Int. J. Mass Spectrom. Ion Process.* **1992**, *117*, 601.

32. Ervin, K. M.; Anusiewicz, I.; Skurski, P.; Simons, J.; Lineberger, W. C., The Only Stable State of O_2^- Is the X $^2\Pi_g$ Ground State and It (Still!) Has an Adiabatic Electron Detachment Energy of 0.45 eV. *J. Phys. Chem. A* **2003**, *107*, 8521.

33. Kass, S. R.; Filley, J.; Van Doren, J. M.; DePuy, C. H., Nitrous Oxide in Gas-Phase Ion-Molecule Chemistry: A Versatile Reagent for the Determination of Carbanion Structure. *J. Am. Chem. Soc.* **1986**, *108*, 2849.

34. Liang, J.-X.; Geng, Z.-Y.; Wang, Y.-C.; Han, Y.-X.; Yan, P.-J., Theoretical Study on Reaction of $C_6H_5^-$ with N_2O in Gas Phase. *J. Mol. Struct.: THEOCHEM* **2008**, *859*, 79.

35. Bohme, D. K.; Young, L. B., Kinetic Studies of the Reactions of Oxide, Hydroxide, Alkoxide, Phenyl, and Benzylic Anions with Methyl Chloride in the Gas Phase at 22.5°. *J. Am. Chem. Soc.* **1970**, *92*, 7354.

36. DePuy, C. H.; Bierbaum, V. M., Gas-Phase Elimination Reactions of Ethers Induced by Amide and Hydroxide Ions. *J. Am. Chem. Soc.* **1981**, *103*, 5034.

37. Reed, D. R.; Kass, S. R., Experimental Determination of the α and β C–H bond Dissociation Energies in Naphthalene. *J. Mass Spectrom.* **2000**, *35*, 534.

38. Ervin, K. M.; Ramond, T. M.; Davico, G. E.; Schwartz, R. L.; Casey, S. M.; Lineberger, W. C., Naphthyl Radical: Negative Ion Photoelectron Spectroscopy, Franck-Condon Simulation, and Thermochemistry. *J. Phys. Chem. A* **2001**, *105*, 10822.

39. Shiell, R. C.; Hu, X.; Hu, Q. J.; Hepburn, J. W., Threshold Ion-Pair Production Spectroscopy (TIPPS) of H_2 and D_2. *Faraday Discuss.* **2000**, *115*, 331.

40. Davico, G. E.; Bierbaum, V. M.; DePuy, C. H.; Ellison, G. B.; Squires, R. R., The C–H Bond Energy of Benzene. *J. Am. Chem. Soc.* **1995**, *117*, 2590.

41. Lykke, K. R.; Murray, K. K.; Lineberger, W. C., Threshold Photodetachment of H^-. *Phys. Rev. A* **1991**, *43*, 6104.

42. Turner, B. E., A Common Gas-Phase Chemistry for Diffuse, Translucent, and Dense Clouds? *Astrophys. J.* **2000**, *542*, 837.

43. Wakelam, V.; Herbst, E.; Selsis, F., The Effect of Uncertainties on Chemical Models of Dark Clouds. *Astron. Astrophys.* **2006**, *451*, 551.

Chapter 7

Chemistry of $HCNH^+$: Mechanisms, Structures, and Relevance to Titan's Atmosphere

7.1 Introduction

Saturn's moon Titan is of great interest due to its thick atmosphere. The data collected by the Ion and Neutral Mass Spectrometer (INMS) aboard the Cassini spacecraft have provided insight into the rich composition of Titan's ionosphere. Multiple models have been developed, with the aid of the INMS data, to characterize the chemistry and physics; however, the ion-neutral chemistry of Titan is still not completely understood. In particular, several models of Titan's ionosphere have shown an overestimation of the $HCNH^+$ ion [1–3].

In 2012, Westlake et al. [3] suggested that an incomplete chemical network is the main cause for this discrepancy and proposed the addition of four reaction pathways that have not been previously included:

$$HCNH^+ + H_2 \longrightarrow CH_2NH_2{}^+, \tag{7.1}$$

$$HCNH^+ + CH_4 \longrightarrow C_2H_3NH^+ + H_2, \tag{7.2}$$

$$HCNH^+ + C_2H_2 \longrightarrow C_3HNH^+ + H_2, \tag{7.3}$$

$$HCNH^+ + C_2H_4 \longrightarrow C_3H_3NH^+ + H_2. \tag{7.4}$$

The indicated products for Equations 7.1, 7.3, 7.4 were specified by Westlake et al. [3]; by analogy we have suggested products for Equation 7.2. Westlake et al. [3] proposed rate constants for these reactions by fitting concentrations of ions to measured values at different

altitudes in Titan's atmosphere using two different sets of conditions: (1) by fitting the $HCNH^+$ concentration for each reaction individually, and (2) by including Equations 7.1, 7.3, and 7.4 as a group and fitting the product ion concentrations (Table 7.1). Although these reactions have been previously studied both experimentally and computationally [4–19], no one has specifically searched for the products suggested in Equations 7.1–7.4 (Table 7.2). We thank Dr. Veronique Vuitton of the Laboratoire de Planétologie de Grenoble for bringing this issue to our attention and for requesting our studies to resolve this problem.

All previous experimental work has been carried out using a selected ion flow tube (SIFT) [15–17] or a flowing afterglow-selected ion flow/drift tube (FA-SIFDT) [18]. For Equation 7.1, Herbst [4] used a purely statistical approach to calculate a radiative association rate constant. On the other hand, Smith & Adams [5] included an experimentally measured, upper limit association rate constant (300 K) in a similar statistical model. These two methods give largely different values, $< 2.7 \times 10^{-13}$ cm^3 s^{-1} [4] and $\leq 1 \times 10^{-16}$ cm^3 s^{-1} [5] at 50 K, where the value reported by Smith & Adams [5] has been adjusted for the lower temperature. Although there is a large difference in these two values, this discrepancy has never been resolved. No reaction has been observed for Equation 7.2, and therefore no rate constants have been determined [10, 11].

The reaction of $HCNH^+$ with C_2H_2 has been studied both experimentally and computationally. Herbst et al. [8] compared experimental and theoretical three-body association rate constants for the production of the $C_3H_4N^+$ ion at 300 K and found a large inconsistency, 5×10^{-29} cm^6 s^{-1} and 2×10^{-25} cm^6 s^{-1}, respectively. The assumed structure of $C_3H_4N^+$ was the lowest energy isomer, protonated propenenitrile (acrylonitrile)(C_2H_3CN); however, Herbst et al. [8] noted that due to the large discrepancy, it was not likely that this isomer was being formed. A second measurement of the three-body association rate constant by Anicich et al. [11], $k = 6 \times 10^{-29}$ cm^6 s^{-1}, corroborates the experimental measurement of Herbst et al. [8]; however, no structural information was obtained. Milligan et al. [12] used experimental and computational work to determine that there are likely two isomers present

Table 7.1: Rate constants for reactions of $HCNH^+$ modeled by Westlake et al. (2012)

Neutral Reactant	Product(s)	Individual Rate Constants ($cm^3\ s^{-1}$)[a]	Group Rate Constants ($cm^3\ s^{-1}$)[b]
H_2	$CH_2NH_2{}^+$	6×10^{-11}	2×10^{-11}
CH_4	Not specified	1×10^{-11}	—
C_2H_2	$C_3HNH^+ + H_2$	2×10^{-11}	5×10^{-11}
C_2H_4	$C_3H_3NH^+ + H_2$	2×10^{-11}	6×10^{-13}

[a] Rate constants were determined by considering each reaction individually and fitting the concentration of $HCNH^+$ to measured values at different altitudes in Titan's ionosphere [3].
[b] Rate constants were determined by including the reactions of $HCNH^+$ with H_2, C_2H_2, and C_2H_4 and fitting the concentrations of the resulting products with measured values at different altitudes in Titan's ionosphere [3].

Table 7.2: Rate constants for reactions of $HCNH^+$ determined by previous workers

Neutral Reactant	Product	Rate Constant[a]	Reference
H_2	—	$< 2.1 \times 10^{-13}\ cm^3\ s^{-1}$	Herbst [4]
		$\leq 1 \times 10^{-16}\ cm^3\ s^{-1}$	Smith & Adams [5]
CH_4	—	No Reaction	Anicich et al. [10]
		No Reaction	Anicich et al. [11]
C_2H_2	$C_3H_4N^+$	$5\ (\pm 25\%) \times 10^{-29}\ cm^6\ s^{-1}$	Herbst et al. [8]
		No Reaction	Anicich et al. [10]
		$6\ (\pm 30\%) \times 10^{-29}\ cm^6\ s^{-1}$	Anicich et al. [11]
C_2H_4	$C_3H_6N^+$	$7\ (\pm 25\%) \times 10^{-27}\ cm^6\ s^{-1}$	Herbst et al. [8]
		No Reaction	Anicich et al. [10]
		$5\ (\pm 30\%) \times 10^{-27}\ cm^6\ s^{-1}$	Anicich et al. [11]

[a] Radiative rate constants have units of $cm^3\ s^{-1}$, whereas three-body rate constants have units of $cm^6\ s^{-1}$.

in the flow tube experiments, one that is electrostatically bound and one that is proposed to be a cyclic isomer. Lastly, Bera et al. [14] have calculated three barrierless association products corroborating the work of Milligan et al. [12]. The thermochemistry involved in this reaction, especially the possible formation of propenenitrile, is not only important to the chemistry of Titan, but also to industrial applications [19].

Likewise, the reaction of $HCNH^+$ and C_2H_4 has also been extensively studied [8–12]. The three-body association rate constant has been previously measured in two studies, $k = 7 \times 10^{-27}$ cm^6 s^{-1} [8] and $k = 5 \times 10^{-27}$ cm^6 s^{-1} [11]. Similar to the reaction with C_2H_2, the theoretical three-body association rate constant determined by Herbst et al. [8] is larger by several orders of magnitude, $k = 3 \times 10^{-25}$ cm^6 s^{-1}. Again, the lowest energy isomer, protonated propanenitrile, is likely not the association product [8]. The experimental work of Wilson et al. [9] suggests that the protonated isocyanoethane isomer is the product, and the extensive calculations carried out by Liu et al. [13] of the $C_3H_6N^+$ adduct ion confirms that this is the only energetically allowed product. However, the experimental work of Milligan et al. [12] discredits the protonated propanenitrile and protonated isocyanoethane ion as the isomer generated in the SIFT experiments and suggests a cyclic isomer as the product. In addition, Bera et al. [14] have found four barrierless association products, two T-shaped and two cyclic isomers. Although previous experimental and computational data exist, this discrepancy has never been resolved. The four reactions in Equations 7.1–7.4 are discussed in detail in Section 7.3 and new insight is drawn from the combination of experiment and theory. In particular we explore the products suggested by Westlake et al. [3] and characterize the structure of $C_3H_6N^+$.

7.2 Methods

Reactions of $HCNH^+$ with neutral molecules are investigated using a flowing afterglow-selected ion flow tube (FA-SIFT) instrument. The association product for the reaction of $HCNH^+$ with C_2H_4, $C_3H_6N^+$, is investigated using proton transfer reactions to determine

the structure. The experimental results are further supported by density functional theory (DFT) and ab initio calculations of chemical structures and their energies.

7.2.1 Experimental

The experiments are carried out at 298 K using an FA-SIFT instrument (Figure 7.1). Here, protonated hydrogen cyanide ($HCNH^+$, m/z 28) is generated using electron ionization (70 eV ionization energy) of dimethylamine [$(CH_3)_2NH$] in a helium buffer gas. The reactant ions are then mass-selected using a quadrupole mass filter, injected into the reaction flow tube, and collisionally cooled by a helium carrier gas (0.35–0.45 Torr) prior to addition of neutral reactants. Measured concentrations of neutral molecules are added to the reaction flow tube through a manifold of inlets. The reactant-ion signal is monitored as a function of reaction distance using a quadrupole mass filter coupled to an electron multiplier. Rate constants or upper limits in reactivity are derived using pseudo first-order kinetics [20]. We note that it was not possible to completely exclude m/z 30 in the injection process, but this ion was unreactive with all neutral reagents and does not affect the studies of $HCNH^+$.

To determine the structure of $C_3H_6N^+$, the proton affinity of the association complex was determined by probing the proton-transfer reaction with molecules whose PA is known. $C_3H_6N^+$ ions are generated by adding C_2H_4 to the reaction flow tube 24 cm downstream of the injection inlet for $HCNH^+$; subsequently, neutral reagents, listed in Table 7.3, are added 50 cm further downstream (Figure 7.1). These conditions allow complete reaction of the $HCNH^+$ ion and ensure that the $C_3H_6N^+$ product complex is collisionally stabilized.

The neutral reagents included in this study are listed along with the chemical formulas and percent purities: hydrogen (H_2; 99.999%), methane (CH_4; 99.0%), acetylene (C_2H_2; $\geq$ 99.6%), ethylene (C_2H_4; 99.5%), benzene (C_6H_6; $>$ 99%), methanol (CH_4O; $\geq$ 99.9%), phenol (C_6H_6O; $>$ 99%), formamide (CH_3NO; $\geq$ 99.5%), 2-methylfuran (C_5H_6O; 99%), N,N-dimethylformamide (C_3H_7NO; $>$ 99%), methylhydrazine (CH_6N_2; 98%), 1,1-dimethylhydrazine ($C_2H_8N_2$; 98%).

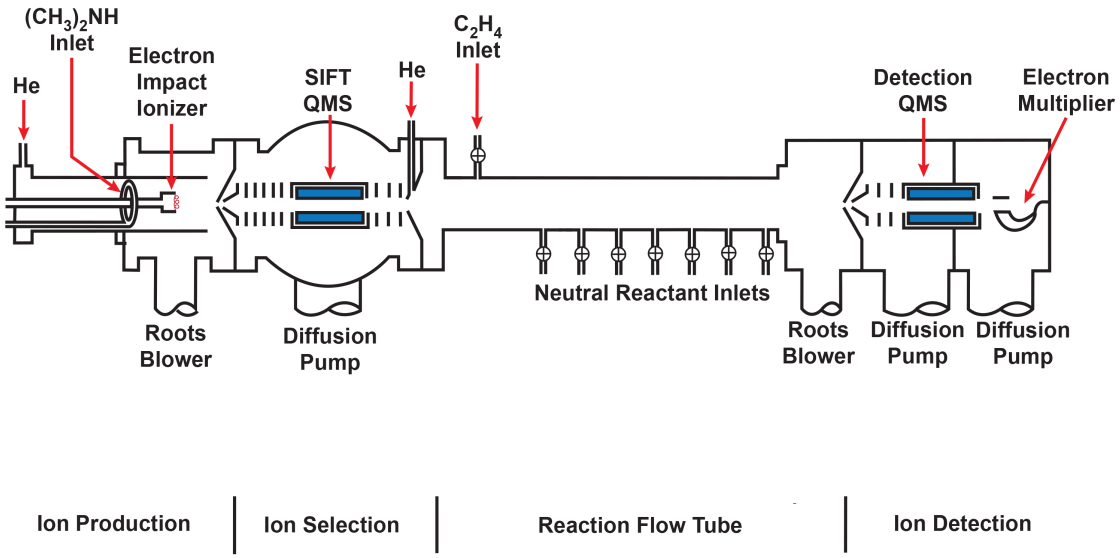

Figure 7.1: Flowing afterglow-selected ion flow tube setup for determination of the structure of $C_3H_6N^+$. The $C_3H_6N^+$ adduct ion was generated by adding C_2H_4 to the reaction flow tube 24 cm downstream of the injection inlet for $HCNH^+$; subsequently, neutral reagents are added 50 cm further downstream.

Table 7.3: Characterization of $C_3H_6N^+$ (formed from the reaction of $HCNH^+ + C_2H_4$) by proton transfer reactions

Neutral Reactant (R)	Experimental PA[a] (kcal mol^{-1})	Calculated PA[b] (kcal mol^{-1})	Proton Transfer Observed[c]
Benzene	179	180	No
Methanol	180	177	No
Propanenitrile[d]	190	188	—
Phenol	195	194	No
Formamide	197	195	No
Isocyanoethane[d]	204	200	—
2-Methylfuran	207	205	Yes
N-Methyleneethenamine[d]	—	210	—
N,N-Dimethylformamide	212	207	Yes
Methylhydrazine	215	214	Yes
(Z)-2-Propen-1-imine[d]	—	217	—
(E)-2-Propen-1-imine[d]	218	219	—
Cyclopropanimine[d]	—	220	—
1,1-Dimethylhydrazine	222	220	Yes

[a] Proton affinity (PA) values taken from Hunter & Lias [33]. There is an uncertainty of ±2 kcal mol^{-1} associated with the reported values.
[b] Energies calculated at the B3LYP/6-311++G(d, p)//B3LYP/6-31+G(d) level of theory at 298 K [29].
[c] Reaction of R with $C_3H_6N^+$.
[d] Isomers of C_3H_5N.

7.2.2 Computational

DFT and ab initio calculations were carried out to support our experimental studies. Structures and geometries for reactants, products, and intermediates involved in the reactions (Figures 7.2–7.4) were computed using *Gaussian 03* [21] at the B3LYP/aug-cc-pVTZ level of theory [22–24]. Using these geometries, single point energies were calculated at the MP2(full)/aug-cc-pVTZ level of theory [25]. This level of theory has been shown to be accurate and efficient for calculating the energies of small H, C, and N containing species [26]. Because the theoretically calculated energies are temperature dependent, we determine reaction enthalpies at 141 K, the temperature of Titan's atmosphere 1010 km from the surface [3]. However, at these low pressures (10^{-7} Torr [1, 27]) the ideal gas limit can be applied, and the enthalpies are pressure independent. The relative potential energy surfaces shown in Figures 7.3 and 7.4 are consistent with previous calculations [9, 13, 14, 18]. Proton affinities were calculated at the B3LYP/6-311++G(d, p)//B3LYP/6-31+G(d) level of theory [28].

7.3 Results and Discussion

The reactions of $HCNH^+$ with H_2, CH_4, C_2H_2, and C_2H_4 are investigated to search for the products listed in Equations 7.1–7.4. The experimental conditions were optimized, and the appropriate m/z regions of the mass spectrum were carefully monitored. None of these products were observed experimentally; however, an association product was detected for the reaction of $HCNH^+$ with C_2H_2 and C_2H_4. All reactions were explored computationally and the structure of the $HCNH^+$ + C_2H_4 adduct was characterized experimentally and computationally.

7.3.1 Confirmation of the $HCNH^+$ Structure

Three possible isomers exist for this ion, $HCNH^+$, H_2CN^+, and $CNH_2{}^+$. Based on the chemistry included in the models of Titan's ionosphere, linear $HCNH^+$ is likely the dominant

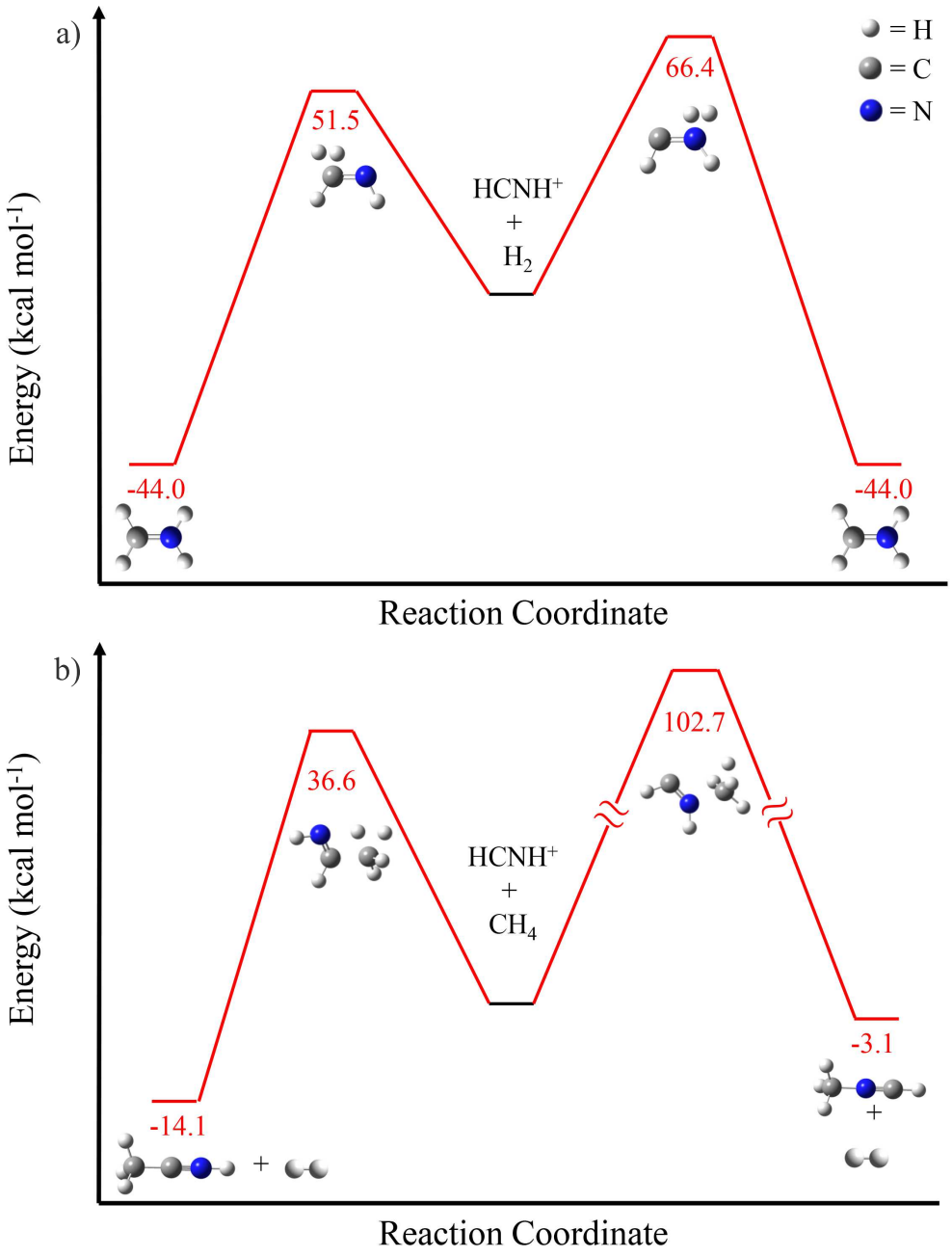

Figure 7.2: $HCNH^+ + H_2$ and $HCNH^+ + CH_4$ reaction coordinate plots. Energies and geometries are obtained from ab initio calculations performed at the MP2(full)/aug-cc-pVTZ//B3LYP/aug-cc-pVTZ level of theory (kcal mol^{-1}). All pathways are disallowed, endothermic, and traced in red lines. No ionic product is observed for these reactions.

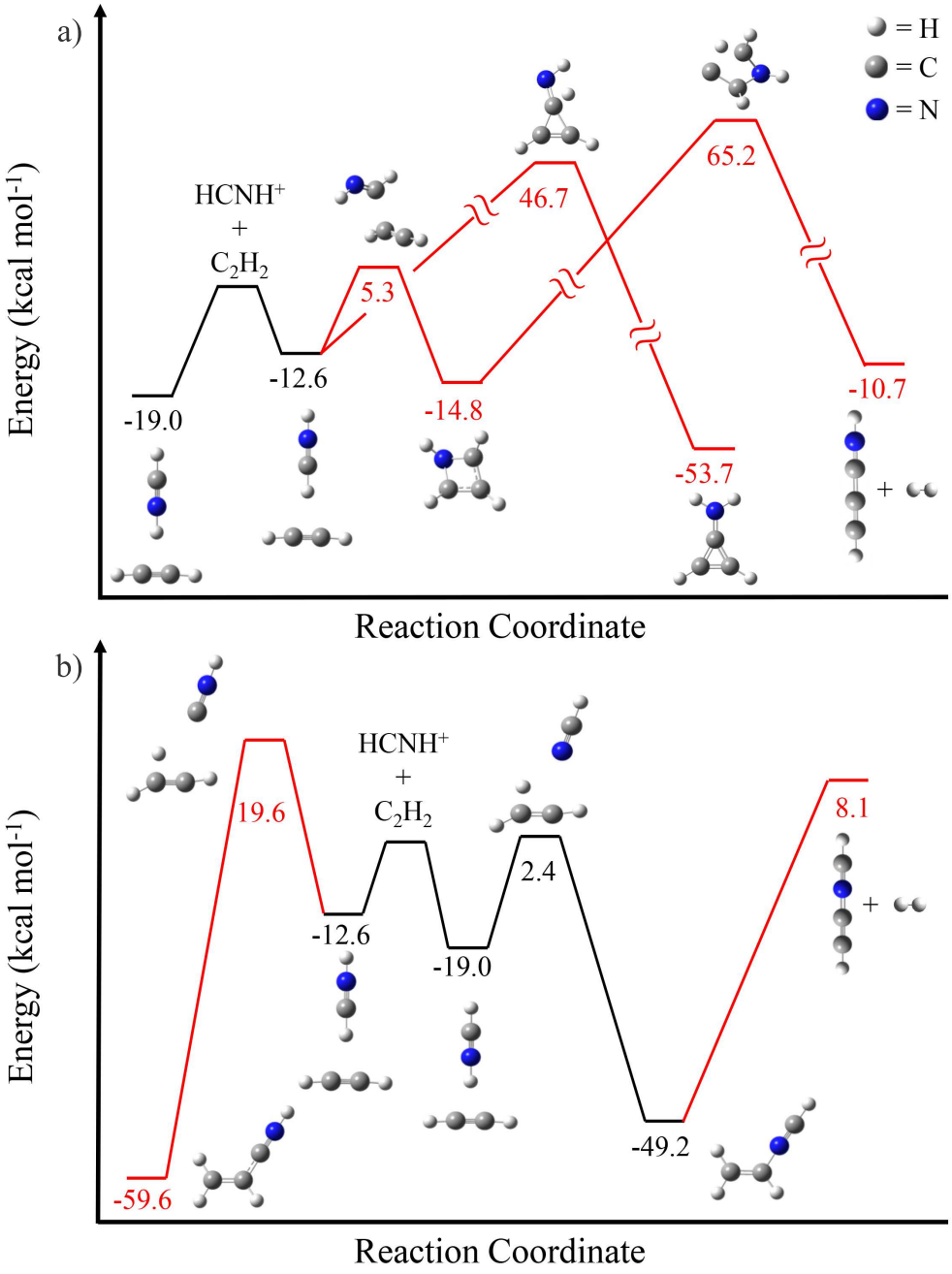

Figure 7.3: $HCNH^+ + C_2H_2$ reaction coordinate plot. Energies and geometries are obtained from ab initio calculations performed at the MP2(full)/aug-cc-pVTZ//B3LYP/aug-cc-pVTZ level of theory (kcal mol^{-1}). Allowed pathways are traced in black lines and disallowed, endothermic pathways are traced in red lines. The product of this reaction is $C_3H_4N^+$. See Section 7.3.2 for additional details.

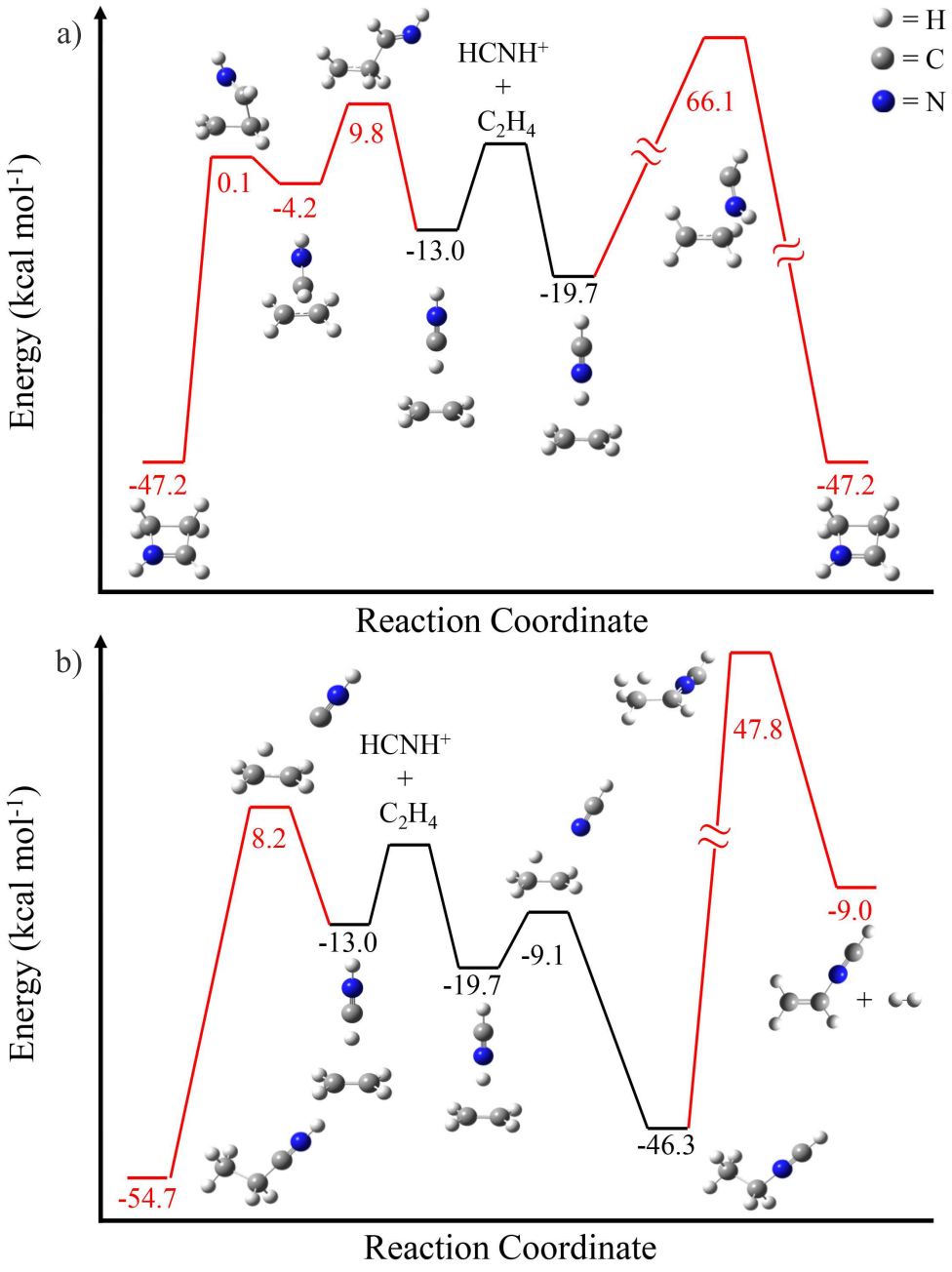

Figure 7.4: $HCNH^+ + C_2H_4$ reaction coordinate plot. Energies and geometries are obtained from ab initio calculations performed at the MP2(full)/aug-cc-pVTZ//B3LYP/aug-cc-pVTZ level of theory (kcal mol^{-1}). Allowed pathways are traced in black lines and disallowed, endothermic pathways are traced in red lines. The product of this reaction is $CH_3CH_2NCH^+$.

isomeric form [1, 3, 29, 30]. We are able to confirm that the ion at m/z 28 in our experiments is the linear $HCNH^+$ ion rather than the H_2CN^+ or $CNH_2{}^+$ isomer. First, the H_2CN^+ cation is highly unstable and is likely not formed by this method of generation of $HCNH^+$ [31]. Second, we have calculated the proton affinity (PA) of

$$CNH + H^+ \longrightarrow CNH_2{}^+ \tag{7.5}$$

to be 131 kcal mol^{-1}, which is lower than the PA of C_2H_2 (153 kcal mol^{-1}) and C_2H_4 (162 kcal mol^{-1}) [32]. Thus, if a significant amount of $CNH_2{}^+$ were present, rapid proton transfer reactions would be expected with C_2H_2 and C_2H_4; however, these reactions were not observed. In addition, we were able to confirm that no significant amount of $N_2{}^+$ (m/z 28) was present by probing for the reaction of $N_2{}^+ + HCOOH \longrightarrow CHO^+ +$ Neutral Products ($k = 4.6 \times 10^{-9}$ cm^3 s^{-1} [33]). The only ionic product observed for the reaction of m/z 28 with HCOOH was m/z 47, indicating the proton transfer reaction of

$$HCNH^+ + HCOOH \longrightarrow HC(OH)_2{}^+ + HCN, \tag{7.6}$$

with a rate constant of $k = 1.4 \times 10^{-9}$ cm^3 s^{-1} [34].

7.3.2 $HCNH^+ + H_2$, CH_4, and C_2H_2

No ionic products were observed for the reactions of $HCNH^+$ with H_2 and CH_4, and only small amounts of adduct were detected for the reactions with C_2H_2. These results are in agreement with previous studies and our measured upper limit rate constants do not improve upon published values. In addition to the experimental search for ionic products, in particular the products suggested by Westlake et al. [3], we have also computationally probed the reaction coordinate for Equations 7.1–7.3. For the reaction of $HCNH^+$ with H_2 there are large energy barriers of 51.5 and 66.4 kcal mol^{-1}, depending on the orientation of the neutral molecule relative to the ion (Figure 7.2a). These barriers will inhibit formation of the suggested products since the reactants have only a thermal distribution of internal and

kinetic energies. Likewise, reaction with CH_4 shows barriers along the reaction coordinate of 36.6 and 102.7 kcal mol^{-1} (Figure 7.2b).

The reaction coordinate for $HCNH^+$ with C_2H_2 (Figure 7.3) contains multiple pathways, and four probable low-energy complexes are considered: protonated propenenitrile (CH_2CHCNH^+), protonated isocyanoethene (CH_2CHNCH^+), protonated azete (c-$C_3H_4N^+$), and protonated cyclopropeneimine [(c-C_3H_2)NH_2^+]. Here, we have computed that there are reaction barriers along the potential energy surface that inhibit the production of protonated propenenitrile, protonated azete, and protonated cyclopropeneimine. The most probable isomer, protonated isocyanoethene, also contains a small barrier (2.4 kcal mol^{-1} at 141 K) along the reaction pathway. The low barrier in combination with the thermal distribution of energy associated with the reactants could explain the low rate constant measured by previous researchers. Although we were unable to determine a barrierless formation pathway for the cyclic product, we have investigated this structure based on the computational work of Bera et al. [14]; however, there exists a barrier above the energy of the reactants for the loss of H_2 from the cyclic structure (Figure 7.3a). In addition, loss of H_2 from protonated isocyanoethene is highly endothermic and rearrangement to give the protonated propenenitrile adduct is endothermic as well, thus inhibiting the reaction from forming the products in Equation 7.3 (Figure 7.3). The two separate structures of $C_3H_4N^+$ observed experimentally by Milligan et al. [12] can also be explained by examining the potential energy surface. The electrostatically bound structure is likely one or both of the T-shaped complexes shown in Figure 7.3, while the covalently bound species likely corresponds to the CH_2CHNCH^+ or the c-$C_3H_4N^+$ adduct.

7.3.3 $HCNH^+ + C_2H_4$

A similar analysis has been carried out for the reaction of $HCNH^+$ with C_2H_4, where only the association product $C_3H_6N^+$ was observed. This reaction has also been probed by other groups [8, 9, 12, 14], where linear and cyclic adduct isomers have been suggested as

possible products. Although an extensive search did not reveal the products suggested in Equation 7.4, we did observe an association reaction. This association molecule has numerous isomers; however, there is only one product that is energetically feasible under our experimental conditions and those of Titan's ionosphere, protonated isocyanoethane ($CH_3CH_2NCH^+$). We have confirmed the identity of the association product experimentally by probing the proton transfer reaction (Equation 7.7) of $C_3H_6N^+$ with other organic molecules (R) with similar PAs, see Table 7.3.

$$C_3H_6N^+ + R \longrightarrow C_3H_5N + RH^+. \tag{7.7}$$

The PAs of five C_3H_5N isomers were calculated for comparison with experimental data. The experimental PA of CH_3CH_2NC is 204 ± 2 kcal mol^{-1} [32]. The $C_3H_6N^+$ ion (formed by the reaction of $HCNH^+ + C_2H_4$) does proton transfer with molecules of higher PA, but does not proton transfer with molecules of lower PA. These results confirm the identification of $C_3H_6N^+$ as protonated ethyl isocyanide (Table 7.3). We report a three-body rate constant of $k \geq 8.7$ (±20%) × 10^{-27} cm^6 s^{-1} for the reaction of

$$HCNH^+ + C_2H_4 \longrightarrow C_3H_6N^+, \tag{7.8}$$

which is in agreement with previously measured values within the combined error bars [8, 12] (Table 7.2).

The complete reaction coordinate has been mapped previously by Liu et al. [13] and our computational work corroborates their results (Figure 7.4). The only energetically allowed pathway produces the protonated isocyanoethane isomer ($CH_3CH_2NCH^+$). Liu et al. [13] have calculated 42 isomers of $C_3H_6N^+$; however, their results also confirm that formation of the protonated isocyanoethane isomer is the only pathway that does not contain a barrier above the reactant energy. In addition, there is a 51.3 kcal mol^{-1} barrier along the reaction path from protonated propanenitrile to form the products in Equation 7.4 ($C_3H_3NH^+ + H_2$) inhibiting this product from forming under our experimental conditions and those of Titan's ionosphere (Figure 7.4b).

7.4 Conclusion

We have investigated the chemistry of $HCNH^+$ with H_2, CH_4, C_2H_2, and C_2H_4 to probe for the products suggested by Westlake et al. [3]. The combination of experimental and computational results has given insight into these four reactions related to Titan's ionosphere. In all cases, the products listed in Equations 7.1–7.4 were not observed experimentally. The large energy barriers determined computationally will inhibit these reaction pathways and they will not contribute significantly to the depletion of $HCNH^+$. In addition, the proposed ionic products $CH_2NH_2^+$, C_3HNH^+, and $C_3H_3NH^+$ will not be formed from these reactions unless significant energy barriers are overcome. The structures of the association products for the reactions of $HCNH^+$ with C_2H_2 and C_2H_4 have been revealed by experiment and by DFT and ab initio calculations. These structures and calculated radiative association rate constants should be included in models of Titan's ionosphere and other interstellar environments.

Upon further review of the models used by Vuitton et al. [1] and Westlake et al. [3], we suggest the inclusion of the proton transfer reactions of $HCNH^+$ with propyne (C_3H_4), propene (C_3H_6), and 1,3,5-heptatriyne (CH_3C_6H [1]) because their PAs are greater than that of $HCNH^+$ [34]. The rate constants for these reactions have not been measured experimentally, but their exothermicities are similar to other proton transfer reactions included in the models of Vuitton et al. [1] and Westlake et al. [3] (i.e., C_4H_2, HC_3N, H_2O, CH_3OH). Thus, the rate constant of $k = 3 \times 10^{-9}$ cm^3 s^{-1} should be adopted for these reactions to be consistent with unmeasured proton transfer reactions included in the model of Vuitton et al. [1]. Although these rate constants are large, the inclusion of these reactions will not be sufficient to account for the overabundance of $HCNH^+$ due to the low concentration of these neutral species. In addition, the inclusion of C_3H_4 and C_3H_6 will exacerbate the overproduction of $C_3H_5^+$ and $C_3H_7^+$, highlighting the fact that the chemistry of Titan's ionosphere is not completely understood.

7.5 References

1. Vuitton, V.; Yelle, R. V.; McEwan, M. J., Ion Chemistry and N-Containing Molecules in Titan's Upper Atmosphere. *Icarus* **2007**, *191*, 7222.

2. Robertson, I. P.; Cravens, T. E.; Waite , J. H., Jr.; Yelle, R. V.; Vuitton, V.; Coates, A. J.; Wahlund, J. E.; Ågren, K.; Mandt, K.; Magee, B.; Richard, M. S.; Fattig, E., Structure of Titan's Ionosphere: Model Comparisons with Cassini Data. *Planet. Space Sci.* **2009**, *57*, 1834.

3. Westlake, J. H.; Waite, J. H., Jr.; Mandt, K. E.; Carrasco, N.; Bell, J. M.; Magee, B. A.; Wahlund, J. E., Titan's Ionospheric Composition and Structure: Photochemical Modeling of Cassini INMS Data. *J. Geophys. Res.* **2012**, *117*, E01003.

4. Herbst, E., Radiative Association in Dense, H_2-Containing Interstellar Clouds. *Astrophys. J.* **1976**, *205*, 94.

5. Smith, D.; Adams, N. G., Molecular Synthesis in Interstellar Clouds: Some Relevant Laboratory Measurements. *Astrophys. J.* **1977**, *217*, 741.

6. Herbst, E., A New Look at Radiative Association in Dense Interstellar Clouds. *Astrophys. J.* **1980**, *237*, 462.

7. Herbst, E., An Additional Uncertainty in Calculated Radiative Association Rates of Molecular Formation at Low Temperatures. *Astrophys. J.* **1980**, *241*, 197.

8. Herbst, E.; Smith, D.; Adams, N. G.; McIntosh, B. J., Association Reactions. Theoretical Shortcomings. *J. Chem. Soc. Faraday Trans. 2* **1989**, *85*, 1655.

9. Wilson, P. F.; Freeman, C. G.; McEwan, M. J., Isomers of $C_3H_6N^+$ and the Interstellar Synthesis of C_2H_5CN. *Int. J. Mass Spectrom. Ion Process.* **1993**, *128*, 83.

10. Anicich, V. G.; McEwan, M. J., Ion-Molecule Chemistry in Titan's Ionosphere. *Planet. Space Sci.* **1997**, *45*, 897.

11. Anicich, V. G.; Milligan, D. B.; Fairley, D. A.; McEwan, M. J., Termolecular Ion-Molecule Reactions in Titan's Atmosphere, I: Principal Ions with Principal Neutrals. *Icarus* **2000**, 146, 118.

12. Milligan, D. B.; Freeman, C. G.; Maclagan, R. G. A. R.; McEwan, M. J.; Wilson, P. F.; Anicich, V. G., Termolecular Ion-Molecule Reactions in Titan's Atmosphere. II: The Structure of the Association Adducts of $HCNH^+$ with C_2H_2 and C_2H_4. *J. Am. Soc. Mass Spectrom.* **2001**, *12*, 557.

13. Liu, G.-x.; Ding, Y.-h.; Li, Z.-s.; Huang, X.-r.; Sun, C.-C., Theoretical Revisit on Potential Energy Surface of $[C_3H_6N]^+$. *J. Mol. Struct.: THEOCHEM* **2001**, *548*, 191.

14. Bera, P. P.; Head-Gordon, M.; Lee, T. J., Initiating Molecular Growth in the Interstellar Medium via Dimeric Complexes of Observed Ions and Molecules. *Astron. Astrophys.* **2011**, *535*, A74.

15. Adams, N. G.; Smith, D., The Selected Ion Flow Tube (SIFT); A Technique for Studying Ion-Neutral Reactions. *Int. J. Mass Spectrom. Ion Process.* **1976**, *21*, 349.

16. Adams, N. G.; Smith, D., Product-Ion Distributions for Some Ion-Molecule Reactions. *J. Phys. B* **1976**, 9, 1439.

17. Knight, J. S.; Freeman, C. G.; McEwan, M. J.; Adams, N. G.; Smith, D., Selected-Ion Flow Tube Studies of HC_3N. *Int. J. Mass Spectrom. Ion Process.* **1985**, *67*, 317.

18. Milligan, D. B.; Fairley, D. A.; Freeman, C. G.; McEwan, M. J., A Flowing Afterglow Selected Ion Flow Tube (FA/SIFT) Comparison of SIFT Injector Flanges and $H_3^+ + N$ Revisited. *Int. J. Mass Spectrom.* **2000**, *202*, 351.

19. Notario, R.; Roux, M.; Liebman, J., What is the Enthalpy of Formation of Acrylonitrile? *Struct. Chem.* **2010**, *21*, 481.

20. Bierbaum, V. M., Flow Tubes. In *Encyclopedia of Mass Spectrometry*, Armentrout, P. B., Ed.; Elsevier: Amsterdam, 2003; p 940.

21. Frisch, M. J.; Trucks, G. W.; Schlegel, H. B.; Scuseria, G. E.; Robb, M. A.; Cheeseman, J. R.; Montgomery, J. A., Jr.,; Vreven, T.; Kudin, K. N.; Burant, J. C. et al. *Gaussian 03*, Revision E.01; Gaussian Inc.: Wallingford, CT, 2003.

22. Becke, A. D., Density-Functional Thermochemistry. III. The Role of Exact Exchange. *J. Chem. Phys.* **1993**, *98*, 5648.

23. Lee, C.; Yang, W.; Parr, R. G., Development of the Colle-Salvetti Correlation-Energy Formula into a Functional of the Electron Density. *Phys. Rev. B* **1988**, *37*, 785.

24. Dunning, T. H., Jr., Gaussian Basis Sets for Use in Correlated Molecular Calculations. I. The Atoms Boron Through Neon and Hydrogen. *J. Chem. Phys.* **1989**, *90*, 1007.

25. Møller, C.; Plesset, M. S., Note on an Approximation Treatment for Many-Electron Systems. *Phys. Rev.* **1934**, *46*, 618.

26. Yang, Z.; Snow, T. P.; Bierbaum, V. M., Computational Studies of Gas Phase Reactions of Carbon Chain Anions with N and O Atoms. *Phys. Chem. Chem. Phys.* **2010**, *12*, 13091.

27. Thissen, R.; Vuitton, V.; Lavvas, P.; Lemaire, J.; Dehon, C.; Dutuit, O.; Smith, M. A.; Turchini, S.; Catone, D.; Yelle, R. V.; Pernot, P.; Somogyi, A.; Coreno, M., Laboratory Studies of Molecular Growth in the Titan Ionosphere. *J. Phys. Chem. A* **2009**, *113*, 11211.

28. Kaur, D.; Khanna, S.; Kaur, R. P., The Role of Conjugative Interactions in Acidic and Basic Character of Five Membered Aromatic Heterocyclics. *J. Mol. Struct.: THEOCHEM* **2010**, *949*, 14.

29. Talbi, D.; Herbst, E., An Extensive Ab Initio Study of the $C^+ + NH_3$ Reaction and its Relation to the HNC/HCN Abundance Ratio in Interstellar Clouds. *Astron. Astrophys.* **1998**, *333*, 1007.

30. Talbi, D., An Extensive Ab Initio Study of a Process of Astrophysical Interest: the $N^+(N) + CH_3(CH_3^+)$ Reaction. *Chem. Phys. Lett.* **1999**, *312*, 291.

31. Burgers, P. C.; Holmes, J. L.; Terlouw, J. K., Gaseous $[H_2, C, N]^+$ and $[H_3, C, N]^{+\cdot}$ Ions. Generation, Heat of Formation, and Dissociation Characteristics of $[H_2CN]^+$, $[HCNH]^+$, $[CNH_2]^+$, $[H_2CNH]^{+\cdot}$, and $[HCNH_2]^{+\cdot}$. *J. Am. Chem. Soc.* **1984**, *106*, 2762.

32. Linstrom, P. J.; Mallard, W. G., Eds., In *NIST Chemistry WebBook, NIST Standard Reference Database Number 69*; NIST: Gaithersburg, MD, 2014.

33. Freeman, C. G.; Harland, P. W.; McEwan, M. J., Ion-Molecule Reactions of Formic Acid. I. Proton-Transfer Reactions. *Aust. J. Chem.* **1978**, *31*, 2157.

34. Lide, D. R., Ed., *CRC Handbook of Chemistry and Physics*, 89th ed.; CRC Press: Boca Raton, FL, 2008.

Chapter 8

Conclusion

The field of astrochemistry has gained increasing attention in the last decade. Several universities now offer degrees in astrochemistry and the American Chemical Society has added astrochemistry as an official subgroup of the Physical Chemistry Division. It is clear from the progression of this interdisciplinary field that a single area of study can not solve all of the mysteries of space. The combination of observations, models, and laboratory chemistry has lead to the identification of some unique molecules, including anions. The Atacama Large Millimeter/submillimeter Array (ALMA) recently commenced scientific observations and will be instrumental in mapping our chemical universe. The ALMA telescope will be able to detect species in low concentrations that were not previously observable. In addition, this highly sensitive telescope is capable of collecting detailed information about interstellar environments and it will take the collaboration of astronomers, modelers, and chemists to interpret the data and direct future studies. The research presented in this thesis has focused on gas-phase ion-molecule chemistry in interstellar, circumstellar, and planetary environments to better understand their chemical makeup and give insight into chemical networks and reaction dynamics.

Polycyclic aromatic hydrocarbons are ubiquitous throughout the interstellar medium and their chemical makeup varies greatly depending on local conditions. In diffuse regions where the flux of interstellar radiation is high, large (> 30 carbon atoms) neutral and cationic PA(N)Hs are likely present. In areas of moderate density, such as translucent clouds, neutral

PA(N)Hs are the dominant charge state. The size distribution in this region could vary from small to large PA(N)Hs since the interstellar UV radiation is low and these molecules are relatively unreactive. In the most dense regions, anionic PA(N)Hs may compete in abundance with neutral species. The phenoxide anion is one possible oxygen-containing PAH to search for in dense regions since it has a similar basicity to CN^-, which has been detected, and the parent radical has a large electron affinity (2.25 eV). In addition, ionic PA(N)Hs are advantageous for identification using their rotational spectra because they possess a permanent dipole moment.

The reaction of H^- with H is efficient, while reaction with H_2 is not observed. The hydride ion also reacts efficiently with many classes of organic molecules identified in the ISM. Thus, H^- will likely survive in greatest concentration in regions such as translucent clouds, where the flux of interstellar radiation is low, H_2 is the dominant form of hydrogen, and large organic molecules are not in high abundance.

From a chemical standpoint, CF^+ is a good molecular tracer for C^+. Although this ion is highly reactive with many organic compounds, it is unreactive with the small molecules that will be present in areas where C^+ is in high density. In photodissociation regions where CF^+ and oxygen-containing organics are present, it may be advantageous to search for the spectral signatures of fluorinated formaldehyde. The presence of secondary ion-molecule reactions in the flow tube indicates that the ionic products formed by the reactions of CF^+ are also highly reactive. A chemical network including these reactions should be established to determine the end state of these cations.

The Cassini-Huygens probe offers astrochemists another analysis tool, not available for analyzing interstellar clouds. However, even with this added advantage, knowledge of Titan's atmospheric chemistry remains incomplete. The reactions of $HCNH^+$ with H_2, CH_4, C_2H_2, and C_2H_4 are not major destruction pathways for $HCNH^+$ and need not be included in models of Titan's ionosphere. A more detailed look at current models has revealed the omission of three proton-transfer reactions; however, these additional reactions only exacerbate the

overprediction of other species. It is clear from this study that the atmosphere of Titan is not completely understood and personal communications with fellow scientists indicate that models such as these are under continual revision.

The chemistry investigated in this study has provided insight into the reactivity of $PA(N)H^+$, $[PAH–H]^-$, H^-, CF^+, $HCNH^+$. The results aid in the chemical description of interstellar, circumstellar, and planetary environments and guide future astronomical observations. In addition, this work should be continued to include new classes of compounds and analysis techniques. First, further studies should be carried out to characterize the reactivity of nitrogen-containing PAHs, with one or more nitrogen atoms. These species are likely present and have astrobiological implications. Second, the recent detection of PAH signatures in oxygen-rich environments suggests that the chemistry of oxygen-containing PAHs should be investigated. Lastly, the electronic spectra of CF^+ should be measured experimentally. This simple molecule may lead to the first definitive assignment of a DIB. Nonetheless, it is clear that we must "think outside the box" to solve this spectroscopic mystery.

Appendix A

Comparison of Reaction Exothermicities for H atom with PA(N)H Cations

A.1 Introduction

The reaction thermodynamics for H atom association with PA(N)H cations was investigated at each available position of the cation. Listed in Table A.1 are the PA(N)H cations, association products, experimentally determined energies where available, and theoretically calculated energies at 0 K and 298 K. PAH molecules are numbered according to IUPAC rules so that the maximum number of rings lie in a horizontal row and as many rings as possible are above and to the right of the horizontal row [1]. Numbering starts with the most counter-clockwise carbon and commences in a clockwise manner counting only the exterior carbons. PANH molecules are oriented such that the nitrogen is placed in the lowest numbered position according to the rules above. Numbering starts at the nitrogen and proceeds clockwise. Figure 3.1 shows the PA(N)H cations investigated in this study and the distinct positions for association are numbered.

Table A.1: Comparison of Reaction Exothermicities: PA(N)H Cations + H atom

M^+	Product	$-\Delta H_{exp}$[a] (kcal mol^{-1})	$-\Delta H_{theor(0\ K)}$[b] (kcal mol^{-1})	$-\Delta H_{theor(298\ K)}$[b,c] (kcal mol^{-1})
Naphthalene$^+$	1-hydronaphthalene$^+$	66.1	63.2	64.5
	2-hydronaphthalene$^+$		60.3	61.6
Quinoline$^+$	1-hydroquinoline$^+$	113.2	108.0	109.7
	2-hydroquinoline$^+$		56.8	58.2
	3-hydroquinoline$^+$		65.5	66.9
	4-hydroquinoline$^+$		56.5	57.8
	5-hydroquinoline$^+$		68.3	69.7
	6-hydroquinoline$^+$		65.9	67.3
	7-hydroquinoline$^+$		64.5	65.9
	8-hydroquinoline$^+$		70.6	72.0
Isoquinoline$^+$	1-hydroisoquinoline$^+$	110.6	106.7	108.4
	2-hydroisoquinoline$^+$		60.9	62.3
	3-hydroisoquinoline$^+$		65.7	67.0
	4-hydroisoquinoline$^+$		65.6	67.0
	5-hydroisoquinoline$^+$		56.4	57.8
	6-hydroisoquinoline$^+$		62.3	63.7
	7-hydroisoquinoline$^+$		61.1	62.5
	8-hydroisoquinoline$^+$		58.2	59.6
Anthracene$^+$	1-hydroanthracene$^+$	67.7	53.2	54.4
	2-hydroanthracene $^+$		50.0	51.2
	5-hydroanthracene $^+$		62.0	63.2
Acridine$^+$	1-hydroacridine$^+$	98.8	96.0	97.5
	2-hydroacridine$^+$		60.7	61.9
	3-hydroacridine$^+$		52.4	53.6
	4-hydroacridine$^+$		56.0	57.2
	5-hydroacridine$^+$		56.7	58.0
	6-hydroacridine$^+$		56.5	57.7
Phenanthrene$^+$	1-hydrophenanthrene$^+$	65.7	59.2	60.5
	2-hydrophenanthrene$^+$		59.8	61.0
	3-hydrophenanthrene$^+$		58.2	59.4
	4-hydrophenanthrene$^+$		60.3	61.6
	5-hydrophenanthrene$^+$		60.2	61.5
Benzo[h]quinoline$^+$	1-hydrobenzo[h]quinoline$^+$		95.1	96.7
	2-hydrobenzo[h]quinoline$^+$		53.1	54.4
	3-hydrobenzo[h]quinoline$^+$		58.0	59.2
	4-hydrobenzo[h]quinoline$^+$		50.2	51.4
	5-hydrobenzo[h]quinoline$^+$		62.0	63.3
	6-hydrobenzo[h]quinoline$^+$		60.0	61.3
	7-hydrobenzo[h]quinoline$^+$		63.8	65.1
	8-hydrobenzo[h]quinoline$^+$		59.5	60.8
	9-hydrobenzo[h]quinoline$^+$		62.8	64.1
	10-hydrobenzo[h]quinoline$^+$		61.9	63.2

M^+	Product	$-\Delta H_{exp}$[a] (kcal mol^{-1})	$-\Delta H_{theor(0\ K)}$[b] (kcal mol^{-1})	$-\Delta H_{theor(298\ K)}$[b,c] (kcal mol^{-1})
Phenanthridine$^+$	1-hydrophenanthridine$^+$		102.9	104.6
	2-hydrophenanthridine$^+$		55.4	56.8
	3-hydrophenanthridine$^+$		59.0	60.4
	4-hydrophenanthridine$^+$		62.2	63.6
	5-hydrophenanthridine$^+$		57.1	58.5
	6-hydrophenanthridine$^+$		63.1	64.5
	7-hydrophenanthridine$^+$		65.4	66.8
	8-hydrophenanthridine$^+$		65.0	66.4
	9-hydrophenanthridine$^+$		64.1	65.6
	10-hydrophenanthridine$^+$		67.2	68.6
Pyrene$^+$	1-hydropyrene$^+$	65.4	61.6	62.8
	2-hydropyrene$^+$		47.1	48.3
	4-hydropyrene$^+$		51.0	52.2
Tetracene$^+$	1-hydrotetracene$^+$	63.6	46.6	47.8
	2-hydrotetracene$^+$		43.7	44.9
	5-hydrotetracene$^+$		58.7	59.9
Coronene$^+$	1-hydrocoronene$^+$	60.4	56.3	57.8

[a] Values determined using Hess's law with experimental values for ionization energies, bond energies, proton affinities, and heats of formation [2].
[b] B3LYP/6-311G(*d*,*p*) theory level including zero-point energy correction.
[c] Including thermal energy correction at 298 K.

A.2 References

1. Harvey, R. G., *Polycyclic Aromatic Hydrocarbons*. Cambridge Univ. Press: New York, NY, 1991.

2. Linstrom, P. J.; Mallard, W. G., Eds., In *NIST Chemistry WebBook, NIST Standard Reference Database Number 69*; NIST: Gaithersburg, MD, 2014.